Metal nanoparticle-decorated carbon nanocups for drug delivery

by

Seth Cameron Burkert

B. S., Saint Francis University, 2012

Submitted to the Graduate Faculty of

The Dietrich School of Arts and Sciences in partial fulfillment

of the requirements for the degree of

Doctor of Philosophy

University of Pittsburgh

2019

UNIVERSITY OF PITTSBURGH

DIETRICH SCHOOL OF ARTS AND SCIENCES

This dissertation was presented

by

Seth Cameron Burkert

It was defended on

April 9, 2019

and approved by

Dr. Jill Millstone, Associate Professor, Department of Chemistry

Dr. Steve Weber, Professor, Department of Chemistry

Dr. Michael Shurin, MD, Professor, Department of Pathology

Dissertation Director: Dr. Alexander Star, Professor, Department of Chemistry

Metal nanoparticle-decorated carbon nanocups for drug delivery

Seth Cameron Burkert, PhD

University of Pittsburgh, 2019

Carbon nanotubes are viewed as an ideal vehicle for drug delivery due to their ease of chemical functionalization, proven ability to penetrate cell membranes, and tunable length scales which can affect bio-distribution. However, concerns as to the potential harmful side effects of carbon nanomaterials have been reported, halting their implementation for biological applications. The incorporation of nitrogen dopants into the graphitic lattice of carbon nanotubes results in sputtered growth yielding a bamboo or stacked cup nanotube structures. The cup structures are held together through weak van der Waals forces and as such can be separated into individual cups for potential drug delivery applications. Due to their unique electrical and structural properties, nanocups represent an exciting material for a wide range of applications. We first investigated the electrochemical response of synthesized nanocups towards the oxygen reduction reaction which has important implications in fuel cell technology. Stacked nanocups were then separated into individual and short stacked segments and effectively sealed through conjugation with gold nanoparticles resulting in a unique drug delivery vehicle. The method of separation was investigated to maximize the propensity for individual nanocups to be corked with gold nanoparticles. Furthermore, the metal decoration of nanocups was explored in response to changes in the local environment illustrating a robust synthetic procedure. The developed gold nanoparticle corked nanocups showed the ability to be loaded with target molecules and effectively degraded through biologically relevant enzymes releasing the loaded cargo. These enzymes are overexpressed in important target cells in the tumor microenvironment creating a built-in targeted

delivery system for cancer therapies. The culmination of this report illustrates nanocups loaded with paclitaxel, a common chemotherapeutic agent, and systemically delivered to tumor-bearing mice resulting in tumor growth inhibition with 25–30% of mice being tumor free after 2–3 weeks. The results of this report demonstrate effective drug delivery design and a novel immunotherapy strategy dependent upon systemic cell delivery to affect change in the tumor microenvironment.

Table of contents

List of tables

List of figures

List of equations

Preface

I would like to extend my sincerest gratitude to my research advisor, Professor Alexander Star. His mentoring and scientific insight have been invaluable towards my intellectual growth over the past seven years. His experience and enthusiasm for scientific discovery have helped me develop my interest in nanoscience into focused research projects with practical applications. I appreciate the freedom he has given me in order to pursue teaching opportunities for personal development towards my future career in academia. It has been an honor to work under his guidance.

I would like to thank my committee members Professor Jill Millstone, Professor Steve Weber, and Professor Michael Shurin for their patience and valuable insight towards the improvement of my research projects. Their expertise in their respective fields has been vital for the successful implementation of my research interests.

I would like to thank my colleagues in the Star lab for their challenging discussions and thoughtful encouragement. Special thanks to Dr. Yifan Tang and Dr. Yong Zhao for their technical training and assistance in the early phases of my graduate career. To Greg Morgan, Phil Fournier, Dave White, and Sean Hwang, your friendship and support has helped me to survive the difficulties of graduate school and enjoy the achievements and successes. To other group members past and present, Dr. Mengning Ding, Dr. Yanan Chen, Dr. Wanji Seo, Dr. Gordon Chiu, Dr. Gregg Kotchey, Dr. Nadine Kraut, Dr. James Ellis, Dr. Haifeng Dong, Dr. Uri Green, Dr. Guiming Peng, Hao Bai, Ian Feigel, James Gaugler, Zachary Michael, Michael Chido, Alexandra Münzer, Wenting Shao, Guilherme de Oliveira Silva, Long Bian, Xiaoyun He, Zidao Zeng, Christian

Gamboa, and Zhengru Liu it has been my sincerest pleasure working with all of you and I wish you the best of luck in the future.

I would like to extend my gratitude to the faculty, staff, and students of the Department of Chemistry for their assistance throughout my time as a member of the University of Pittsburgh. I would like to thank Christie Hay, Mary Beth Conroy, LaShawn Youngblood and all of the other second floor staff members for their assistance throughout the years. To Tom Gasmire and the members of the machine shop, thank you for your help towards successful apparatus design to achieve my research goals. To Lori Neu for all my glass needs and her warm conversation. To Tom Harper for his help with all of my TEM questions and ideas. To Dr. Joel Gillespie for his training and valuable understanding of the many analytical techniques used within the department. To the members of the Nanoscale Fabrication and Characterization Facility for their technical assistance on the synthesis and characterization of my materials.

Without the love and support of my family and friends I would not have survived the difficulties of my PhD studies. Your constant encouragement served as the motivation to keep me going through the most challenging experience of my life. To my Mom and Dad, I cannot thank you enough for your constant understanding and unyielding support as I pursued my dreams. To my Pittsburgh family, our experiences together are some of my most cherished memories from my time in Pittsburgh and I will carry them with me forever.

Finally, I would like to thank the University of Pittsburgh and National Science Foundation for financial support and the opportunity to pursue my PhD.

1.0 Introduction

World history has been punctuated by several technological revolutions, where new technologies are developed and rapidly implemented resulting in wide spread changes to society. Technologies such as the steam engine and printing press resulted in drastic improvement over societal quality of living around the world. The isolation of nanomaterials from bulk materials and their subsequent investigation have resulted in the discovery of many unique properties exceeding current technology standards. In addition to superior properties over current technology, nanomaterials have shown unique phenomenon not previously observed resulting in previously unimagined opportunities. The rise in popularity of nanomaterial investigation and implementation indicates the dawn of a new technological revolution which can shape the state of the world for decades to come.

Nanomaterials can be defined by their length dimensions where at least one length scale exists between 1 nanometer (1×10^{-9} meters) and 100 nm.[1] These nanomaterials exhibit unique properties not observed in smaller molecular compounds or larger bulk materials. The unique properties are tied closely to particle size, interparticle distance, nature of the particle surface functionalization, and the overall shape of the nanomaterial.[2] Nanomaterial properties originate from the quantum size effect when the de Broglie wavelength of valence electrons are on the same order as the size of the particle itself.[3] At these length scales the nanomaterials are able to behave electronically as zero-dimensional quantum dots and are governed by quantum mechanical rules as opposed to classical physics. Differences in chemical reactivity, electrical properties, and structural integrity have all been observed with nanoscale materials.[4]

The implementation of nanotechnology can already be seen in today's culture with the rapid miniaturization of electronic devices, smart surfaces with coatings for protection from electromagnetic radiation or physical deformations, and the use of nanomaterials for drug delivery and biomedical applications. Nanomaterials have physical dimensions smaller than bacteria and plant and animal cells making them a prime candidate for interaction with biological systems. By observing changes in nanomaterial properties in response to interaction with biological systems, it is possible to understand complex cellular mechanisms not previously understood. Likewise, by modifying the composition of nanomaterials, chemical changes to their local environment can be performed resulting in altered biological functions. Lastly, the interaction of nanomaterials with biological systems has been characterized by harmful side effects to various cell types, necessitating their modification for safe biological applications.[5-8]

Throughout this report we will focus on two specific types of nanomaterials mainly carbon nanotubes and gold nanoparticles. These materials have been studied for decades, centuries in the case of gold nanoparticles, and therefore carry an expansive body of literature around them. Our focus here will be on the interaction of these nanomaterials with biological systems and how they can be exploited to elicit changes in their local environment. Engineered nanomaterials provide unique advantages and opportunities in several areas of medicine including therapeutics, diagnostics, imaging, and regenerative medicine.[9, 10] Finally, we report the use of a novel hybrid material which combines the unique properties of each nanomaterial for advanced drug delivery applications.

1.1 Carbon nanomaterials (CNM)

Carbon nanomaterials (CNM) encompass a wide range of carbon allotropes from sp^2 conjugated species, such as graphene, fullerenes and carbon nanotubes, to sp^3 nanodiamonds as shown in Figure 1–1.[11-13] Fullerenes take the form of spheres, ellipsoids or tubules where spherical and cylindrical fullerenes are referred to as buckyballs and buckytubes, respectively. The first observation of the buckyball family, referred to as buckminsterfullerene, is composed of 60 carbon atoms (C_{60}) and has the shape of a truncated icosahedron with 20 hexagons and 12 pentagons, similar to a soccer ball, with a diameter around 1 nm.[14] Iijima is credited with the discovery of carbon nanotubes (CNT) in 1991[15] although some claim that these structures had been observed decades earlier.[16] CNT are graphitic tubules, which can be capped with hemifullerenes at the ends, consisting of a single graphene sheet referred to as single-walled carbon nanotubes (SWNT). Additionally, these materials can also be composed of several concentric and nested tubes referred to as multi-walled carbon nanotubes (MWNT). Both types of CNT display high aspect ratios, or the ratio between the length and the diameter of the material. SWNT have diameters around 1 nm, depending on their chirality,[17] with lengths of a few microns or more. MWNT have diameters of several tens of nanometers, depending upon the number of walls, and have lengths up to several tens of microns or more. All sp^2 allotropes of carbon can be related to a parent material known as graphene.[18] Graphene was first isolated into individual sheets from stacked graphite flakes in 2004, since this discovery much progress has been made on the electrical, medical, and optical applications of graphene.[19, 20]

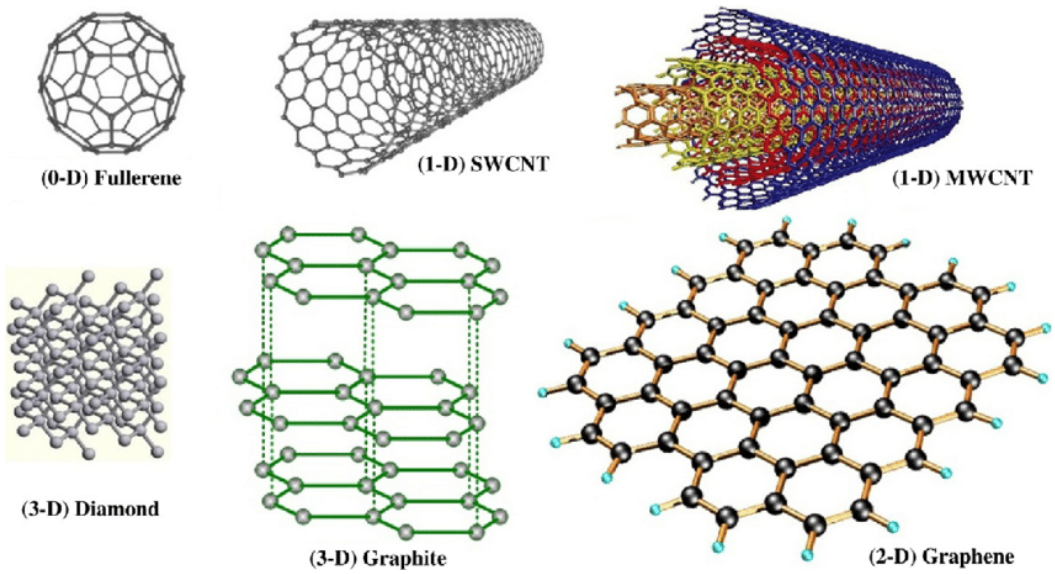

Figure 1-1 Illustration depicting the structure for various allotropes of carbon. Reprinted (adapted) from reference.[21]

Due to their small width dimensions, CNT are able to penetrate biological barriers through a reported passive "needle-like" mechanism negating the need for specific targeting and uptake ligands.[22] CNT also possess unique physicochemical properties which can be advantageous for biological applications such as strong optical absorption in the near infrared, Raman scattering, and photo-acoustic properties that widen the scope of *in vivo* applications as they can potentially be used for bio-imaging and tracing functions coupled with drug delivery.[23] CNM, specifically graphene, are characterized by large surface area and easy functionalization allowing for controlled modification of the material for a wide ranging applications. CNM also exhibit unique physical properties such as high tensile strength (up to 1 TPa), high thermal stability (up to 2800°C in vacuum), and thermal conductivity twice that of diamond.[24] CNT have been used extensively as drug carriers through either covalent modification of the CNT with therapeutic cargo,[25] or noncovalent decoration through π-π stacking for target molecules such as doxorubicin.[23] With appropriate functionalization, SWNT have been shown to rapidly clear blood circulation through

renal excretion with a half-life of several hours.[26] The retention of MWNT has been shown to be dependent on surface functionalization as well, where increasing the level of functionalization results in enhanced renal clearance while less functionalized materials are prone to renal accumulation in the liver and spleen.[27]

CNT have been synthesized through a multitude of techniques including laser ablation,[28-30] arc-discharge,[31, 32] and chemical vapor deposition (CVD).[33] These synthesis techniques rely on a thermochemical process knowns as pyrolysis where organic precursors are degraded into their atomic components at high temperatures in the absence of oxygen.[34] Once degraded, these atomic components can rearrange into the desired graphitic structures observed above. Of particular interest, CVD synthesis can be separated into two main categories, fixed-bed CVD[35, 36] and floating catalyst CVD.[37] In fixed-bed CVD, transition metal catalyst particles are deposited on a substrate and heated to high temperatures in the presence of organic precursors for the formation of CNT. This process is limited by the availability of free transition metal catalyst surface to initiate the CNT growth resulting in low yields and poor scalability.[38] To improve scalability, transition metal catalytic particles can be formed *in situ* through the decomposition of volatile metallo-organic compounds within the reactor, negating the need for substrate bound particles; this method is known as the floating catalyst method.[37] During floating catalyst CVD synthesis a reducing gas, such as H_2 is added to the synthesis in order to reduce the transition metal precursor into catalytic transition metal nanoparticles which are then used to initiate CNT growth. During this technique, transition metal nanoparticles are continuously made, through the addition of metal precursor and H_2, greatly increasing the overall yield of CNT and allowing for improved scalability.

The mechanism for CNT formation in CVD synthesis is of upmost importance to its overall physical structure and resulting chemical properties. In a fixed bed CVD synthesis, the transition

metal nanoparticles are attached to a substrate surface with CNT growth occurring through the formation of a graphitic envelope on the exposed surface. The most commonly accepted mechanism for CNT growth is due to the catalytic decomposition of the organic precursor which is initiated on the transition metal surface producing carbon and hydrogen atoms.[39] This decomposition is followed by diffusion of carbon into the metal particles until saturation resulting in precipitation of solid carbon from the metal surface.[40] At this point in the CNT synthesis, growth occurs through either a tip growth mechanism or a root growth mechanism. In a root growth process, the metal catalyst stays fixed to the substrate and CNT growth moves upward and away from the substrate. In a tip growth process, the CNT stays anchored to the substrate and the transition metal catalyst moves away from the substrate as nanotube growth proceeds. The underlying cause of these growth mechanisms is due to diffusion of the carbon through the transition metal catalyst and the interaction between the metal catalyst and the substrate. An illustrative summary of CVD synthesis growth mechanisms responsible for CNT growth is provided in Figure 1–2.

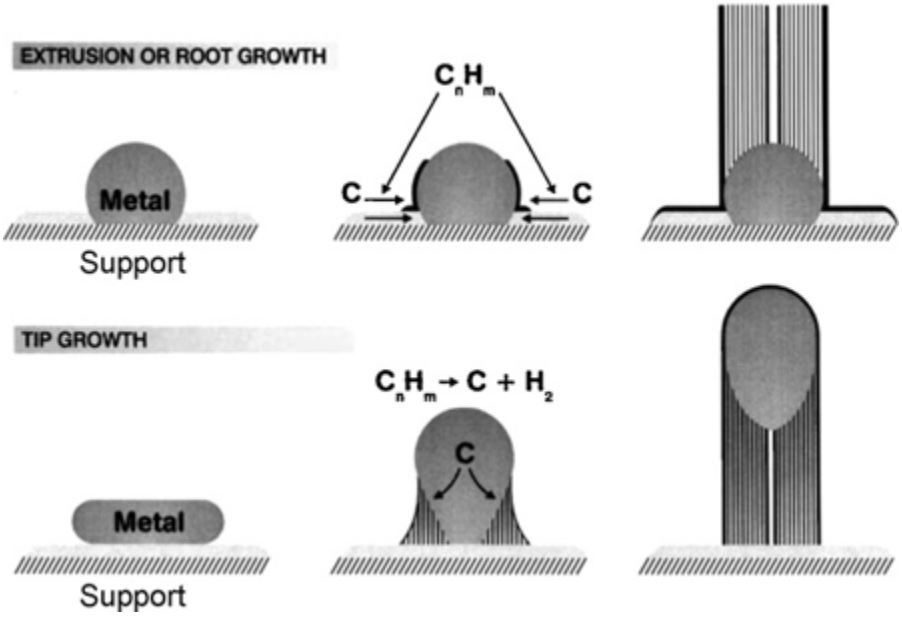

Figure 1-2 Schematic diagram of the root growth and tip growth mechanisms of carbon nanotubes. Reprinted (adapted) with permission from reference.[37] Copyright 2007 American Chemical Society.

The doping of nitrogen into CNM has been achieved through *in situ* doping during synthesis by introducing a nitrogen source directly into the CVD/pyrolysis[35, 41-43] process or post synthetic doping by chemical[44] or electrochemical[45] functionalization. Doping of CNM with nitrogen atoms alters their intrinsic properties due to interaction between the nitrogen lone-pair electrons and the graphene π-system, producing tailored electronic characteristics and controllable surface and local chemical features.[46] Incorporation of nitrogen dopants into the graphitic lattice of CNT can result in a change in morphology where the CNT becomes segmented, denoted as either bamboo[36] or stacked-cups structure.[47] The stacked-cup structure is achieved as a result of the added strain on the graphitic lattice upon the incorporation of nitrogen. When the strain from the incorporated nitrogen forces the CNT diameter to exceed the diameter of the metal catalyst particle, a fresh catalyst surface is exposed to the reactive environment allowing for the formation of a new CNT structure. The sputtered growth of nitrogen-doped CNT results in a stacked-cup

structure referred herein as nitrogen-doped carbon nanotube cups (NCNC). Differences in CVD growth mechanism and resulting NCNC morphology are summarized in Figure 1–3.

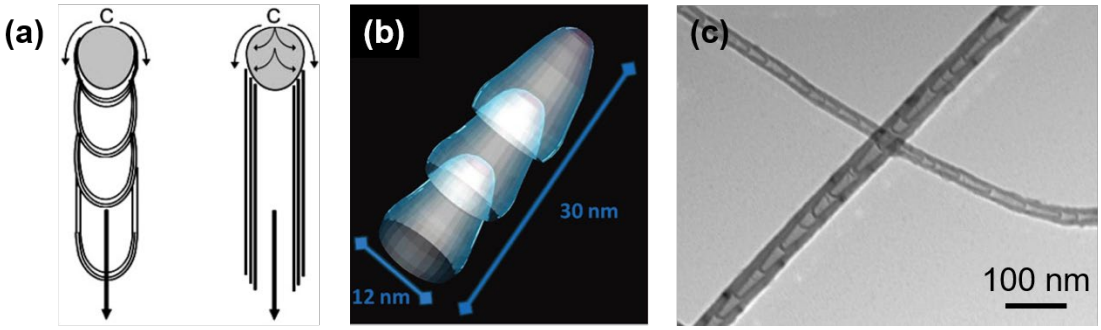

Figure 1-3 (a) Illustration showing the formation of nitrogen-doped carbon nanotube cups (NCNC) in comparison to un-doped carbon nanotubes. Reprinted (adapted) from reference.[36] Copyright 2008 Elsevier. (b) Schematic diagram of NCNC. Reprinted (adapted) from reference.[47] Copyright 2008 American Chemical Society. (c) Transmission electron microscopy (TEM) image of as-synthesized NCNC.

While nitrogen-doped carbon structures have been extensively explored for electrocatalytic applications, their biological applications have been somewhat less explored.[48] Compared to regular un-doped multi-walled carbon nanotubes, which have a continuous tubular structure with relatively long inaccessible hollow interiors, NCNC are composed of compartmented hollow structures that are held together through weak van der Waals interactions between their graphitic structures.[49] In addition to the unique cup-shaped morphology, the incorporation of nitrogen dopants has been shown to increase the cytocompatibility of the carbon structure over its undoped counterpart.[48] The incorporation of nitrogen dopants also provides initiation sites for enzymatic degradation, *vide infra*, making NCNC a unique material for drug delivery applications.[50] Overcoming the multiple interlayer non-covalent interactions can allow for separation of stacked NCNC into individual NCNC with length scales around 200 nm.[47 51] Separated NCNC with well-

defined inner cavities could be of great interest for applications in drug delivery and nano-sized containers. The improved biocompatibility of NCNC compared to un-doped MWCNT[52] and versatile surface chemistry due to the nitrogen doping could also facilitate their biomedical applications.

1.2 Gold nanoparticles (GNP)

Bulk gold has been used extensively in jewelry, currency, and electronics due to its unreactive nature and lustrous appearance which remains untarnished for thousands of years. Gold nanoparticles (GNP) attracted significant attention due to their vivid colors which are dependent upon their size and shape. The Lycurgus Cup, crafted between the 5th and 4th century B.C., illustrates this unique property as it appears red in transmitted light and green in reflected light due to the presence of colloidal GNP. In addition to their visual appeal, GNP also exhibit unique properties due to their small size, specifically in particles of sizes less than 100 nm, such as photothermal heating, surface enhanced Raman scattering (SERS), and absorption of X-ray radiation.[53] The unique properties of GNP, in addition to their small size, makes them an interesting material for a wide range of biological applications including photothermal therapy, contrast imaging agents, and drug delivery vehicles. In fact, the potential medical applications of colloidal GNP have been explored throughout history with many rudimentary therapies prescribed by physicians over the years.[54]

GNP have been observed with varying shapes and sizes due to alterations in their synthetic conditions, as shown in Figure 1–4.[55] Synthesis of GNP has been extensively explored over centuries, however most mechanisms for GNP growth require the use of a reducing agent acting

on a gold salt.[53] Depending on the strength of the reducing agent, the identity of the surface ligands, and additional ionic species in solution, GNP can take the shape of nanoprisms, nanorods, icosahedra, tetrahedron, and even atomically precise nanoclusters.[56] Other methods for GNP production have been documented including thermal synthesis, photochemical synthesis, and electrochemical synthesis.[57, 58] Of the countless synthetic parameters for GNP, one of the most investigated and reliable methods is the Turkevich method.[59] The Turkevich method utilizes trisodium citrate ($Na_3C_6H_5O_7$ or Na_3Cit) for the reduction of chloroauric acid ($HAuCl_4$) with multiple interconnected reactions determining the final GNP size.[60] With fine-tuned control over pH, ionic strength, precursor concentrations, and temperature reproducible monodisperse GNP can be obtained.

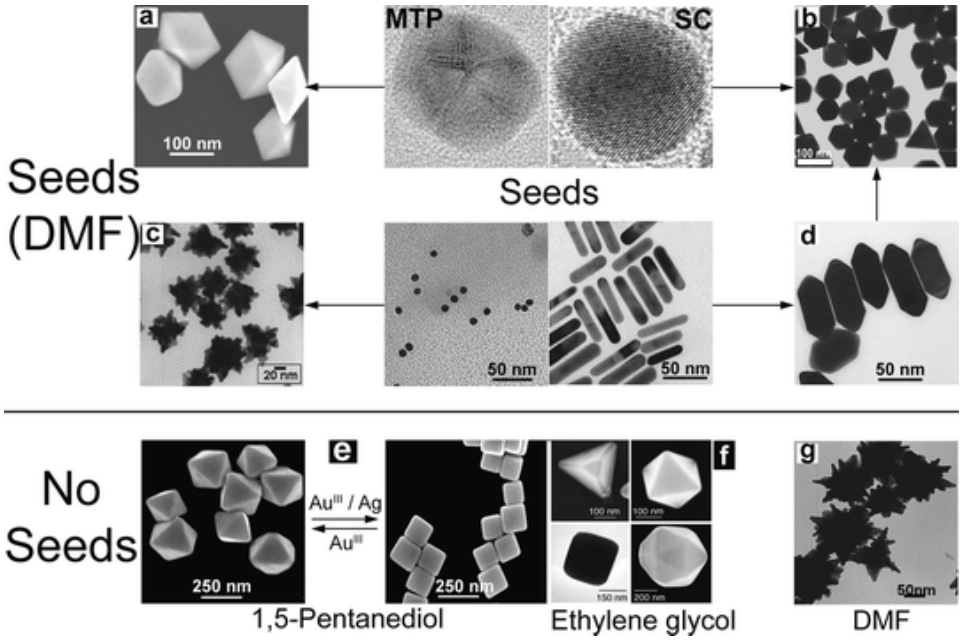

Figure 1-4 Electron micrographs of gold nanoparticles with various shapes, synthesized through dimethylformamide/polyol reduction in the presence of polyvinylpyrrolidone. In the upper panel, seeded growth is summarized, while the particles shown in the lower panel were made with no pre-made seeds. Adapted from reference.[55] Reproduced with permission of Royal Society of Chemistry.

The Turkevich method results in monodisperse particles which are electrostatically stabilized by nontoxic citrate ions. The citrate ions can be easily functionalized resulting in an avenue for surface modification for biomedical applications. However, there have been conflicting reports in the reproducibility of GNP *via* this technique.[61] The complexity and interconnected chemical reactions involved in the Turkevich method may explain the conflicted reports of monodisperse particles. The first step in the Turkevich method is the reduction of the gold precursor with trisodium citrate producing small clusters which initiate nanoparticle growth at elevated temperatures. Next, the clusters coalesce to form stable seed particles which grow into the final GNP. The remaining precursor is reduced in the electric double layer of the seed particles until depleted and the final particle size is determined. Therefore, the initial seed formation acts as the size determining step in the Turkevich method, where more seed particles result in smaller but more numerous GNP and fewer seed particles result in larger, less abundant GNP. This synthesis is summarized in Figure 1–5.

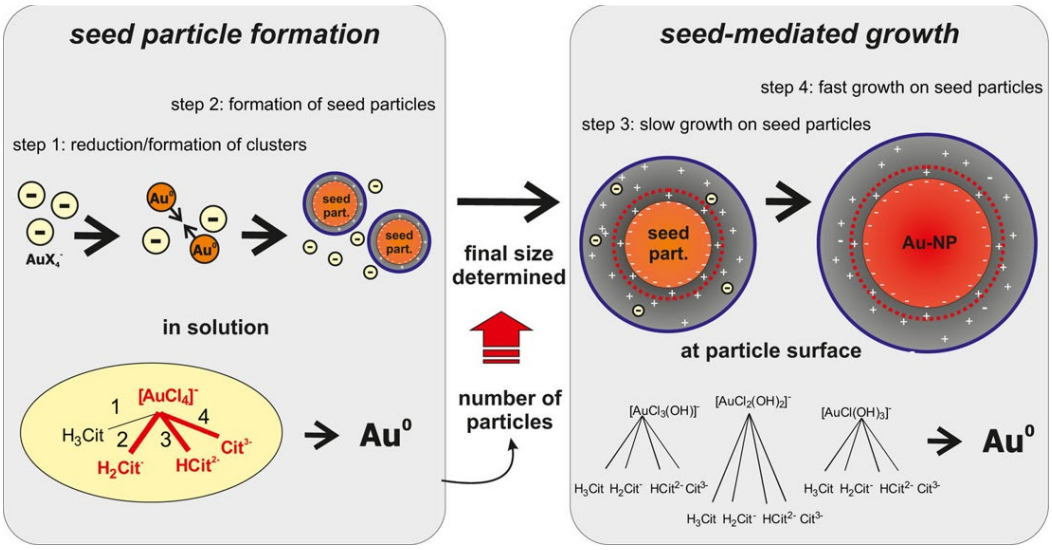

Figure 1-5 Schematic illustration of the growth mechanism of the Turkevich synthesis; during the seed particle formation $[AuCl_4]^-$ reacts with a citrate species (paths 1–4) to give Au^0 in solution; after the seed formatiomn $[AuCl_4]^-$ is not present in the reaction mixture and $[AuCl_{4-x}(OH)_x]^-$ complexes are reduced in the electric double layer of the seed particles. Reprinted (adapted) with permission from reference.[60] Copyright 2016 American Chemical Society.

As shown above, the amount of gold precursor reduced in the initial stages of the Turkevich method will have a significant effect on the resulting particle size and therefore needs to be controlled for reproducible synthesis. The origin of this initial reduction is heavily tied to the Cl^- concentration in solution and the pH of the solution as discussed below. The addition of Na_3Cit, and therefore Cit^{3-} ions results in a shift in pH towards more neutral values as the Cit^{3-} ions have the capability to react with free H^+ ions in solution. The shift in pH alters the stable species of $[AuCl_4]^-$ in solution to complexes with hydroxide; $[AuCl_{4-x}(OH)_x]^-$, where $x \geq 1$.[61] The difference in speciation of the $[AuCl_4]^-$ ions is dependent upon the concentration of both H^+ and Cl^-, and the resulting reduction of the $[AuCl_4]^-$ is affected by the state of the $[AuCl_4]^-$ species as shown in equations 1, 2, and 3.

Equation 1

$$[AuCl_4]^- + x\,H_2O \leftrightarrow [AuCl_{4-x}(OH)_x]^- + x\,H^+ + x\,Cl^-$$

Equation 2

$$[AuCl_4]^- \leftrightarrow [AuCl_3(OH)]^- \leftrightarrow [AuCl_2(OH)_2]^- \leftrightarrow [AuCl(OH)_3]^- \leftrightarrow [Au(OH)_4]^-$$

Equation 3

$$Cit^{3-} + x\,H^+ \leftrightarrow H_xCit^{(3-x)-}$$

Therefore, fine-tune control over the pH, Cl^- concentration, and the initial concentrations of the metal and reducing agent precursors are important for effective size control and GNP formation in the Turkevich method.

While free GNP synthesis is desirable for many applications, the ability to decorate CNM with GNP is of great interest for catalysis, sensing, and biomedical applications.[62, 63] While GNP can be decorated onto CNM through the use of the Turkevich method,[63] there is evidence that CNM possess the ability to reduce gold salts without the addition of an additional reducing agent.[64-66] As these technique would not require the use of Na_3Cit, the dependence upon pH and ionic strength of the synthesis mixture should be less pronounced on the GNP formation allowing for improved synthesis reproducibility. However, much like iodide ions were shown to have an effect on free GNP synthesis,[67] free bromide ions were shown to alter the formation of GNP on graphene.[65] Therefore, thorough investigations into the templated growth of GNP on carbon scaffolds are necessary for reproducibility similar to the extensive investigations performed with the Turkevich method.

Due to their small size, the electrons in GNP can be viewed as being trapped within a potential well (i.e., the particle in a box model) and show characteristic collective oscillation frequency referred to as the plasmon resonance band.[3] The collective oscillation in electrons can

be induced by electromagnetic radiation referred to as localized surface plasmon resonance which is located at 530 nm for 50 nm GNP and can be shifted depending on the size of the particle.[68] The location and shape of the plasmon resonance band is dependent upon particle size, particle shape, surface ligands, and temperature. The unique plasmonic properties of GNP can be coupled with Raman spectroscopy resulting in a phenomenon known as surface enhanced Raman scattering (SERS) which can be used for sensing applications in biological systems as shown in Figure 1–6.[54, 68] Raman spectroscopy relies on inelastic light scattering by a sample due to interaction with its inherent vibrational modes creating a unique spectrum of the sample. Raman spectroscopy benefits from low signal from water allowing for practical use in biological systems, however the low energy of molecular vibrations results in poor sensitivity. When a Raman active molecule is held in close proximity to a plasmonic particle the molecular vibrations can be increased resulting in improved Raman signals with reported sensitivities down to single molecule detection.[69, 70] This Raman enhancement can be further improved if the analyte molecule is held between 2 or more plasmonic particles resulting in a compounded "hot-spot" effect. The ability for GNP to enhance the Raman signature of nearby molecules makes them a unique material for biological sensing.

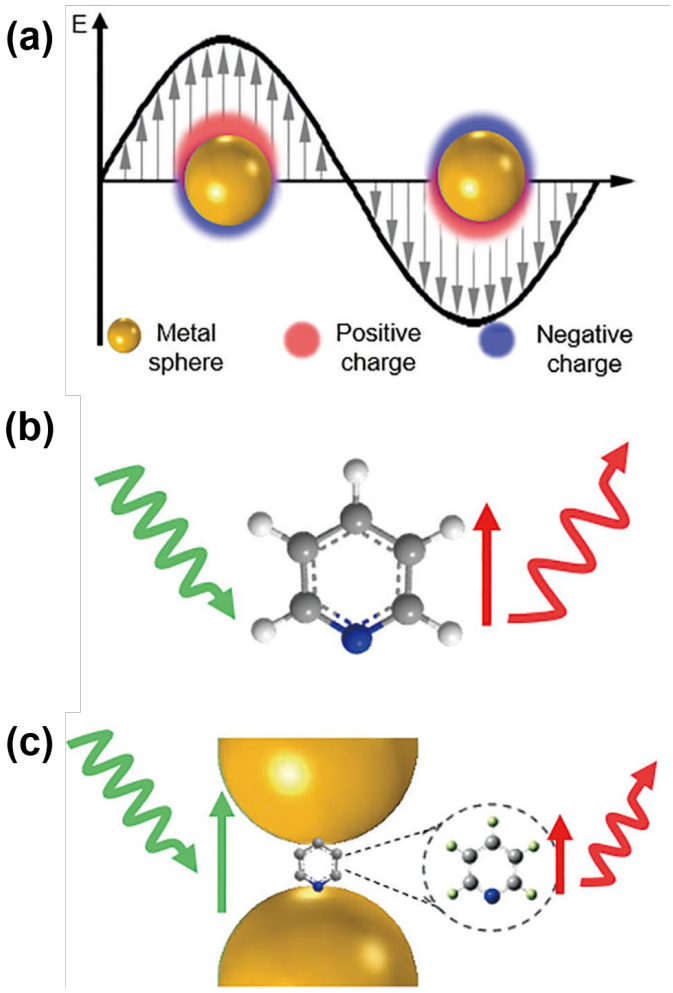

Figure 1-6 (a) Illustration of surface plasmon resonance. (b) Normal Raman and (c) electromagnetic enhancement mechanism in surface enhanced Raman scattering. Reprinted (adapted) with permission from reference.[68] Copyright 2018 American Chemical Society.

1.3 Enzymatic degradation of CNM

The unique electronic, optical, thermal, and mechanical properties of CNM have attracted significant attention in recent years in nanomedicine.[23, 71] The ultimate successful implementation of CNM for biomedical applications depends on demonstrating their superior properties over that of existing approaches, in addition to documenting their safe interaction with biological systems. A detailed understanding of the biological interactions of CNM is important from both an efficacy and safety point of view, as is the understanding of the ultimate fate of the nanomaterial in the form of accumulation, degradation, and excretion from biological systems.[72] Nanoparticles such as liposomes, dendrimers, and micelles are prone to biodegradation and often exhibit minimal harmful side effects.[73] In contrast, sp^2 hybridized CNM have been shown to be resistant to biodegradation and can have prolonged circulation times and bio-persistence.[74] The mechanisms underlying the resistance of CNM to biodegradation are important not only for their biomedical applications but also in regards to unintended exposures in occupational and environmental settings. CNT in particular have been met with skepticism for applications in drug delivery applications due to their fiber-like structure which was presumed to result in bio-persistence and therefore asbestos-like pathogenicity.[75] However, further investigations have suggested strategies to improve the biocompatibility of CNT through surface modification which can improve the susceptibility of CNT towards enzymatic degradation.

Several peroxidase-based enzymes, horseradish peroxidase (HRP), myeloperoxidase (MPO), lactoperoxidase (LPO), and eosinophil peroxidase (EPO) have been shown to effectively degrade oxidized CNM.[74, 76] These enzymes contain a ferriprotoporphyrin IX heme group as shown in Figure 1–7. In the resting state, the heme group exists in the ferric, Fe(III), form. Upon the addition of hydrogen peroxide, the heme center is converted to an oxo-ferryl iron (Fe^{4+}=O),

which can be reduced back to the ferric state by the peroxidase cycle. Biproducts of the enzymatic cycle include hypohalite which has been shown to induce CNT degradation as well.[6] In the presence of peroxidases, CNT which contain oxygen functionalities or defect sites are able to undergo effective degradation while pristine CNT undergo no such degradation.[77] These results can be used to explain the previous observations that increased levels of CNT functionalization result in improved clearance from the renal system. Furthermore, degraded CNT were shown to induce less pulmonary inflammation in mice illustrating that the level of degradation has a direct correlation to the inflammatory response of CNT *in vivo*.[6] The improved degradation of functionalized CNT, as opposed to pristine CNT, is presumed to be due to electrostatic interactions between the negatively charged oxidized CNT and the positively charged domains of the peroxidase enzymes.[77] The rate of enzymatic degradation is also correlated to the level of oxidation and/or defect sites on the CNT. CNT with increased levels of oxidation were found to degrade at a faster rate than less oxidized samples with the ultimate product being CO_2.[50] Finally, the incorporation of nitrogen-defects has also been shown to initiate the degradation of CNT. In addition to peroxidase-based degradation of CNT, other biologically relevant machineries have been shown to induce effective degradation. Oxidative mechanisms driven by NADPH oxidase, which produces superoxide, and the inducible isoform of nitric oxide synthase (iNOS), which produces peroxynitrite ($ONOO^-$) have been shown to effectively degrade CNT. [78]

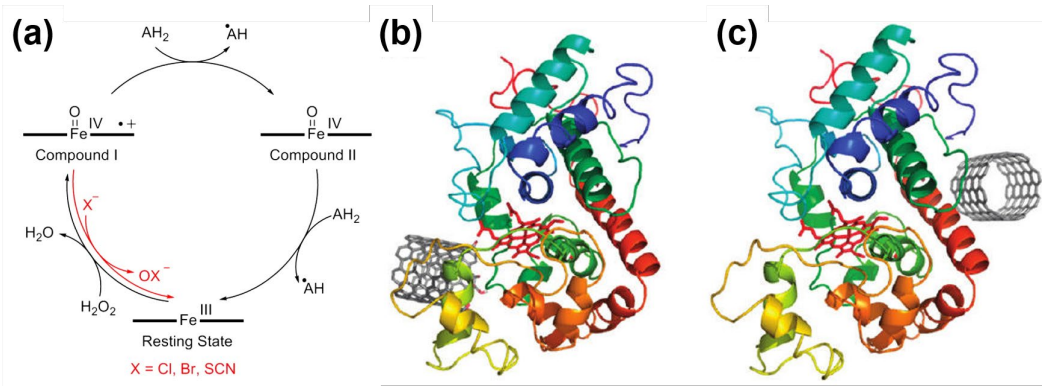

Figure 1-7 (a) Catalytic peroxidase cycle for peroxidase enzymes, compound I is reduced directly to the resting state *via* conversion of halide to hypohalite. Molecular modeling of the most preferred binding site on HRP for (b) carboxylated and (c) pristine SWNT. Panel a reprinted (adapted) from reference.[74] Copyright 2013 Elsevier. Panels b and c reprinted (adapted) from referene.[77] Copyright 2009 American Chemical Society.

1.4 Myeloid-derived suppressor cells (MDSC)

Cancer is the second leading cause of death in developed countries with over 12 million new cases diagnosed annually worldwide and the expected number of people suffering from cancer reaching 25 million annually in the next two decades.[79] Recent studies have highlighted the important role of myeloid-derived suppressor cells (MDSC), a heterogeneous population of immature myeloid cells, in regulating the antitumor immune response and tumor progression. MDSC can be broadly defined as myeloid cells which have not been fully differentiated into mature myeloid cells such as macrophages, dendritic cells (DC), or neutrophils.[80] MDSC are produced in bone marrow and released into the bloodstream where they eventually accumulate in the tumor and lymphoid organs. Under normal physiological conditions, MDSC are not found in circulation and accumulation and detection of MDSC is only observed under pathological conditions. The accumulation of MDSC in tumor-bearing hosts, inhibit effector T cells and thus prevent the formation and execution of an effective antitumor immune response. Recent studies have shown that MDSC also function to promote tumor metastasis, tumor-dependent angiogenesis, and provide tumor resistance to immunotherapy, antiangiogenic drugs and chemotherapy.[81] Counteracting MDSC activities significantly contributes to antitumor efficacy and prolongs survival of tumor bearers.[82, 83] However, clinical applicability of cytotoxic drugs for depleting immune regulators is limited by cumulative toxicity, non-specific effects, immunosuppression and possible pro-metastatic activity.[84-87]

MDSC accumulate in tumor-bearing hosts and consist of two populations: polymorphonuclear cell (PMN-MDSC) and monocytic cells (M-MDSC).[88, 89] PMN-MDSC are similar to granulocytes such as neutrophils and eosinophils while M-MDSC are similar to monocytes which have the ability to differentiate in macrophages and DC. DC are antigen-

presenting cells which are important for communicating between the innate and adaptive arms of the immune system. DC cells initiate the pathways which are responsible for the production and accumulation of B cells and T cells. Both PMN-MDSC and M-MDSC have potent immune suppressive activity and have been implicated in promotion of tumor angiogenesis, tumor cell invasion, and metastasis.[90] Tumor-associated MDSC, unlike normal immature myeloid cells, lose the ability to differentiate into conventional DC,[91] acquire the ability to differentiate into immunosuppressive regulatory DC,[92] induce differentiation of tolerogenic regulatory T cells (Treg),[93, 94] support polarization of macrophages into protumorogenic type 2 cells (M2),[95] and suppress activity of innate immune cells like natural killer (NK) cells as shown in Figure 1–8.[96, 97] NK cells are specifically programmed to destroy tumor cells and their suppression is directly related to the uninhibited growth of tumor masses.

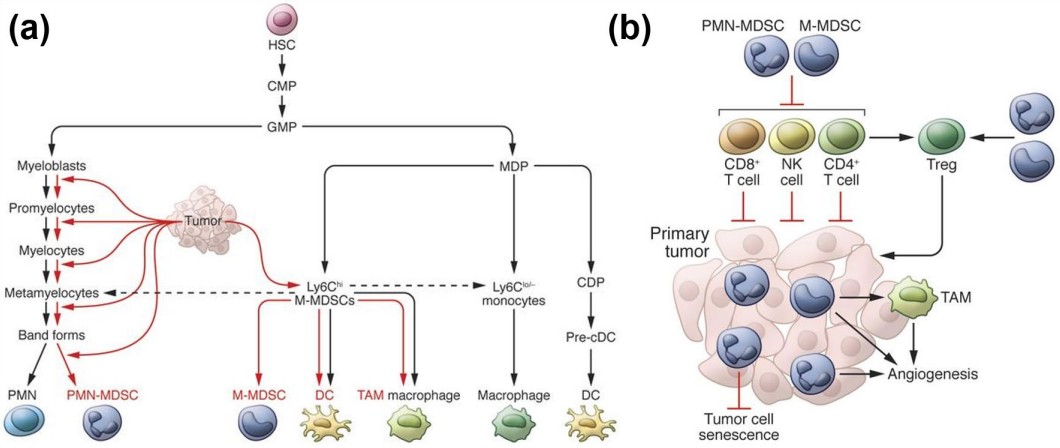

Figure 1-8 (a) Differentiation of myeloid-derived suppressor cells (MDSC) in wild-type mice (black) and tumor-bearing mice (red). (b) Interaction of MDSC with the tumor microenvironment. Reproduced (adapted) with permission from reference.[80] Copyright 2015 American Society for Clinical Investigation.

Activated MDSC are characterized by an unusually robust co-expression of NADPH oxidase, ARG-1, iNOS, and MPO creating an exceptionally potent source of pro-oxidants. NADPH oxidase (particularly NOX2) catalyzed production of superoxide, combined with high levels of $NO^{\cdot}$ production can yield $ONOO^{-}$. Dismutation of superoxide creates H_2O_2, a source of oxidizing equivalents for MPO, which facilitates generation of hypochlorous acid (HOCl). These reactive oxygen and nitrogen species, byproducts of the combined activity of iNOS, MPO, and NOX2, in addition to suppressing activity and longevity of different subsets of immune cells in the tumor milieu,[98] have been shown as effective biodegradation mechanisms of carbonaceous nanoparticles.[8, 99] This arsenal of $ONOO^{-}$ and HOCl-producing enzymatic machineries, uniquely characteristic of MDSC, by far exceeds the capacities of macrophages or neutrophils in generating $ONOO^{-}$ or HOCl, respectively, as carbonaceous nanoparticle biodegradation reagents. The enzymatic activity of MDSC represents an attractive way to influence their differentiation.

2.0 Manipulation of nitrogen-doped carbon nanotube cups (NCNC)

2.1 Introduction

NCNC are characterized by a unique cup−shaped morphology which is attractive for drug delivery applications. For effective use of NCNC, the material must first be separated into individual and short stacked cup segments which undoubtedly affects their chemical characteristics. Additionally, the synthesis of NCNC requires the use of transition metal catalysts where residual metal remains within the NCNC and can therefore alter the interaction of the material with biological systems. This chapter compiles the results of multiple projects illustrating the role residual metal catalyst plays in the interaction of NCNC with H_2O_2, and how the technique used for separation of NCNC alters their chemical functionalities.

To address the role residual metal catalyst plays for H_2O_2 reaction with NCNC, NCNC were synthesized from ferrocene, nickelocene, and cobaltocene metal precursors with their resulting electrocatalytic activity towards the oxygen reduction reaction (ORR) quantified. While the ORR results have implications for electrocatalyst design and fuel cell technology, the activity of the synthesized materials could potentially be used to predict which material has the highest potential for enzymatic degradation involving hydrogen peroxide. Computational results on the binding energy of the reactants, intermediates, and products of the ORR are discussed along with electrocatalytic characterization of NCNC response to H_2O_2. Since H_2O_2 is a crucial component to the enzymatic degradation of CNM, determining the synthesis conditions which increase the binding of H_2O_2 can improve degradation rates of NCNC

To address how the techniques used for separation of NCNC alter their chemical functionalities, two separate techniques will be explored. The separation of adjacent NCNC through bath sonication in alkali metal salts is performed in order to maintain the inherent functionalities of the NCNC. Conversely, intense probe-tip sonication is performed in order to disrupt the intermolecular forces between adjacent cups, however the high energy output further alters the nitrogen functionalities distributed on the separated cups. In addition to modifying the NCNC structure, the process of functionalizing nitrogen-doped carbon materials with plasmonically active GNP is also explored. The resulting material is able to enhance the inherent Raman signature of interacting molecules providing an avenue to prove loading of NCNC with desired cargo.

The material contained in this chapter was published in three research articles and have been reprinted (adapted) with permission from the respective publisher.

1. The Effect of Metal Catalyst on the Electrocatalytic Activity of Nitrogen−Doped Carbon Nanotubes. *The Journal of Physical Chemistry C* **2013**, *117*(48), 25213–25221, Copyright © 2013, American Chemical Society. Reference[100] in the bibliography section.

List of Authors: Yifan Tang, Seth C. Burkert, Yong Zhao, Wissam A. Saidi, and Alexander Star

Author Contributions: All authors contributed to the design of experiments and writing of the paper. YT, SCB, and YZ synthesized NCNC materials using CVD. YT and SCB performed TEM and electrochemical characterization. SCB performed XPS characterization. WAS performed quantum chemical calculations.

2. Efficient Separation of Nitrogen−Doped Carbon Nanotube Cups. *Carbon* **2014**, *80*, 583–590, Copyright © 2014, Elsevier. Reference[101] in the bibliography section.

List of Authors: Yifan Tang, Yong Zhao, Seth C. Burkert, Mengning Ding, James E. Ellis, Alexander Star

Author Contributions: All authors contributed to the design of experiments and writing of the paper. YT, YZ synthesized the NCNC material using CVD. YT and SCB conducted separation experiments. YT characterized the materials using TEM. YZ performed Raman characterization. SCB performed XPS characterization.

3. Oxidative Unzipping of Stacked Nitrogen-Doped Carbon Nanotube Cups. *ACS Applied Materials and Interfaces* **2015**, *7*(20), 10734–10741, Copyright © 2015, American Chemical Society. Reference[102] in the bibliography section.

List of Authors: Haifeng Dong, Yong Zhao, Yifan Tang, Seth C. Burkert, and Alexander Star

Author Contributions: All authors contributed to the design of experiments and writing of the paper. HD and YZ synthesized the material. HD, YZ, and YT performed microscopic and spectroscopic characterization. HD, YT, and SCB performed electrochemical characterization. SCB performed XPS characterization.

Nitrogen-doped carbon nanomaterials have attracted significant attention in recent years because of their tailored electrical and electrochemical properties.[103-105] They have been shown to be promising substitutes for expensive Pt based catalysts in fuel cells for the ORR.[106, 107] The CVD synthesis of nitrogen-doped carbon nanomaterials typically involves the use of transition metal catalysts,[108, 109] which have well-known catalytic activity on their own[110] and might affect the electrochemical catalytic activity above parts per million (ppm) concentrations.[111] An increasing body of evidence suggests that the previously reported unique properties of carbon nanomaterials are a result of interactions between the carbon scaffold and residual metals from synthesis procedures.[112, 113] Studies have shown that residual metal is often bound to nitrogen species causing

a metalloporphyrin-like active site.[114, 115] While the role of residual metal catalyst is important in electrocatalytic reactions, the residual metals could also have a substantial effect on the biological interactions of carbon nanomaterials.[116]

To determine the effect residual metal catalyst plays in observed NCNC properties, we synthesized NCNC using ferrocene, nickelocene, and cobaltocene and tested their resulting electrocatalytic properties towards the ORR. ORR not only has important implications for fuel cell technology but is also prevalent in biological reaction mechanisms.[117] In fact, nitrogen-doped carbon nanotubes with high ORR activity have been shown to interact strongly with free H_2O_2 with a sensitivity nearly 100 times better than undoped CNT.[118] The ORR can proceed through either a one-step 4-electron mechanism as shown in equation 4, or through a two-step 2-electron mechanism as shown in equations 5 and 6.[119]

Equation 4

$$O_2 + 4H^+ + 4e^- \rightarrow 2H_2O$$

Equation 5

$$O_2 + 2H^+ + 2e^- \rightarrow H_2O_2$$

Equation 6

$$H_2O_2 + 2H^+ + 2e^- \rightarrow 2H_2O$$

Due to the involvement of H_2O_2 in the enzymatic degradation of NCNC, understanding the mechanism for ORR on NCNC synthesized from different metal precursors could be used to identify the ideal starting material for effective enzymatic degradation. Unlike previous work, where only Fe-catalyzed nitrogen-doped carbon nanotubes created the stacked cup structure,[36] all three synthesized nitrogen-doped carbon nanotubes formed the unique structure. Electrochemical testing results demonstrated that NCNC synthesized from ferrocene have improved ORR activity over NCNC synthesized from nickelocene or cobaltocene in terms of the reduction half-wave

potential and current. The detailed ORR mechanism shows that NCNC[Ni] demonstrate an almost 4-electron ORR reduction pathway while NCNC[Fe] and NCNC[Co] show a combination of 2-electron and 4-electron mechanisms with NCNC[Fe] illustrating the largest 2-electron activity. The observed difference in their performance supports the hypothesis that the ORR mechanism can be controlled through changing the metal catalyst utilized during material synthesis. The electrochemical results are combined with computational calculations to determine the binding energy of the ORR reaction intermediates, mainly H_2O_2, to hypothesize the propensity for enzymatic degradation. In addition to NCNC[Fe] showing the highest selectivity for 2-electron reduction of oxygen, it also has the strongest binding affinity for the H_2O_2 reaction intermediate and electrochemical response to H_2O_2. The results of this investigation indicate that NCNC should be synthesized from ferrocene to produce cups with the largest ability for enzymatic degradation.

While NCNC have impressive electrocatalytic activity, separating stacked NCNC into individual cups is an attractive way to further manipulate their morphology, providing additional opportunities for their application. Several methods have been reported to date on the separation of stacked-cup shaped carbon nanotubes, including grinding with mortar and pestle,[47, 120] oxidative treatment,[121] bath sonication[122] and probe-tip sonication.[51, 123] However, each of these methods has their limitations. Grinding with mortar and pestle is a labor-intensive technique which provides poor yields and unsatisfactory separation results. Oxidation treatment requires harsh chemicals[124] and complicated instrumentation.[121] The bath sonication method still requires a pre-oxidation step by heating the materials in air at 500 °C.[122] Probe-tip sonication, especially when combined with oxidative treatment, is a promising technique that affords separated NCNC with lengths less than 200 nm.[124] However, the oxidation step alters the surface functionalities, as indicated by the increase in Raman D/G ratio and higher oxygen content measured by EDX spectra.[51, 123] The

change in surface functional groups could greatly diminish many of the characteristic properties that make these materials desirable for improved applications. The process of oxidation and probe-tip sonication will also be explored in this chapter. Lithium intercalation has been greatly studied due to the unique electronic property changes upon intercalation as well as the potential for lithium storage.[125] This intercalation process has been shown to increase intergraphitic distance and similar intercalation processes may be able to separate NCNC. Furthermore, it has been reported that potassium ions, in conjunction with probe-tip sonication, have been able to separate graphite layers through a facilitated intercalation mechanism.[126] However, probe-tip sonication has been shown to be destructive towards the graphitic lattice of carbon nanomaterials.[127]

We report a novel separation method to convert stacked NCNC into separated cups by simple bath sonication in concentrated KCl solution for 150 hours. Using this method, we achieved effective separation of NCNC with an average length of ~ 180 nm while preserving the pristine surface structure and functionalities which is not seen in analogous probe-tip sonication methods. This length scale is of great interest as nanoparticles are readily taken up into the tumor microenvironment through the enhanced permeability and retention (EPR) effect at length scales less than 200 nm.[128] We determine that the presence of high concentration potassium cations is vital for the effective separation. We believe that adjacent NCNC are separated through a process of potassium intercalation which has been previously exploited for exfoliation techniques.[129] By separating NCNC through this gentle bath sonication method the NCNC retain their inherent functionalities.

Further manipulation of NCNC can result in new materials with unique applications. For instance, oxidative longitudinal unzipping of carbon nanotubes has been shown to effectively produce graphene nanoribbons (GNR) upon reaction with sulfuric acid and potassium

permanganate.[130] This complete unzipping has been further demonstrated to produce nitrogen-doped GNR from nitrogen-doped CNT.[131] To further explore the properties of NCNC, we started with stacked NCNC and separated them through probe-tip sonication to compare to the salt separated NCNC. Unlike the intact nitrogen functionalities of salt separated NCNC, the resulting probe-tip separated NCNC have altered nitrogen functionalities which may be of interest for the seeding of gold nanoparticles which will be explored in Chapter 3. To test the proof of concept for this idea, probe-tip separated NCNC were unzipped through reaction with sulfuric acid and potassium permanganate. When exposed to the unzipping conditions, separated NCNC are completely unzipped to produce nitrogen-doped graphene nanosheets (GNS). GNS have been previously synthesized by electrochemical exfoliation[132] or hydrothermal cutting of graphene sheets.[133] Although nitrogen doping of GNS is typically performed by a post synthetic step,[134] our approach provides a facile synthetic route to nitrogen-doped GNS by direct unzipping of NCNC.

SERS has developed into an extremely useful technique for the detection of low concentration chemicals and biomolecules.[135] SERS is achieved when noble metal nanoparticles are in close proximity to Raman-active molecules, thus inducing dipole moments that enhance the inherent Raman signatures While free metal nanoparticles are able to induce SERS, it has been found that templating nanoparticles on a substrate, given optimized gaps between metal nanoparticles, allows for more sensitive and consistent SERS measurements, although most current fabrication techniques for SERS substrates are expensive and require complex instrumentation.[136, 137] Moreover, graphene sheets have been explored in SERS applications as support for noble metal nanoparticles.[138, 139] The doping of nitrogen atoms enhances the electronic structure of graphene for SERS[140] and promotes gold nanoparticle binding affinity.[51] Here, the localized reactive sites of doped nitrogen atoms in the completely unzipped GNS were employed

to functionalize with GNP to form a GNS/GNP hybrid composite, which exhibits efficient SERS detection of Rhodamine 6G, displaying potential application in chemical sensing.

2.2 Experimental section

2.2.1 Synthesis of NCNC

NCNC were prepared using a floating catalyst CVD synthesis using a three-zone Lindberg/Blue furnace and a 1 inch diameter quartz tube. NCNC were synthesized by injecting a liquid precursor consisting of 0.75 wt% of metallocenes (ferrocene, nickelocene, or cobaltocene) 10 wt% of acetonitrile, and 89.25 wt% of xylenes at a rate of 1 mL/hour with carrier gases of Ar at 127 sccm and H_2 at 38 sccm. The first zone of the furnace was used for metallocene evaporation at temperatures between 250°C and 300 °C, and the growth was carried out in the second and third zone for 60 minutes at 800°C for NCNC[Fe] and NCNC[Co], and 750°C for NCNC[Ni]. The NCNC synthesized during different CVD runs were collected from a quartz plate placed in the quartz tube in the growth zones. Samples from several CVD runs were evenly mixed together as the initial stock for all separation techniques.

2.2.2 Electrochemical characterization of NCNC

Rotating ring-disk electrode (RRDE) voltammetry and chronoamperometry measurements were performed using a CHI 7042 Bipotentiostat (CH Instruments, Austin, TX). A Pt wire electrode (CHI 115) and an Ag/AgCl (CHI 111, 1 M KCl) electrode were used as the counter and

reference electrode, respectively. All potentials are reported versus the reference electrode. The electrodes were purchased from CH Instruments, Austin TX. The RRDE was purchased from Pine Instrument Company (AFE7R9GCPT; reported collection efficiency, N = 0.37) and contains a glassy carbon (GC) disc and Pt ring electrode. RRDE experiments were carried out on an modulated speed rotator electrode.

A GC electrode (CHI 104, GC area 0.0707 cm^2, total area 0.196 cm^2) or RRDE (GC disk area 0.2475 cm^2) was carefully polished with gamma alumina powder (0.05 μm, CH Instruments) until a mirror finish was obtained. Then the electrode was rinsed and sonicated with plenty of double distilled water to remove any alumina residues and finally dried under N_2. Catalyst ink was made by dissolving 1 mg of NCNC in a solvent mixture of 992 μL of ethanol and 8 μL of 5% Nafion by sonication for at least 30 minutes to give a concentration of 1 mg/mL and 0.04% Nafion. A 20 μL sample of catalyst ink was then dropcast on the GC electrode or the GC part of the RRDE and allowed to air-dry.

Before electrochemical testing began, the working electrodes were first treated by bulk electrolysis in 50 mM phosphate buffer solution (pH = 7.2) at 1.7 V to remove any bulk metal catalyst residue and activate the electrode materials, followed by thoroughly rinsing with double distilled water. For RRDE voltammetry, linear sweep voltammetry (LSV) was performed using a modified RRDE in O_2 saturated 0.1 M KOH solution at a scan rate of 0.05 V/s and rotating speed of 1400 rpm, while the Pt ring was polarized at +0.5 V for oxidizing H_2O_2. The tests were repeated three times to confirm the reproducibility of the process. The collection efficiency of the RRDE was confirmed by testing in 10 mM $K_3Fe(CN)_6$ solution with 0.5 M KNO_3 as the supporting electrolyte. Chronoamperometric measurements were done using a three-electrode configuration

in 0.1 M KOH solution with the working electrode being held at – 0.3 V. Current was measured in response to 1 mM aliquots of hydrogen peroxide to NCNC[Fe], NCNC[Ni], and NCNC[Co].

2.2.3 Quantum chemical calculations

The quantum chemical calculations were carried out using the all-electron FHI-aims program,[141] where we employed spin-polarized Perdew-Burke-Ernzerhof exchange-correlation functional[142] in conjunction with DFT+vDW dispersion corrections.[143] The Kohn-Sham wave functions were expanded using a tier-1 numerical atom-centered basis sets.[144] We modeled the NCNC[M] system using nitrogen and metal doped graphene in a metalloporphyrin-like configuration. The graphene sheet was modeled using a supercell with a 4 × 4 repetition of the unit cell and 20 Å to mitigate the spurious interactions along the nonperiodic directions.

2.2.4 Salt separation of stacked NCNC

5 mg of ferrocene synthesized NCNC were suspended in 25 mL of 32 wt% KCl solution. The mixture was sonicated in a Branson 1150 bath sonicator at a power of 80 W for 150 hours. As sonication time increased the temperature of the water bath increases so ice was added in order to keep the temperature close to room temperature and to compensate the evaporated water level. In order to remove the salt, the products were centrifuged at 11,000 rpm for 1 hour with an Eppendorf centrifuge 5804 and the NCNC pellet was re-suspended in DI water. A centrifugation using a Fisher Scientific centrifuge model 228 (maximum speed 3400 rpm) for a pulse of 45 seconds was performed with the supernatant collected and centrifuged twice more, or alternatively low

concentration 2% HF washing was done, in order to remove glass particles shed from the glass container during the long sonication times.

2.2.5 Probe-tip sonication separation of stacked NCNC

5 mg of ferrocene NCNC were transferred to a 3:1 mixture of 95-98% sulfuric acid and 68% nitric acid (20 mL). The mixture was then sonicated in a Branson 1510 bath sonicator at a power of 80 W for 4 hours at room temperature. Subsequently, 80 mL of water was added and the material was collected by filtration using a polytetrafluoroethylene (PTFE) membrane filter (200 nm pore size), washed thoroughly with water, and dried overnight under vacuum at 60°C. The resulting oxidized NCNC (o-NCNC) were processed into separated NCNC through probe-tip sonication. Briefly, the o-NCNC aqueous solution (0.1 mg/mL) was sonicated by a 500 W probe-tip sonicator (Fisher Scientific FB505) for a total of 8 hours (30 seconds on and off) in an ice bath. For typical unzipping of separated NCNC, 2 mg of separated NCNC were added to 2 mL of 98% sulfuric acid and the mixture incubated for 18 hours. Subsequently, 10 mg of $KMnO_4$ was gradually added to the solution while the temperature was kept at 65°C for 2 hours. The reaction was then quenched by the addition of 10 mL of ice water containing 125 µL of 30% H_2O_2 solution. The solution was filtrated through a PTFE membrane (200 nm pore size), and the solid was washed with 5% HCl solution three times (20 mL each time) and water three times (20 mL each time). The final product was dried in a vacuum to obtain the GNS.

2.2.6 GNP functionalization and surface-enhanced Raman characterization

About 5 mL of 0.005 mg/mL GNS were added with 250 µL of 1 mg/mL $HAuCl_4$ solution, and the mixture stirred on a hot plate at 70°C for 20 minutes. Then 150 µL of 1 wt% trisodium citrate solution was added dropwise and the reaction was stirred for another 2 hours. The GNP-functionalized GNS were collected by centrifugation at 3400 rpm and resuspended in ~1 mL of water. Rhodamine 6G (R6G) with different low concentration were added into the GNS solution, and 20 µL was drop-cast on a glass slide for Raman spectroscopy.

2.2.7 Material characterization

Low-resolution transmission electron microscopy (TEM) images were obtained with a Phillips/FEI Morgagni at an accelerating voltage of 80 kV. Samples were drop-cast on a lacey carbon TEM grid (Pacific Grid-Tech) and allowed to dry overnight. X-ray photoelectron spectroscopy (XPS) was obtained with a Thermo Scientific K-alpha X-ray photoelectron spectrometer using monochromated Al Kα X-rays as the source. The sample spot size was 400 µm. Charge compensation was provided by a low energy electron source and Ar^+ ions. Survey scans were collected using a pass energy of 200 eV and high-resolution scans were collected using a pass energy of 50 eV. Raman spectra were collected on a Reinshaw inVia Raman microscope with an excitation wavelength of 633 nm with a scan wavelength range from 1000 to 2000 cm^{-1} at 10% laser power (maximum 17 mW) with 15 second exposure time. Samples were drop-cast on a quartz slide and dried prior to characterization.

2.3 Results and discussion

NCNC were synthesized using a floating catalyst CVD method at 800°C for NCNC[Fe] and NCNC[Co] and 750°C for NCNC[Ni] under the carrier gases of Ar and H_2 with xylenes as the carbon source and 10% acetonitrile (by mass) as the nitrogen source. It should be noted that the difference in CVD temperature for NCNC[Ni] was due to quality and quantity of the resulting structure. NCNC[Ni] grown at 800°C did not readily form the stacked cups structure desired. Ferrocene, nickelocene, cobaltocene were used as catalysts to synthesize NCNC from the corresponding transition metals. The products were denoted as NCNC[Fe], NCNC[Ni], and NCNC[Co], respectively. Metallocenes were chosen as the metal catalyst in order to achieve consistent CVD synthesis. Unlike previous reports,[36] stating that only Fe catalyst tends to form the stacked cups structure, whereas Co or Ni catalysts form a straight hollow tube structure, in our synthesis all three catalysts produced NCNC with a well-defined stacked-cup structure as observed by TEM in Figure 2–1. The well-defined stacked-cup structure for all three materials can be attributed to the floating catalyst CVD method by liquid injection as compared to the fixed-bed CVD method in analogous reports. Prior syntheses[35, 36] relied on transition metal catalyst deposited on alumina or silica substrate, where the stacked-cup structure can only occur with Fe catalysts due to the formation of stable metal carbides at the Fe particle surface. The formation of iron carbides around the surface of the Fe particle produces a graphitic envelope which eventually slides off the particle revealing a fresh Fe surface for the graphitic envelope to reform. This subsequent reforming of the graphitic envelope causes a sputtered growth resulting in the stacked-cup structure.[36] Nickel and cobalt however do not form stable metal carbides and the graphitic envelope is not produced in their solid substrate syntheses. However, the CVD results are quite sensitive to the growth conditions, as similar bamboo-like growth results for CNT have been observed on Ni

nanoparticles.[145] In this liquid injection CVD synthesis the catalyst particles are more evenly dispersed throughout the carbon source allowing for graphitic envelope formation resulting in stacked-cup structure. The resulting NCNC have similar diameter (25–50 nm) and length (μm range) regardless of the identity of the catalyst precursor. Additionally, the resulting NCNC samples show a similar nitrogen content of 1.0 atomic % as shown in Figure 2–2.

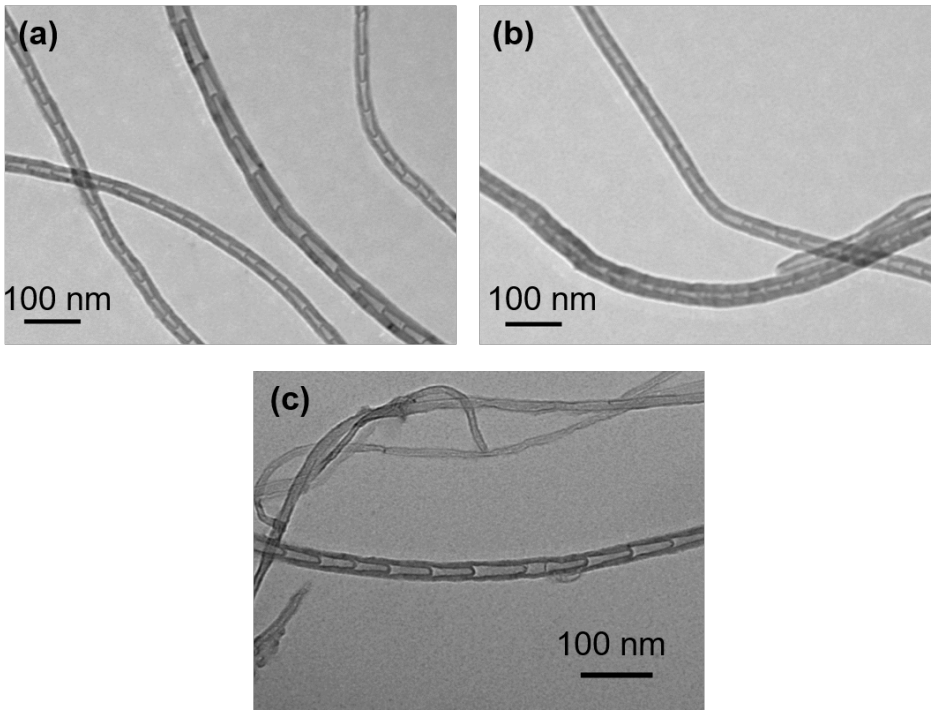

Figure 2-1 Transmission electron microscopy images of (a) NCNC[Fe], (b) NCNC[Ni], and (c) NCNC[Co]. Reprinted (adapted) with permission from reference.[100] Copyright 2013 American Chemical Society.

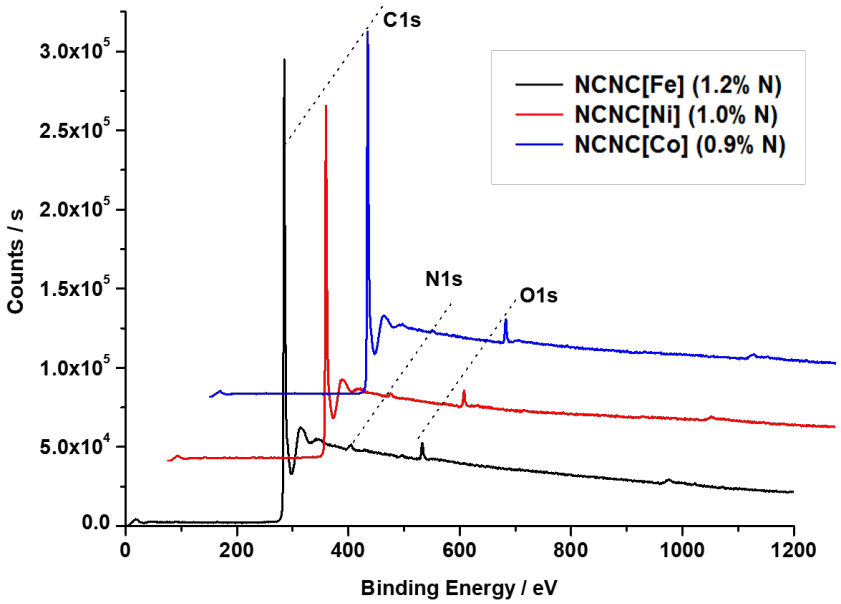

Figure 2-2 Survery X-ray photoelectron spectroscopy of NCNC[Fe] (black), NCNC[Ni] (red), and NCNC[Co] (blue); nitrogen content is reported in the legend. Reprinted (adapted) with permission from reference.[100] Copyright 2013 American Chemical Society.

NCNC[Fe], NCNC[Ni], and NCNC[Co] were made into a catalyst ink and drop-cast on a GC electrode for RRDE and chronoamperometric characterization. Prior to electrochemical characterization, an electrochemical activation process was performed in order to remove bulk metal catalyst not incorporated into the active sites of the NCNC. The removal of bulk metal residue has been shown previously not to affect the intrinsic catalytic activity of CNM.[146] RRDE was performed on the NCNC materials to determine their catalytic activity toward the ORR and determine their electron transfer mechanism, as shown in Figure 2–3. RRDE shows that NCNC[Fe] has the highest ORR activity due to its more positive reduction potential and highest reduction current. It is expected that the residual metal catalyst and nitrogen dopants can from complex structures analogous to metalloporphyrins which account for the difference in ORR activity.[147-149] Among different metalloporphyrin-based materials tested as ORR catalysts, iron

porphyrins have been found to be more active than nickel-porphyrins.[150] High-resolution TEM and electron energy loss spectroscopy imaging results suggest a positive correlation on the close spatial relations between iron and nitrogen atoms, which could be the Fe-porphyrin-like active sites.[44] Although similar imaging studies with Ni and Co have not been performed it is a safe assumption that Ni and Co would also readily form Ni-Porphyrin-like and Co-porphyrin-like active sites. Analogous catalyst syntheses have been performed with Fe-, Ni-, and Co- porphyrin precursors in order to mimic the hypothesized active site for ORR.[151, 152]

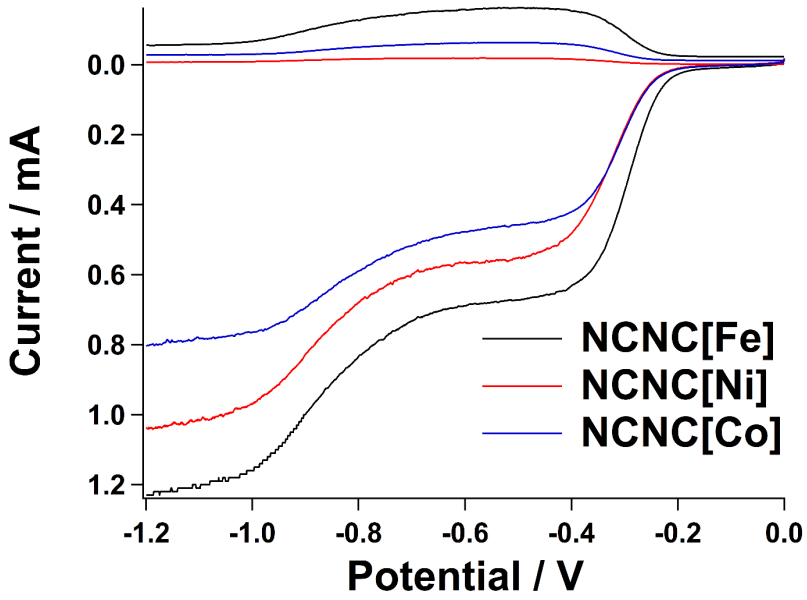

Figure 2-3 Rotating ring disc voltammograms of NCNC[Fe] (black), NCNC[Ni] (red), and NCNC[Co] (blue) for the oxygen reduction reaction in 0.1 M KOH at arotating speed of 1400 rpm. The Pt ring electrode was held at +0.5 V. Reprinted (adapted) with permission from reference.[100] Copyright 2013 American Chemical Society.

The proposed metal-porphyrin structure may explain the difference in ORR activity and can be supported by theoretical calculations[153-155] demonstrating the difference in binding energy of the metal-porphyrin site depending on the identity of the metal. Changes in the oxidation state

of metals incorporated in a metal-porphyrin structure have been known to alter the binding energy of the active site[156] thus altering the turnover rate of the catalytic reaction.[157] This same concept can be applied to changing the identity of the metal bound to the nitrogen active site of NCNC as one possible explanation for the difference in half-wave potential between NCNC synthesized from different metals. A detailed ORR mechanism could be investigated through RRDE results by calculating the transferred electron number (*n*) per oxygen molecule, using equation 7:

Equation 7

$$n = \frac{4I_D}{I_D + \frac{I_R}{N}}$$

where I_D is the faradaic disk current, I_R is the faradaic ring current, and N=0.37 is the collection efficiency. An *n* value of 4 corresponds to a complete four-electron reduction process from O_2 directly to H_2O (eq. 4) while an *n* value of 2 implies the less efficient two-electron reduction process from O_2 to H_2O_2 (eq. 5).

Table 2-1 NCNC[M] catalytic activity towards the oxygen reduction reaction (ORR)

Material	*n*	Half-wave potential (V)
NCNC[Fe]	2.6 ± 0.1	–0.297 ± 0.006
NCNC[Ni]	3.9 ± 0.1	–0.334 ± 0.003
NCNC[Co]	3.1 ± 0.2	–0.316 ± 0.008

As shown in Table 2–1, NCNC[Ni] has a high *n* value of 3.9 ± 0.1 representing an almost exclusive four-electron process where little H_2O_2 is detected. This value is also significantly higher than the *n* values reported for nickel phthalocyanine-based electrocatalysts in the literature.[152, 158] There is a small contribution of the overall current related to two-electron reduction which could be attributed to different catalytic active sites on the nanotube surface. While the majority of active sites reduce oxygen through a four-electron process, a fraction of the catalytic sites reduce oxygen

through a two-electron process. NCNC[Fe] and NCNC[Co] both exhibit a mixed process of four-electron and two-electron processes with NCNC[Fe] having the largest component of two-electron reduction. On the bases of these results we can hypothesize that the different ORR mechanisms are strongly correlated with different metal catalysts and the resulting metal-nitrogen-carbon hybrid active sites.

To gain further insight into the selectivity of the metal-doped carbon system toward the compete or incomplete ORR, we examined the binding energies of the intermediates of both ORR processes namely, OH, OOH, and O for the complete four-electron reaction and OOH and H_2O_2 for the incomplete two-step two-electron process. For the complete four-electron reaction the peroxide intermediate stays bound to the catalyst surface and undergoes further reduction, while in the incomplete two-step two-electron reaction hydrogen peroxide is formed and desorbs from the catalyst surface.[119] Our analysis which is based on the thermodynamics of the intermediate steps without regard to the kinetics imposed has been shown before to describe well the ORR mechanism on metal surfaces.[159] Figure 2–4 shows the nitrogen and metal doped graphene model, and the optimum adsorption configuration for hydrogen peroxide. The adsorption distances for OH, OOH, O, and H_2O_2 are reported in Table 2–2 and the binding energies are reported in Table 2–3.

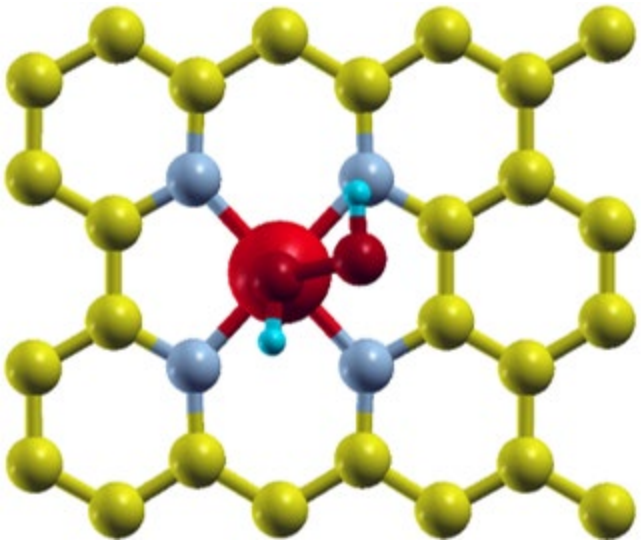

Figure 2-4 Ball and stick model that was used for quantum chemical calculations. Reprinted (adapted) with permission from reference.[100] Copyright 2013 American Chemical Society.

Table 2-2 DFT calculated adsorption distances for NCNC[M] towards intermediates of the ORR

Metal	OH	OOH	O	H_2O_2
NCNC[Fe]	1.80 Å	1.77 Å	1.64 Å	2.21 Å
NCNC[Ni]	2.00 Å	2.16 Å	1.43 Å	3.24 Å
NCNC[Co]	1.85 Å	1.87 Å	1.36 Å	2.25 Å

Table 2-3 DFT calculated binding energy for NCNC[M] towards intermediates of the ORR

Metal	OH	OOH	O	H_2O_2
NCNC[Fe]	2.78 eV	5.41 eV	3.67 eV	2.93 eV
NCNC[Ni]	4.16 eV	6.65 eV	5.02 eV	3.14 eV
NCNC[Co]	3.33 eV	5.93 eV	3.08 eV	3.15 eV

The adsorption energies are computed using H_2 and H_2O as a reference. Also, to avoid problems associated with the ground state energy of the O_2, the total O_2 energy is computed from the reaction ½ O_2 + H_2 → H_2O using the experimental dissociation energy 2.46 eV per H_2O and the total DFT energies of H_2O and H_2, both of which are described well in the DFT.[159] As the adsorption energy decreases, the catalyst surface increases in reactivity leading to stronger

adsorption of the intermediates. The trends in the adsorption energies show that the reactivity of different metals is in the order Fe > Co > Ni. These results show that there is a direct correlation between an increase in the occupation of the d-orbitals and a decrease in the strength with which the different intermediates are bound to the metal surface agreeing with previous investigations.[160]

The adsorption distance for H_2O_2 shows that the formation of hydrogen peroxide on NCNC[M] is the most favorable for NCNC[Fe] and NCNC[Co], as both have similar adsorption distances. On the other hand, on NCNC[Ni], the adsorption distance of H_2O_2 is larger than that of NCNC[Fe] and NCNC[Co] by about 1 Å. This is not the case with OOH as all metals can bind OOH, although the trends in the binding energies and distances between the different metals are similar to those of H_2O_2. For example, NCNC[Fe] and NCNC[Co] have an adsorption distance for OOH of 1.77 Å and 1.87 Å, respectively, and an adsorption distance for H_2O_2 of 2.21 Å and 2.25 Å. On the other hand, NCNC[Ni] has an adsorption distance of 2.16 Å for OOH and 3.24 Å for H_2O_2, a difference exceeding 1 Å. These computational results indicate that the H_2O_2 formation on NCNC[Ni] is hindered, which in turn explains the selectivity of NCNC[Ni] toward the complete ORR that is seen experimentally. Furthermore, NCNC[Fe] has the shortest adsorption distance for H_2O_2 as well as the smallest adsorption energy for H_2O_2 indicating that NCNC[Fe] is the most reactive material towards hydrogen peroxide.

To confirm the computation results, 1 mM aliquots of hydrogen peroxide, up to 10 mM total, were added to the materials, and the resulting current was measured as shown in Figure 2–5. All materials show an increase in relative current upon the addition of hydrogen peroxide. The response times of each material correlate to the binding energies determined in the computational studies. NCNC[Ni] has the longest response time which agrees with the weaker adsorption energy

of H_2O_2, thus lower reactivity, as determined by computational studies while NCNC[Fe] had the shortest response time correlating with the strong adsorption energy of hydrogen peroxide.

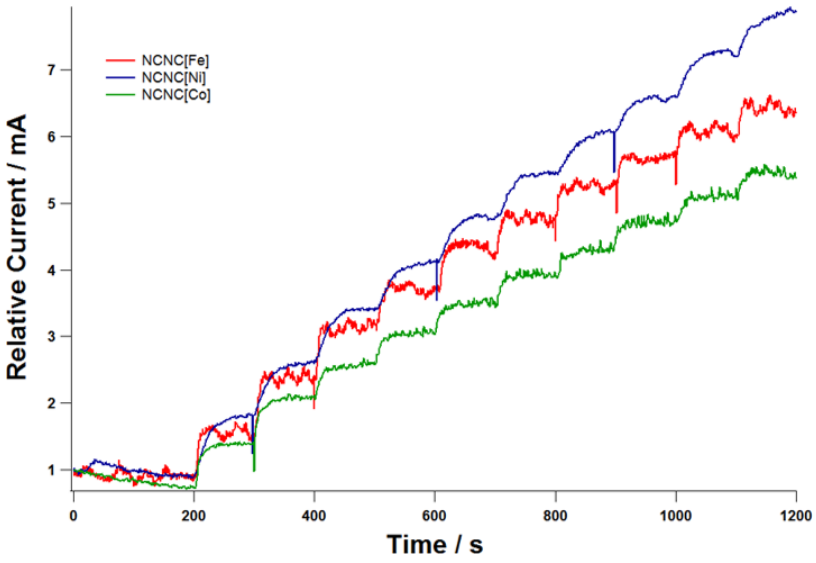

Figure 2-5 Relative current responses to 1 mM aliquots of hydrogen peroxide of NCNC[Fe] (red), NCNC[Ni] (blue), and NCNC[Co] (green). Reprinted (adapted) with permission from reference.[100] Copyright 2013 American Chemical Society.

In summary, NCNC with stacked-cup structure were synthesized successfully from ferrocene, nickelocene, and cobaltocene catalysts using CVD synthesis. The resulting materials were characterized by their electrocatalytic capacity for ORR with computational results supporting their relative activity. We believe that the active site in this material is analogous to a metal-nitrogen-carbon structure where the identity of the metal determines the mechanism that occurs on each material. NCNC[Fe] had the largest percentage of 2 electron reduction which is due to its short adsorption distance for hydrogen peroxide and small adsorption energy for hydrogen peroxide. While the results of this study have implications for electrocatalyst design we

hypothesize that they also indicate general reactivity towards H_2O_2 and could potentially be used to predict biological response to hydrogen peroxide.

The first separation technique explored on the NCNC[Fe] material was achieved by bath sonication of NCNC in a concentrated (32 wt%) KCl solution. After sonication for 150 hours, the resulting suspension of separated NCNC had an average length of around 180 nm, and about 90% of the NCNC were within the range of 0–300 nm as shown in Figure 2–6. Previously reported probe-tip sonication method was only able to achieve an average length of 380 nm with 70% of NCNC under 400 nm in length.[51] This result indicates that we can achieve improved separation of NCNC by simple KCl sonication treatment. Compared to other methods, this process requires neither harsh chemicals (oxidation or acidic reagents) nor intensive physical (probe-tip sonication) treatments, thus maintaining the inherent chemical functionalities while not damaging the surface of NCNC. The bath sonication was carried out twice under the same conditions, and similar separation results were achieved, indicating the reliability of the sonication technique. It should also be noted that the resulting separated NCNC form a stable colloidal suspension and remain in solution much longer than stacked NCNC, due to the shorter average length of the separated NCNC.

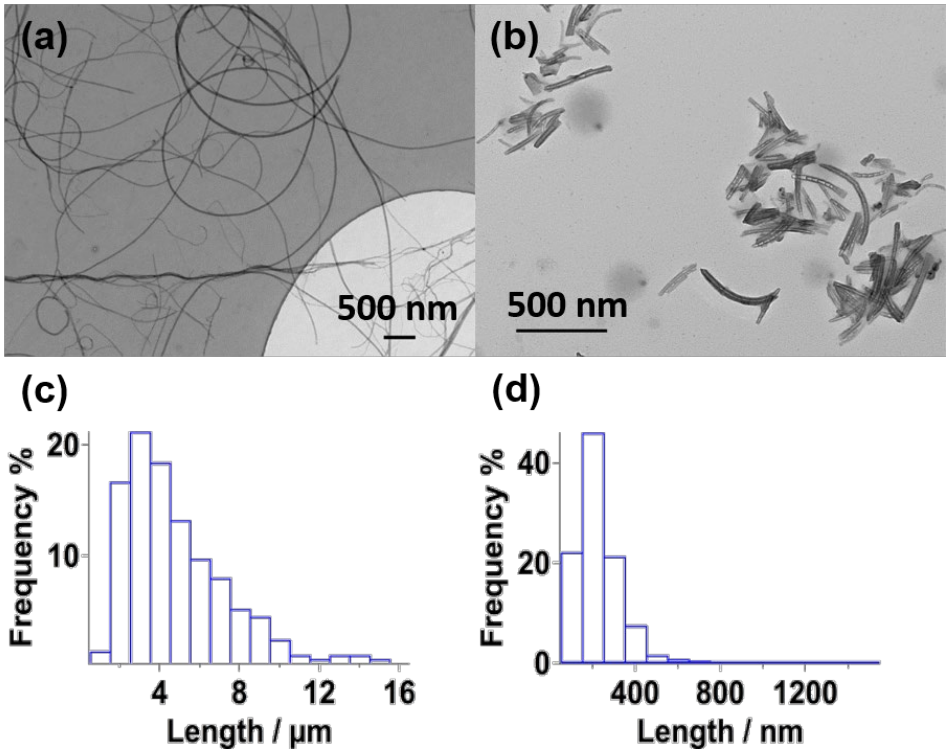

Figure 2-6 Transmission electron microscopy images of (a) as-synthesized NCNC and (b) separated NCNC. Length histogram of (c) as-synthesized NCNC and (d) separated NCNC. Reprinted (adapted) from reference.[101]

Further characterization showed that this KCl sonication method not only separated stacked NCNC, but also largely preserved their original surface structure. XPS shows that the nitrogen concentration relative to carbon was preserved around 1.5 atomic % in this separation process as shown in Figure 2–7. While an increase in oxygen content is observed in the XPS survey spectra, this is most likely due to residual SiO_2 derived from shed glass particles during the long sonication procedure. The survey spectra support this as an increase in the Si2p peak coincides with the increase in the O1s peak. Maintaining surface functionalities could be expected since KCl, which is not an oxidizing reagent, was used and the bath sonication applies an estimated power density of 42 W/L, which is much lower than the power density of probe-tip sonication of 720 W/L. Additionally, the high resolution N1s XPS spectra show that the types of nitrogen functionalities

do not change after the separation with KCl sonication. Before and after KCl sonication, pyridinic, pyrollic, graphitic, valley, and oxidized nitrogen species can be identified from the overall N1s spectrum. This indicates that the KCl sonication does not separate the cups through breaking the bonds of NCNC, thus keeping the surface intact, and instead only works to disrupt the weak van der Waals forces holding consecutive cups together. Conversely, the probe-tip sonication method attacks the bonds of NCNC, as well as the van der Waals forces, as can be seen by the breakdown of the intrinsic nitrogen functionalities into dangling nitrogen bonds and amine groups as previously reported.[51]

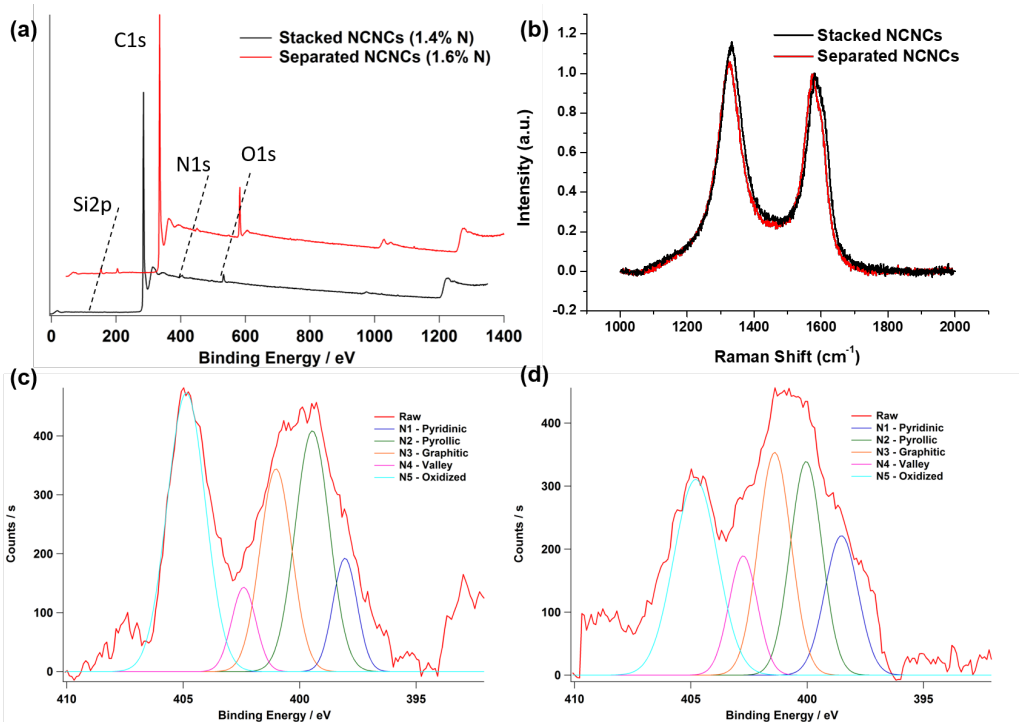

Figure 2-7 (a) Survey X-ray photoelectron spectroscopy (XPS) of stacked NCNC (black) and separated NCNC (red). (b) Raman spectra of stacked and separated NCNC. High resolution N1s XPS of (c) stacked NCNC and (d) separated NCNC with functionalities identified in the legend. Reprinted (adapted) from reference.[101]

Consequently, Raman results showed that the D/G ratio slightly decreased from 1.16 of stacked NCNC to 1.07 of separated NCNC, compared to the probe-tip sonication method where the D/G ratio increases with increasing process time up to a maximum of 1.5.[51] Such a small decrease in the D/G ratio might be related to the removal of extra amorphous carbon or other highly defective structures during the separation process, while leaving the majority of the NCNC surface unaffected. These Raman results show preference for the KCl sonication process towards disrupting the interlayer π-π interaction of adjacent cups or amorphous carbon structure rather than breaking the chemical bonds (C–C, C–N, or C–O) on the graphitic surface of NCNC.

In order to investigate the mechanism of the KCl separation, we compared the separation process to KOH (50 wt%) and pure DI water in order to determine the importance of potassium ions towards the separation of stacked NCNC as shown in Figure 2–8. The treatment of KOH was stopped after 26 hours due to the strong corrosive effects of KOH towards the glassware. However, even with shortened sonication time KOH was able to yield average NCNC segments around 212 nm, which is comparable to the separation achieved by KCl. On the other hand, sonication in DI water proved less effective for separation of NCNC achieving an average length of only 695 nm. This indicates that the sonication power itself is not enough to separate the NCNC effectively and instead K^+ ions are necessary to facilitate separation. Furthermore, due to the maintained chemical and surface structure as determined by XPS and Raman spectroscopy, it is proposed that K^+ intercalation occurs, thus weakening the van der Waals forces between adjacent cups inducing separation.

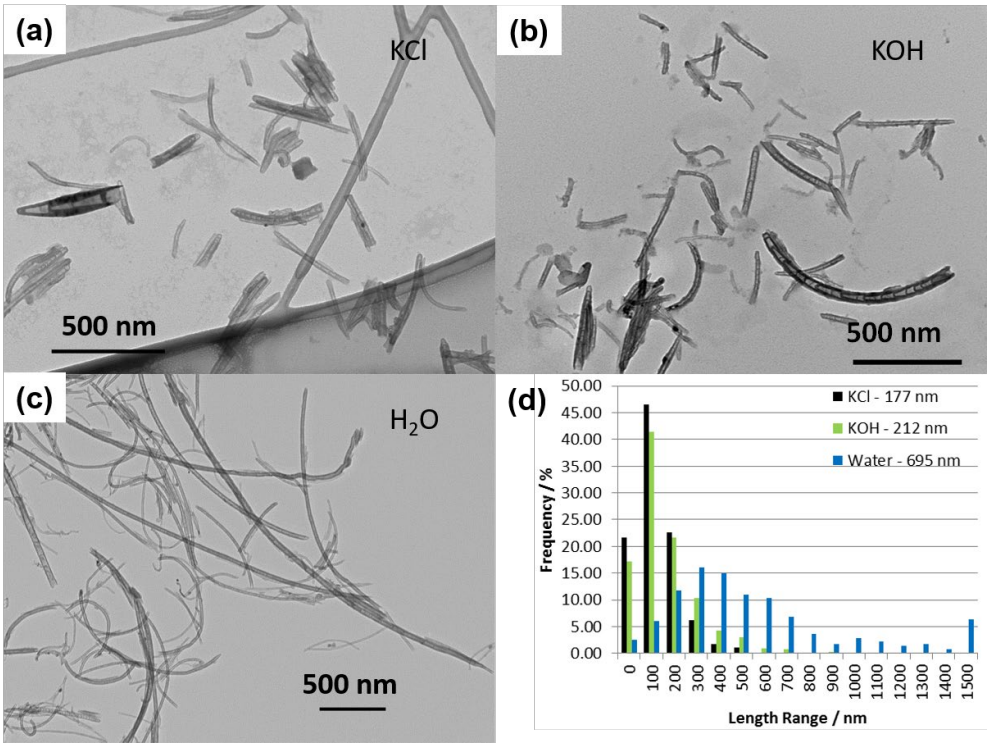

Figure 2-8 Representative transmission electron microscopy images of NCNC treated with (a) 32 wt% KCl for 150 hours, (b) 50 wt% KOH solution for 26 hours, and (c) DI water for 100 hours. (d) Length histogram of treated NCNC with average length (inset) of the three different separated NCNC samples. Reprinted (adapted) from reference.[101]

Potassium has been previously shown to form intercalation material such as C_8K with graphite.[129, 161, 162] Furthermore, potassium intercalation has been shown to occur in graphite during high-energy probe tip sonication.[126] Typical intercalation processes, such as two-zone vapor transport method, usually are performed at high temperatures and inert atmosphere. In our case with potassium ions, compounds like C_8K are not expected to form in aqueous solution, and no potassium signal was detected in the survey XPS. This is further shown by the lack of any peaks in the high-resolution K2p XPS spectra as shown in Chapter 6 supporting information. Exposure to sound waves creates a unique, high energy event known as acoustic cavitation where microbubbles within a solvent rapidly expand and collapse to create isolated areas with extreme

temperatures and pressure.[163] These high energy microbubbles when compressed would be able to penetrate the graphitic interspace and upon rapid expansion would allow the entry of potassium ions into the graphitic interspace. The resulting cation-π intercalation causes an increase of the intergraphitic distance and subsequent weakening of the interlayer π-π interaction, which leads to the dissociation of adjacent cups. NaCl and LiCl were also explored as salts for the separation of NCNC however their effects were negligible compared to the separation in potassium salt solutions.[101] KCl separation method was found to be effective for isolating individual NCNC while maintaining their inherent chemical functionalities. This technique will be compared to the probe-tip sonication of NCNC in order to determine which is most desirable for drug delivery applications.

For probe tip separation of NCNC, ferrocene based NCNC were first oxidized by bath sonication in a mixture of H_2SO_4/HNO_3 (3:1 v/v) for 4 hours. Oxidized NCNC were then separated by high-intensity probe-tip sonication to yield separated NCNC consisting of many short-stacked and individual nanocups, which were then unzipped by $H_2SO_4/KMnO_4$ treatment, forming nitrogen-doped GNS. The unzipping mechanism starts from the addition of manganese ester to C=C bonds on exposed graphitic planes and propagates along the adjacent alkene groups on the same plane.[130, 164] After the oxidation process, oxidized NCNC largely maintain the morphology of stacked cup-shaped compartments of the initial material with diameters of 30 – 50 nm however with much shorter lengths of 1–2 μm as shown in Figure 2–9. After the ultrasonic separation, most of the NCNC segments were shortened to about 200 nm, consisting of either individual nanocups or several stacked-cup segments. After treatment with $H_2SO_4/KMnO_4$, the cup-shaped structures were completely unzipped and transformed into flakelike GNS. The sizes of the nanosheets appear

to be correlated to the initial length of the separated NCNC, which ranges from apparent 5–10 nm graphene quantum dots to larger flakes hundreds of nanometers in size.

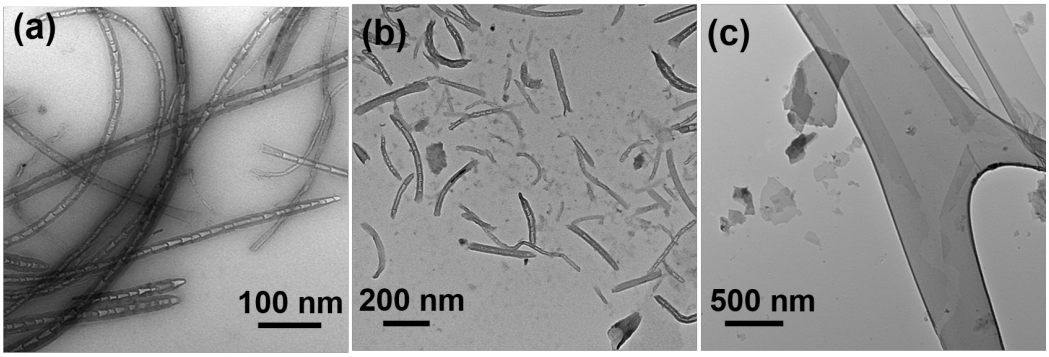

Figure 2-9 Transmission electron microscopy images of (a) oxidized NCNC, (b) separated NCNC, and (c) graphene nanosheets after unzipping of separated NCNC. Reprinted (adapted) with permission from reference.[102] Copyright 2015 American Chemical Society.

The chemical functionalities of the synthesized materials were determined by XPS as shown in Figure 2–10. The high-resolution N1s scans show changes of the nitrogen functionalities as a result of tip separation. The spectrum of oxidized NCNC can be deconvoluted into four peaks at 398.7 eV (N1), 399.8-400.3 eV (N2), 401-401.6 eV (N3), and 405 eV (N5), which can be assigned to pyridinic, pyrollic/amine, graphitic, and oxidized nitrogen species respectively.[165] Separated NCNC are primarily composed of graphitic and pyrollic/amine nitrogen functionalities which is different than the separation of NCNC through sonication in alkali salt solutions. XPS of GNS shows that the nitrogen exists primarily as pyrollic/amine nitrogen, which is a direct result of the unzipping process where nitrogen previously contained within the graphitic lattice of the NCNC is converted to edge nitrogen functionalities.[140] Because the existence of nitrogen alters the local electronic structure and makes the peripheral carbon networks more vulnerable to MnO_4^- oxidation,[131] we infer that the unzipping of separated NCNC is preferentially induced by the

nitrogen defective edges. Due to the small initial size of separated NCNC and the increasing amount of defects created by probe-tip sonication,[51] the unzipping may take place from multiple nitrogen-functionalized defective sites on separated NCNC and propagate simultaneously, which more easily cuts the graphitic planes into many GNS fragments. This explains the distribution of sizes observed for the GNS flakes.

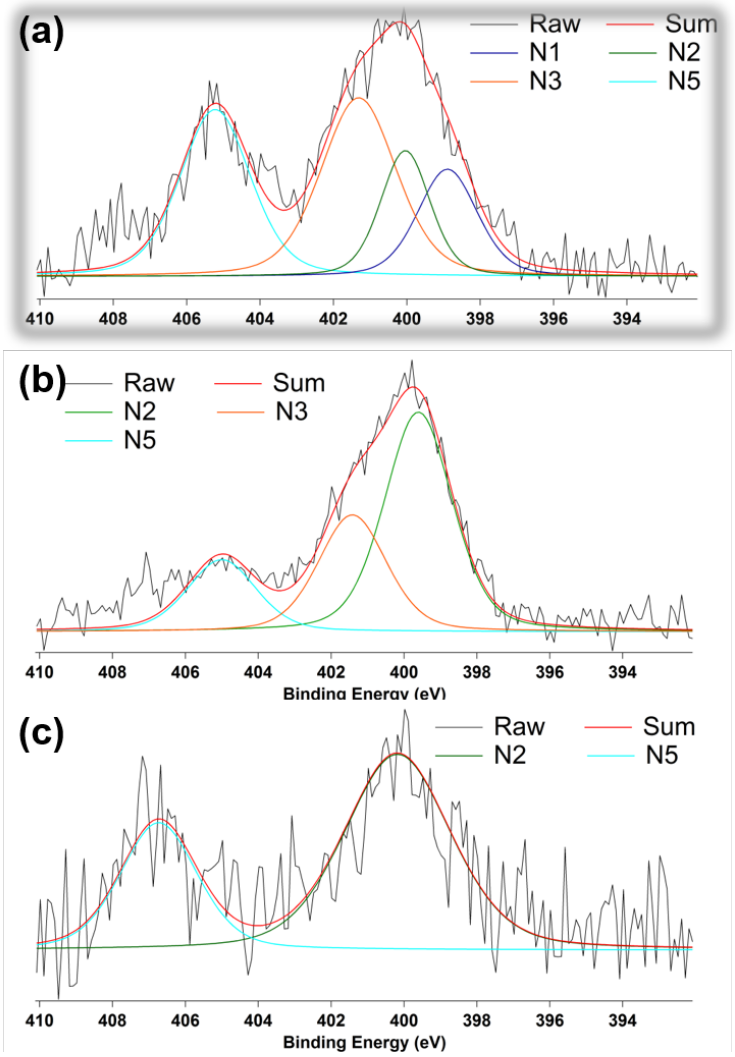

Figure 2-10 High resolution N1s X-ray photoelectron spectroscopy of (a) oxidized NCNC, (b) separated NCNC, and (c) graphene nanosheets. Reprinted (adapted) with permission from reference.[102] Copyright 2015 American Chemical Society.

The nitrogen-doped GNS may have interesting applications as SERS substrates. Facilitated by the rich nitrogen functionalities, the GNS can be evenly decorated with GNP through a trisodium citrate reduction of $HAuCl_4$. Figure 2–11 shows TEM imaging of GNS evenly functionalized with GNP with diameters of about 20 nm presumably anchored on the local nitrogen functionalities. Due to the heavy decoration of amine functionalities on GNS, these functional groups may be crucial for decoration of nitrogen-doped CNM with gold nanoparticles. The island distribution of GNP on graphene nanosheets causes SERS on the graphene substrate, which can be used for highly sensitive SERS detection of biomolecules. To illustrate this application, we incubated the GNP/GNSwith the Raman probe molecule R6G at low concentrations and drop-cast 20 μL from each sample on glass slides for Raman characterization. As shown in Figure 2–11, without the SERS substrate, pure R6G solution drop-cast on a glass slide incurred very weak Raman signals, even at high concentration of 10^{-2} M. However, significantly enhanced signals were observed in the presence of GNP/GNS at 10^{-4} M of R6G, which corresponds to enhancement of more than 100 times. The detection limit can be as low as 10^{-6} M under our current conditions; the signals at even lower concentrations tend to be overshadowed by those of the GNS. We speculate that the SERS signals arise from the optimal diameters and interparticle distances of GNP that provide coupled surface plasmon resonance (SPR) and significantly enhance the local electromagnetic field.[166] The enhanced SERS sensitivity, combined with suitable functionalization chemistry of the GNS/GNP composite, can lead to new classes of novel nanomaterials for drug delivery and *in vivo* SERS spectrum imaging.

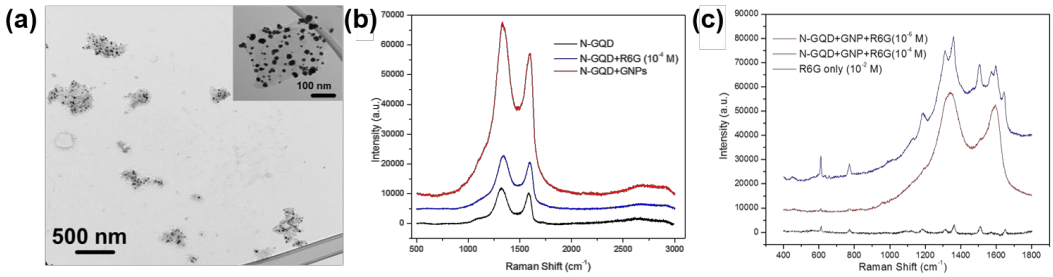

Figure 2-11 (a) Transmission electron microscopy (TEM) image of graphene nanosheets (GNS) after functionalization with gold nanoparticles (GNP), the inset shows a magnified TEM image of the material. (b) Raman spectrum of GNS (black), as compared to the surface enhanced Raman spectrum of GNS functionalized with GNP (red), and Raman spectrum of GNS mixed with 10^{-4} M Rhodamine 6G without GNP functionalization. (c) Surface enhanced Raman of GNP-functionalized GNS sensing probe molecules of Rhodamine 6G. Reprinted (adapted) with permission from reference.[102] Copyright 2015 American Chemical Society.

2.4 Conclusions

In this chapter, stacked NCNC were manipulated through altering their synthetic conditions and performing post-synthesis chemical and physical modifications. We determined that NCNC synthesized from iron precursors have the strongest binding affinity towards hydrogen peroxide and may potentially be preferred for enzymatic degradation cycles involving hydrogen peroxide. Additionally, two separate techniques for NCNC separation were explored, mainly sonication in alkali salt solutions and oxidation and probe-tip sonication. Sonication in alkali salt solutions results in maintained nitrogen functionalities and shorter length distributions, however the process can take up to 150 hours to complete. By contrast, oxidation and probe-tip sonication result in longer length distributions and convert nitrogen functionalities predominantly to amine groups.

These amine groups can act as initiation sites for decoration with gold nanoparticles which results in a material with SERS applications.

2.5 Acknowledgement

This work is supported by NIEHS Award R01ES019304 and NSF CAREER Award No. 0954345. YT and YZ acknowledge a graduate student fellowship through Bayer MaterialScience. WAS is grateful for computing time provided by the Extreme Science and Engineering Discovery Environment (XSEDE), which is supported by National Science Foundation Grant No. OCI-1053575. Special thanks to the Department of Biological Sciences, the Department of Materials Science and Engineering, and the Nanoscale Fabrication and Characterization Facility at the University of Pittsburgh for provision of access to instruments.

3.0 Decoration of NCNC with GNP

3.1 Introduction

In Chapter 2 we explored various ways to manipulate NCNC for their potential applications towards drug delivery. We also determined that amine nitrogen functionalities are able to act as nucleation sites for the formation of GNP and may therefore represent an attractive way to modify NCNC further to produce capsules for drug delivery. In this Chapter we will investigate decoration of separated NCNC with GNP in an attempt to create GNP corks resulting in a sealed container which can be effectively loaded with cargo. Once the NCNC are loaded and corked, they will be exposed to enzymatic oxidation environments for effective uncorking and delivery of the loaded cargo. First, the separation conditions for NCNC will be optimized to produce the best material for GNP corking. Second, the trisodium citrate reduction of $HAuCl_4$ in the presence of separated NCNC will be explored in order to generate GNP corked NCNC. Third, the NCNC will be effectively loaded with molecular cargo and the loading confirmed through the use of Raman enhancement of the cargo through the GNP cork. Finally, the loaded and corked NCNC will be exposed to enzymatic oxidation conditions in order to remove the GNP cork and release the loaded cargo.

The material contained within this chapter is comprised of two separate publications. Our *Journal of American Chemistry* publication reports our first decoration of separated NCNC with GNP through trisodium citrate reduction of $HAuCl_4$. The second publication is a step by step protocol paper published in *Current Protocols in Chemical Biology*. The initial reporting does not represent the optimized separation and corking conditions which will be explored in this chapter.

The final optimized separation and corking conditions are reported in our *Nanoscale* publication which will be discussed in detail in Chapter 4. The results presented in this Chapter represent the evolution of the separation and corking conditions between the initial *Journal of American Chemistry* publication and the optimized *Nanoscale* publication.

The material contained in this chapter was published in two research articles and have been reprinted (adapted) with permission from the respective publisher.

1. Nano-Gold Corking and Enzymatic Uncorking of Carbon Nanotube Cups. *Journal of the American Chemical Society* **2015**, *137*(2), 675–684, Copyright © 2015, American Chemical Society. The full citation is listed as reference[167] in the bibliography section.

List of Authors: Yong Zhao, Seth C. Burkert, Yifan Tang, Dan C. Sorescu, Alexandr A. Kapralov, Galina V. Shurin, Michael R. Shurin, Valerian E. Kagan, Alexander Star

Author Contributions: All authors contributed to the design of experiments and writing of the paper. YZ and SCB carried out corking and loading experiments. YZ, YT, and SCB performed material characterization. DCS led the theoretical study. AK and VEK performed cellular studies. GVS and MRS performed *in vitro* experiments.

2. Corking Nitrogen-Doped Carbon Nanotube Cups with Gold Nanoparticles for Biodegradable Drug Delivery Applications. *Current Protocols in Chemical Biology* **2015**, *7*(4), 249–262, Copyright © 2015, John Wiley & Sons, Inc. The full citation is listed as reference[168] in the bibliography section.

List of Authors: Seth C. Burkert, Alexander Star

Author Contributions: All authors contributed to the design of experiments and writing of the paper.

Advancements in drug delivery have been made through the implementation of newly developed nanomaterials including, drug-polymer conjugates, polymeric nanoparticles, solid lipid nanoparticles, dendrimers, liposomes, micelles, GNPs, and CNM.[169] While these nanomaterials have been tested as drug delivery devices, several issues remain, including nonspecific delivery of therapeutic cargo, inflammation due to accumulation of drug delivery devices, and short circulation time. Unique properties of CNM that make them ideal candidates for drug delivery include large surface area, the ability to encapsulate designated cargo, and the ability to functionalize nanomaterials with biocompatibility agents that help deliver cargo to specific target sites. Although CNT have been viewed as an attractive material for drug-delivery devices, they have been shown to cause oxidative stress both *in vitro* and *in vivo* resulting in inflammation and cell damage in the lungs and liver. Pristine CNT directly induce the formation of reactive oxygen species resulting in oxidative damage ultimately leading to cell damage and apoptosis.[170] Similar to asbestos, DNA damage and inflammation are caused by CNT with a high aspect ratio, whereas short MWNT with lengths less than 200 nm have negligible side effects *in vivo*.[171] Functionalization of pristine CNT, primarily with polyethylene glycol, improves solubility in aqueous solution, thereby increasing circulation time and diminishing the harmful side effects caused by the formation of reactive oxygen species. Moreover, nitrogen functional groups facilitate the degradation of CNT by the body resulting in less cytotoxic behavior.[172]

Separated NCNC are characterized by an abundance of nitrogen functional groups on the opening of individual cups[173] and provide an attachment site for GNP which can effectively cork NCNC. As shown in Chapter 2, the intense energy output of probe-tip sonication alters inherent nitrogen functionalities into dangling amine groups which can coordinate with gold clusters. Therefore, GNP can be chemically grown, through trisodium citrate reduction of chloroauric acid,

into a solid particle which can effectively seal the open end of NCNC. This synthesis of GNP is referred to as the Turkevich method and is a common method for producing free standing GNP with confined size distributions.[174] The mechanism for GNP growth has been extensively investigated with several factors including pH, temperature, ionic strength, and precursor concentrations playing critical roles in the resulting quality and size distribution of synthesized particles.[60] Graphitic structures have also been shown to reduce $HAuCl_4$ through their inherent functionalities resulting in gold nanostructure formation.[64-66] Therefore, the conditions for the most efficient GNP corking of separated NCNC needs to be explored.

Effective drug delivery using GNP-corked NCNC requires a mechanism for cork detachment and release of cargo. CNM can be biologically degraded *in vitro* and *in vivo* by peroxidases, such as HRP, MPO, and EPO.[74] In the presence of peroxidases, CNT with oxygen functionalities degrade more rapidly than pristine CNT.[50] Improved degradation of oxidized CNT results both from their improved solubility in aqueous solution and from the electrostatic interactions of carboxyl groups that orient CNT close to the heme active site of the enzyme. Present in neutrophils, the most abundant white blood cells in the body and key players in normal inflammatory responses, MPO can oxidize halogens at high rates, producing hypohalous acids that further improve CNT degradation. Due to its exceptional ability to degrade oxidized CNT and its biologically availability and practical relevance, MPO will be used to degrade separated NCNC and effectively remove the GNP cork.

Given their nanoscale dimensions and versatile reactivities, CNT have received increasing research attention for drug delivery.[175-177] Drugs loaded on the outer surface of CNT *via* covalent[177] or noncovalent[178] functionalization risk unnecessary exposure causing side-effects or early drug degradation.[179] Comparatively, filling drugs into the hollow interior of nanotubes is more desirable

in terms of protecting drugs from reaction before reaching the designated target.[180-182] NCNC provide a unique system for drug delivery as their morphology allows easy access to both the inner cavity and the outer surface for diverse functionalization. To illustrate the potential of GNP corked NCNC as drug delivery systems, loading with a common fluorescent dye, Rhodamine 123 (Rh123), was performed. By using Raman spectroscopy, we were able to prove the loading of the desired cargo inside GNP corked NCNC. The fluorescent properties of Rh123 also provides a route to track the enzymatic uncorking of NCNC and resulting release of cargo.

3.2 Experimental section

3.2.1 Corking NCNC with GNP

NCNC were synthesized from ferrocene as reported in Chapter 2. 250 μL of $HAuCl_4$ aqueous solution (1 mg/mL) was added into 5 mL of ~0.01 mg/mL separated NCNC aqueous solution when stirring on a hot plate at 70°C. After 20 minutes of incubation, 150 μL of 1 wt% trisodium citrate solution was added dropwise, and the reaction was stirred for another 2 hours. GNP/NCNC conjugates were precipitated from free GNP by centrifugation at 3400 rpm for 15 minutes. For effective loading of corked NCNC the desired cargo was also added to the solution during corking. This is the base synthesis for producing corked NCNC. Alterations to this corking procedure will be discussed in the results and discussion as they are made.

3.2.2 Materials characterization

TEM was performed with a FEI Morgagni microscope at an accelerating voltage of 80 kV. Environmental TEM images were taken with a Hitachi H-9500 TEM. Raman spectra were taken on a Reinshaw inVia Raman microscope with an excitation wavelength of 633 nm at 50% laser intensity and 10 second exposure time, unless noted otherwise. XPS was performed on a Thermo Scientific Kα using monochromated Al Kα X-rays as the source. UV-Vis spectroscopy was carried out on a PerkinElmer Lambda 900 spectrometer. Fluorescence spectra were taken on a HORIBA Jobin Yvon Fluoromax-3 spectrofluorometer with a slit width of 2 nm, excitation of 500 nm and an emission of 520 nm.

3.2.3 Opening and degradation of gold-corked NCNC (Au-NCNC)

GNP corked NCNC were dispersed at a concentration of 0.015 mg/mL into 0.01 M phosphate buffer solution in a total volume of 1000 μL. The enzymatic degradation was conducted following published procedure.[6] To the NCNC sample, NaCl at a concentration of 1 μM is added on the initial day; lyophilized purified native human MPO (Athens Research and Technology, Inc.) is added daily at a concentration of 8.35 μg/mL; 1 μL of 100 mM H_2O_2 is added every 2 hours, four times per day. All samples were incubated at 37°C for 20 days, with daily agitation by vortex shaker for better dispersion.

3.2.4 Computational methods

Plane-wave DFT calculations using density functional theory and 3D supercell models were performed using Vienna *ab initio* simulation package (VASP) code.[183, 184] The electron-ion interaction was described by the projector augmented wave (PAW) method of Blöchl[185] and the Perdew, Burke and Ernzerhof (PBE)[142] functional has been used for description of the exchange and correlation. The PBE functional was corrected to include long-range dispersion interactions using the Tkatchenko and Scheffler method[143] as implemented in the VASP code.[186] Calculations were spin-polarized and used a cutoff energy of 400 eV. The graphene flake surface with a zigzag termination running along the Ox axis has been represented using a supercell with Nx=7 and Ny=11 periodic units separating the opposite edges of the graphene flake. These edges were terminated with H atoms or with other functional groups as described below.[167] In order to reduce the lateral interactions for the adsorbed Au_{20} clusters on graphene surface, the graphene sheet was separated by vacuum layers up to 13.6 Å and 20.4 Å along the Oy and Oz directions, respectively. Given the large dimensions of the supercells used, the sampling of the Brillouin zone was done only at the Γ point. The adsorption energy of the Au_{20} cluster on graphene surface was calculated based on the equation $E_{ads} = (E_{(A)} + E_{(S)} - E_{(A+S)})$ where $E_{(A)}$ is the energy of the isolated Au_{20} cluster, $E_{(S)}$ is the total energy of the graphene surface and $E_{(A+S)}$ is the energy of the combined adsorbate-surface system in the optimized configuration. In the sign convention introduced above, positive adsorption energies correspond to stable adsorption configurations. The minimum energy reaction pathways for diffusion of the Au_{20} cluster on graphene surface was calculated using the climbing-image nudged elastic band (CI-NEB) method.[187]

3.3 Results and discussion

In Chapter 2 we demonstrated two unique separation techniques for NCNC; one based on salt sonication preserving the inherent functionalities of NCNC and one based on probe-tip sonication converting nitrogen functionalities to amine groups. Based upon the decoration of GNS, primarily composed of amine groups, with GNP we assume that amine groups are the anchoring site for such chemical functionalization. In order to confirm this observation, DFT calculations were performed in order to determine the binding energy of gold clusters with the various functionalities on separated NCNC. The resulting binding energies will be used in order to determine the optimum separation technique for the most efficient corking of separated NCNC. The nitrogen functionalities possible in NCNC are pyridinic, pyrollic, graphitic, amine, and oxidized nitrogen. We simulated the initial stage of GNP nucleation process for the case of an Au_{20} cluster adsorbed initially either at the center or at the edge of a 7 × 11 graphene flake functionalized with the possible nitrogen or oxygen functional groups as shown in Figure 3–1. By comparing the adsorption energy at the most stable binding configuration, we found that the graphene edge functionalized with an aliphatic primary amine ($-CH_2NH_2$) incurred the strongest binding with Au_{20}. In this case, the $-CH_2NH_2$ group is extruding out of the graphene plane such that the lone electron pair from N is unconjugated and forms a covalent bond with the Au_{20} cluster.

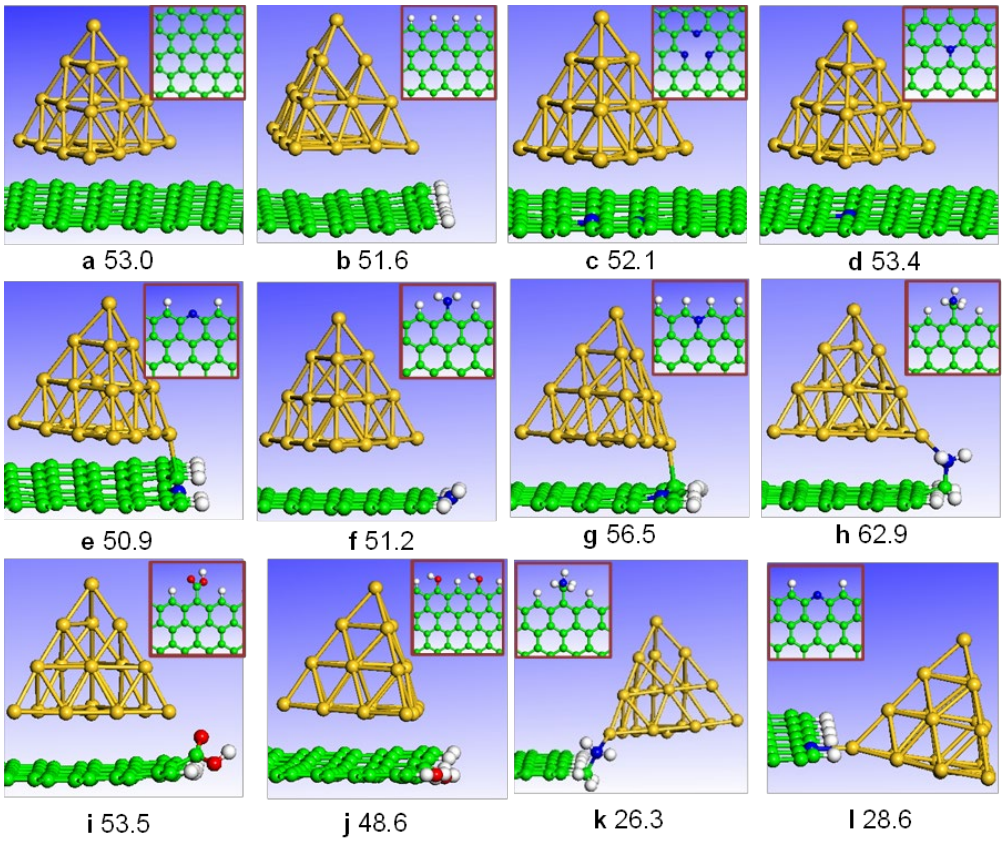

Figure 3-1 Pictoral views of the atomic configuration corresponding to adsorption of an Au_{20} cluster: (a) above a (7×11) graphene flake in the central region of the flake, (b) above the graphene flake near the hydrogen terminated zigzag graphene edge, (c) above a graphene defect functionalized with three pyridinc N atoms, (d) above a substitutional N (graphitic N) on the graphene surface, (e) above a pyridinic N on the graphene edge, (f) above an aromatic amine on the graphene edge, (g) above a graphitic N on the graphene edge, (h) above a CH_2NH_2 group on the graphene edge, (i) above a carboxylic acid on the graphene edge, (j) above a hydroxyl on the graphene edge, (k) attached to the amine group on the graphene edge, (l) attached to the pyridinic N on the graphene edge. Insets: the top view of the corresponding bare or functionalized graphene flake. For each configuration the corresponding adsorption energy (in kcal/mol) of the Au_{20} cluster is also provided. Legend of atoms: C (green), N (blue), O (red), and Au (orange). Reprinted (adapted) with permission from reference.[167] Copyright 2014 American Chemical Society.

Because individual NCNC have multi-walled structure with diameters of several tens of nanometers, their surface has relatively small curvatures and thus can locally be represented by flat graphene sheets. The Au_{20} cluster was placed either at the center or close to the edge of the flake and interactions with different functional groups were probed by evaluation of the corresponding adsorption energies (kcal/mol). Without nitrogen-doping, only the long-range dispersion interactions between the aromatic carbon rings and Au atoms are responsible for the adsorption. As a result, there is a slight drop in adsorption energy of Au_{20} from the center to the edge of the graphene sheet. However, when either pyridinic or graphitic nitrogen replaced the carbon atoms in the center, no remarkable difference in adsorption energy was observed. When Au_{20} was adsorbed at the edge of graphene, the adsorption energy varies depending on the edge functional groups. Compared with undoped graphene, the graphene edge functionalized with pyridinic N or aromatic amine does not seem to increase the adsorption energy. There is a small increase when Au_{20} is close to graphitic N on the edge when the apex atom of the Au cluster binds with a neighboring C of the graphitic N. However, when the graphene edge is functionalized with an aliphatic primary amine ($-CH_2NH_2$), a more significant increase in adsorption energy by over 10 kcal/mol is observed. In this case the $-CH_2NH_2$ group is extruding out of the graphene plane such that the electron pair from N is unconjugated and forms a covalent bond with Au_{20}.

As separated NCNC are also functionalized with oxygen groups so we investigated their binding energies towards Au_{20}. The oxygen functional groups do not appear to be strong anchoring sites for GNP binding. Specifically, the carboxylic groups that exist on the surface from the oxidation process show only a slight increase in the adsorption energy of Au_{20}, even though the oxygen atoms are located out of the graphene plane. Furthermore, the binding energy of the Au_{20} cluster decreases even further when adsorption takes place at a graphene edge functionalized with

hydroxyl groups. Besides the binding configuration of Au_{20} on the graphitic surface, nitrogen functional groups at the edge can also provide initial or intermediate binding states for the Au_{20} cluster. The side interaction of Au_{20} can be enhanced by amine and pyridinic N groups, with covalent bonds formed between an apex Au atom and N as compared to Au_{20} attaching to the edge of a bare graphene sheet terminated with hydrogen. Although this side interaction is much weaker than the on-surface interaction due to smaller contributions of Au-C dispersion interactions, the observed enhancement effect from the edge nitrogen groups can be cumulative in the case of the multi-layer graphitic edges at the open rims of NCNC.

The results of the theoretical calculations indicate that dangling amine bonds have the strongest adsorption for gold clusters and therefore represent the best functionality in order to decorate NCNC with GNP. Therefore, probe-tip sonication is the desired method of NCNC separation for best GNP decoration. In order to confirm the computational results, we performed a trisodium citrate reduction of $HAuCl_4$ in the presence of probe-tip sonicated NCNC as well as KCl separated NCNC as shown in Figure 3–2. As expected, GNP decoration of KCl separated NCNC shows some stacked segments being barren of any nanoparticle formation and a lack of specificity to the open end on cup segments which are decorated. On the other hand, probe-tip sonication shows more uniform GNP decoration with a majority of the nanoparticles being formed around the open end of the cup. Therefore, probe-tip sonication will be used in order to prepare separated NCNC for GNP corking reactions. Since the KCl separation technique was able to produce short NCNC segments with few changes in structural integrity, the probe-tip sonication procedure needs to be updated in order to also obtain short segments with few defects in the side walls.

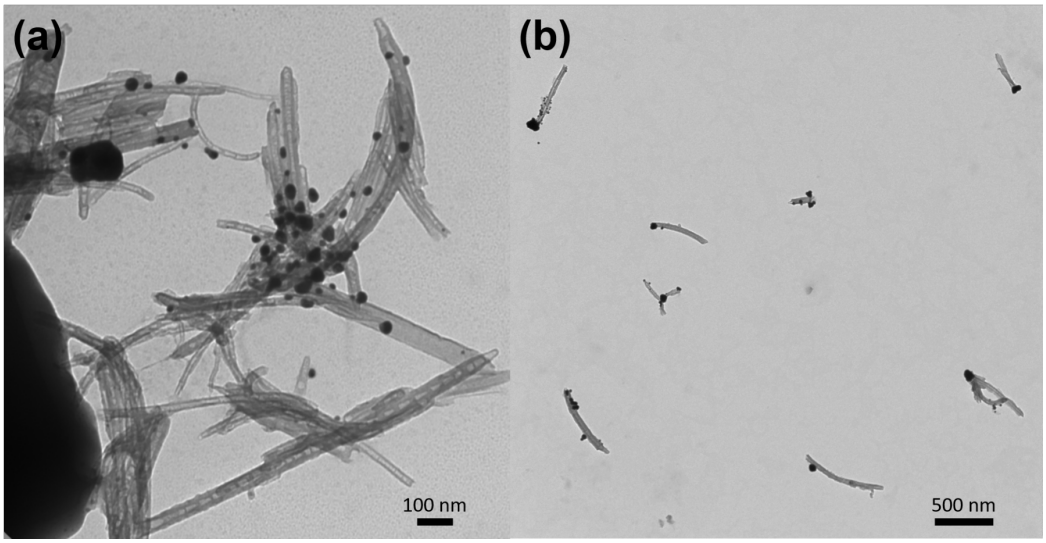

Figure 3-2 Transmission electron microscopy images of GNP decoration of (a) KCl separated NCNC, and (b) probe-tip separated NCNC.

As shown previously, prolonged probe-tip sonication time results in an increase in the overall D/G ratio of the separated NCNC and therefore process time should be shortened in order to improve structural integrity.[51] This alteration in structural integrity could result in poor drug delivery results as loaded cargo may be able to escape the sealed cavity. Oxidation conditions, while functionalizing the outer surface of CNT, have also been shown to shorten CNT length over time.[6, 188] The oxidation of stacked NCNC is used to produce hydrophilic carbon particles, but also serves to aid the isolation of individual NCNC from their neighboring cups. Therefore, by altering the separation procedure to include longer oxidation times and shorter probe-tip sonication times, ideal length distributions for *in vivo* applications can be achieved. The increased oxidation time will result in shorter NCNC prior to probe-tip sonication, and their increased oxygen functionalization should aid in the separation of stacked cups and improve their resulting colloidal stability.

Stacked NCNC first underwent extended oxidation times in order to decrease their initial length before probe-tip sonication. The initial procedure consists of a 4-hour oxidation in a 3:1 mixture of H_2SO_4/HNO_3. The resulting oxidized NCNC have lengths that are too long to be appropriately measured and therefore length distributions are not available for this time point. The oxidation time was increased to 6 and 8 hours to determine if shortening of the NCNC occurs. These results are summarized in Table 3–1. After a 6-hour oxidation the length of NCNC had shortened to 817 ± 305 nm, and after an 8-hour oxidation the length further decreased to 360 ± 190 nm. As sonication time increased up to 4 hours the average lengths of the material had an overall downward trend. Sonication times ranging from 1 to 4 hours have overlapping length distributions showing no benefit for increased sonication times for effective separation of NCNC, however the separation of adjoining cups is desirable to expose the hydrophobic inner core of the NCNC. The interior of NCNC are not oxidized as they are protected from the outer environment during the oxidation process. Therefore, the probe-tip sonication which separates cups further allows exposure of the hydrophobic core to the environment which can be used to attract cargo with poor aqueous solubility as a mechanism for loading. This will be explored later in this Chapter and in Chapter 4. The synthesis of separated NCNC does show some deviation in reproducibility as a duplicate separation had a length scale 100 nm larger than the initial separation.

Table 3-1 Length averages for separation techniques. Each average consists of at least 50 length measurements taken from TEM images

Sample	Length (nm)	Standard Deviation (nm)
6-hour oxidation	817	305
8-hour oxidation	360	190
1-hour sonication	321	153
2-hour sonication	269	153
3-hour sonication	291	146
4-hour sonication	269	134
Duplicate separation	372	234

We have shown that separated NCNC can be decorated with GNP through trisodium citrate reduction of $HAuCl_4$. While this method has been extensively investigated for free nanoparticle growth,[60, 174] conditions for the effective decoration of CNM have been less explored. Several reports have shown that CNM may have the inherent ability to reduce gold thus eliminating the need of an external reducing agent.[64-66] First, we will investigate whether inclusion of trisodium citrate in the GNP formation is beneficial to cork formation. Another factor which heavily influences the formation of GNP is the synthesis temperature.[174] The standard synthesis for GNP formation occurs at 100°C which would be too high for the potential loading of biological cargo, such as enzymes, which can denature at temperatures higher than 37°C.[189] Gold decoration reactions were run in the absence and presence of trisodium citrate at room temperature, 75°C, and 100°C to determine optimum GNP decoration. Representative TEM images are shown in Figure 3–3.

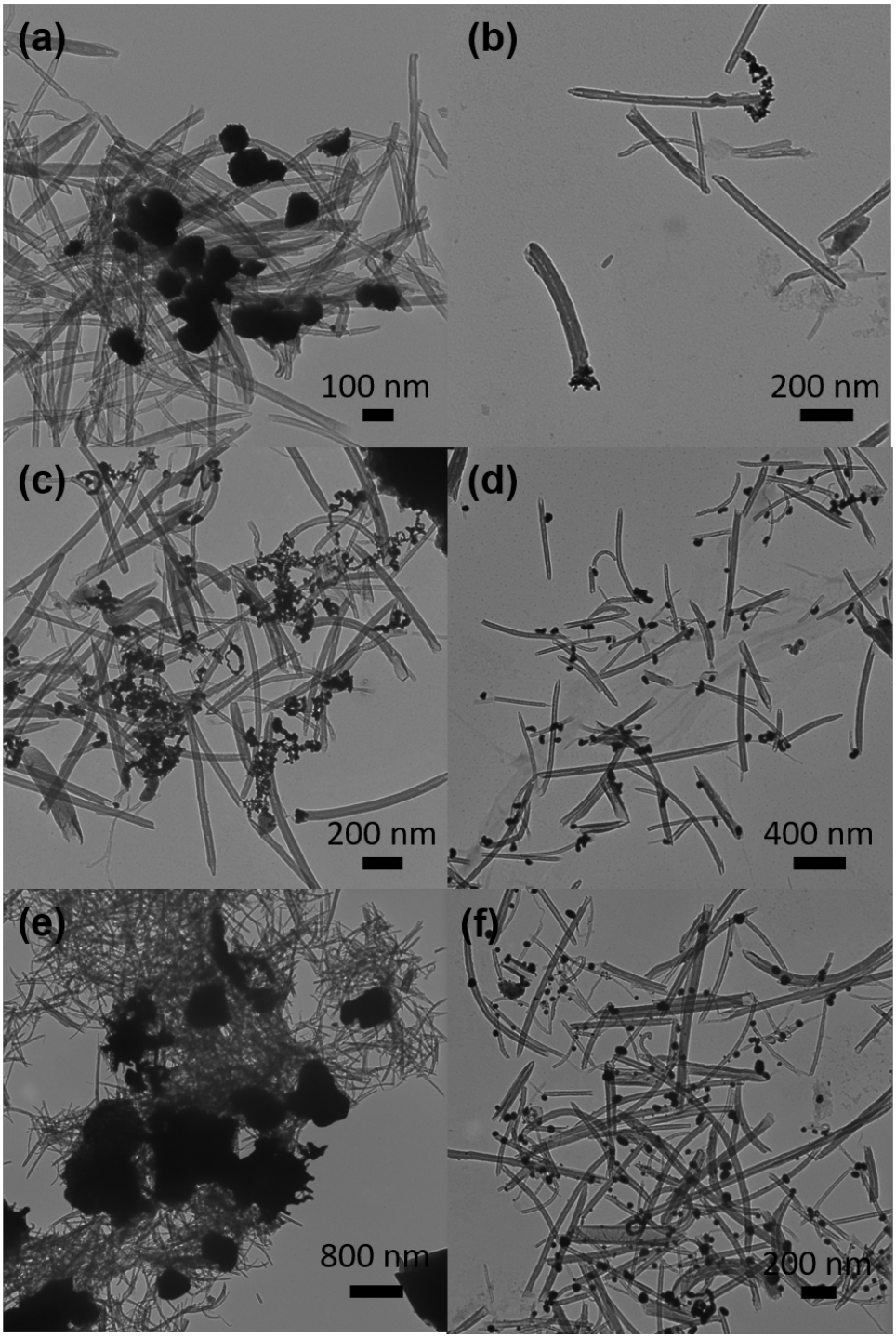

Figure 3-3 Representative transmission electron microscopy images of GNP corking reactions at (a) room temperature without trisodium citrate, (b) room temperature with trisodium citrate, (c) 75°C without trisodium citrate, (d) 75°C with trisodium citrate, (e) 100°C without trisodium citrate, and (f) 100°C with trisodium citrate.

In the absence of a reducing agent, gold structures are observed decorated on NCNC, although their size and morphology are temperature dependent. At room temperature, various structures are observed with dimensions around 100 nm. These structures range from agglomerates with no definitive shape or structure to prism-like structures. Due to the variation in particle formation at room temperature, non-citrate conditions do not appear to be ideal. At 75°C some makeshift "corking" is observed where aggregate particles are found to form at the opening of the NCNC. However, the dominant morphology of the gold structures comes in the form of long nanowires. At 100°C small particle formation is non-existent, and the gold structure appear as large aggregates with dimensions exceeding 1 μm. In the presence of trisodium citrate, more controlled nanoparticle formation is observed, and general trends based upon temperature can be observed. As the temperature of the reaction increases, more free gold nanoparticles are formed with relatively smaller sizes. Free GNP formation is not observed at room temperature, but rather the particles originate from the NCNC albeit without defined shape or structure. At 75°C free GNP formation is observed, however the majority of NCNC are decorated to some extent with GNP. These particles vary in their location on the NCNC, but several examples of GNP formed at the opening of the cup are observed. At 100°C free GNP formation has increased substantially resulting in small GNP not attached to the NCNC structure. While some NCNC are shown to be decorated with GNP, there does not seem to be any preference for the opening of the cup as opposed to sidewall attachment. Therefore, ideal GNP formation seems to take place at 75°C in the presence of trisodium citrate.

As trisodium citrate is present for the most effective decoration of NCNC with GNP, it begs to follow that the same factors governing the Turkevich method of GNP formation would also affect the NCNC decoration and resulting morphology of the GNP. The remaining factors

with the biggest impact on GNP synthesized from the Turkevich method are the pH, concentration of gold precursor, concentration of reducing agent, and the ionic strength of the solution. While these factors are all intertwined to some extent,[60] looking at each one individually can provide insight into the most effective method for GNP corking of NCNC. pH is of central importance to biological applications and therefore was investigated first. Extreme and slight changes in pH were made to the GNP decoration solutions through the addition of either HCl or NaOH as shown in Figure 3–4. At very extreme pH values, 2 and 12, no GNP decoration was observed on the NCNC. However, slight changes to pH did not have a drastic effect on the formation of GNP. Optimum GNP decoration appears to occur at a neutral pH of 7. Multiple NCNC are observed with GNP lining the opening of the cup. Moderate changes to pH show varying effects depending on whether the solution is basic or acidic. At a slight basic pH of 8, GNP decoration seems to decrease as compared to the neutral conditions with no corking observed in the material. However, at more acidic pH, while GNP formation does decrease, several NCNC are still seen with GNP formation at the open end of the cup. This aligns with free GNP synthesis as slightly acidic pH values have been shown to provide the most control over the formation of free GNP. It appears as though corking can successfully be achieved at neutral pH and even at slightly acidic pH values. However, the presence of chloride ions from the addition of HCl can also play a role in the speciation of the $HAuCl_4$ precursor and therefore have a significant effect on the GNP formation. Additionally, for *in vivo* applications, corking in buffered solutions with higher ionic strength would be desirable. Therefore, the effect of added salts to the corking solution were explored.

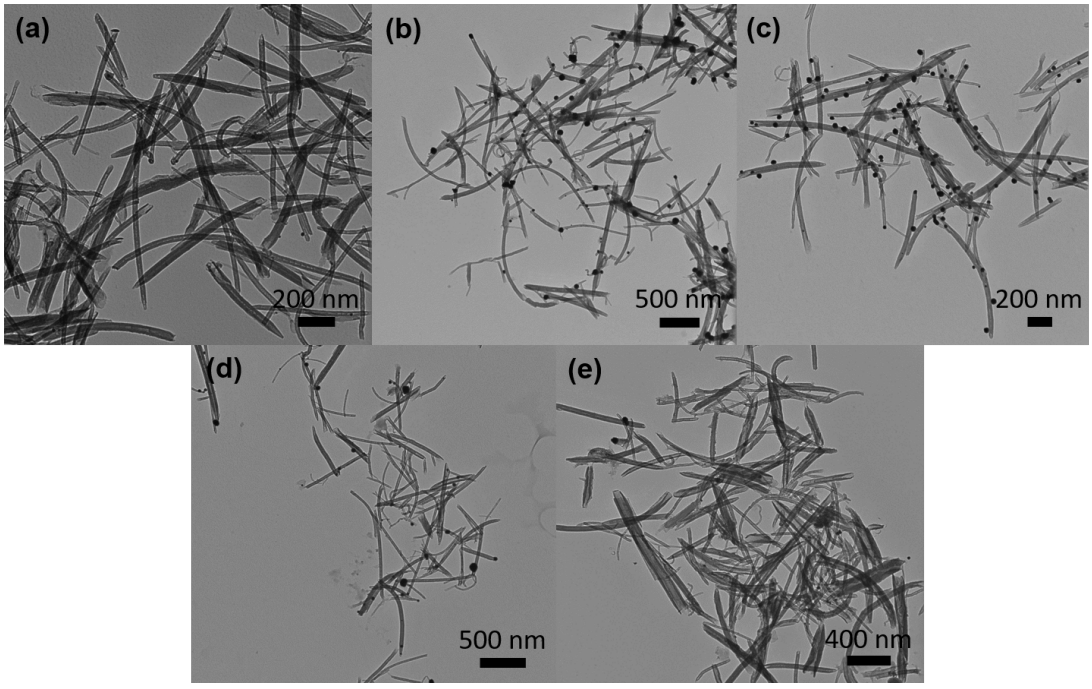

Figure 3-4 Transmission electron microscopy images of NCNC decorated with GNP at pH values of (a) 2, (b) 6, (c) 7, (d) 8, and (e) 12.

We then aimed to identify changes in the GNP decoration of NCNC by altering the ionic strength of the corking solution. As Cl^- ions have been shown to affect the speciation of $HAuCl_4$, we utilized two salts at the same concentration; NaCl which increases ionic strength while adding Cl^- and KNO_3 which increases ionic strength and leaves Cl^- concentration unaffected. Representative TEM images are shown for both experiments in Figure 3–5. Upon the addition of NaCl, GNP formation is still observed with most NCNC being decorated with GNP with several having GNP formed on the open end of the cup. The addition of KNO_3 also does not seem to alter GNP formation although the number of GNP corked NCNC does appear to increase over the NaCl sample. These experiments indicate that GNP formation and association to NCNC can still be achieved upon increasing the ionic strength of the solution. The desire to use buffered corking conditions should therefore have little effect on the synthesis of GNP corked NCNC.

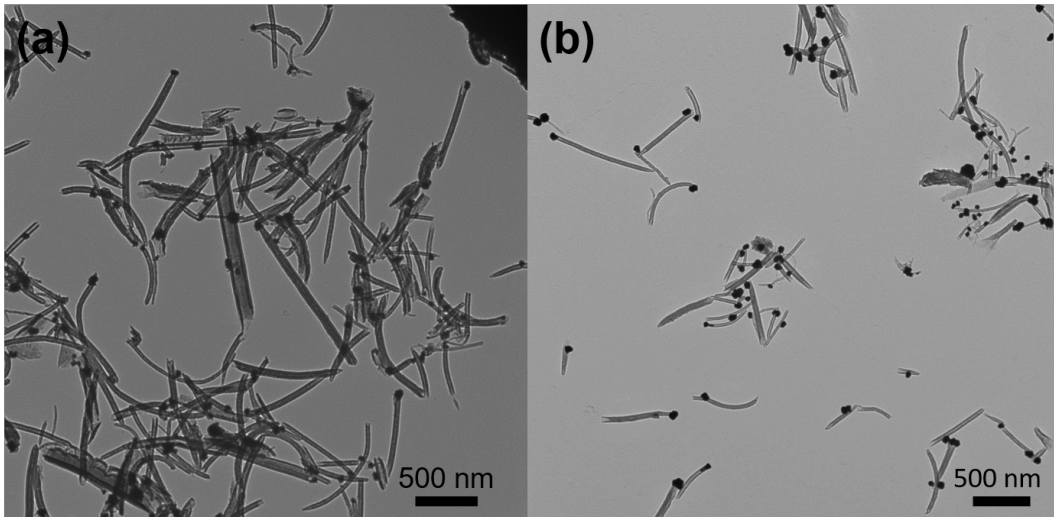

Figure 3-5 Transmission electron microscopy images of GNP decoration with the addition of (a) 0.62 mM NaCl, and (b) 0.62 mM KNO_3.

The normal corking conditions, as illustrated in Figure 3–3d, use concentrations of 1.27 mM $HAuCl_4$ and 1.02 mM trisodium citrate. Decreasing the amount of reducing agent in the GNP synthesis will result in a decrease in initial gold cluster formation with fewer nanoparticle seeds being formed. As the initial seed step is important for determining the number of the synthesized GNP, changes in metal decoration of NCNC in response to changes in trisodium citrate concentration need to be explored. Additionally, an increase in the amount of gold precursor will allow for larger GNP to form from the initial gold seeds. Both of these factors need to be investigated to determine the ideal ratio of gold precursor to reducing agent for effective GNP decoration and corking. The concentrations of the trisodium citrate and the $HAuCl_4$ were halved and doubled individually as shown in Figure 3–6. When the $HAuCl_4$ concentration is halved, larger gold aggregates were formed and less efficient NCNC decoration was observed. When the $HAuCl_4$ concentration is doubled, GNP are found to be associated to the NCNC, however they show signs of growing outward from the particle forming nanowires. Additionally, the number of free GNP

increases, and these free GNP show similar nanowire formation due to the increased $HAuCl_4$ concentration.

Alterations in the trisodium citrate concentration have a less substantial effect on the GNP formation. At both higher and lower trisodium citrate concentrations larger gold aggregates can be observed. However, both samples show NCNC decoration with many cup segments effectively corked with GNP. This is in stark contrast to normal Turkevich method as the concentration of trisodium citrate plays a critical role in the formation of uniform GNP.[60] We believe this is due to the fact that NCNC have the ability to reduce gold on their own and therefore produce the gold seeds which grow into larger GNP corks. The NCNC are first incubated with $HAuCl_4$ for 20 minutes before the addition of the trisodium citrate. This incubation period allows the NCNC to begin reducing gold species for the formation of gold seeds. Once the trisodium citrate is added, free $HAuCl_4$ is reduced and the seeded GNP grow into larger complete nanoparticle corks. The results of these investigations illustrate the robust nature of the NCNC decoration with GNP where pH, precursor concentrations, and ionic strength have less pronounced effects on the overall nanoparticle formation as compared to the free GNP synthesis by the Turkevich method. While free GNP formation is dependent on a delicate balance between all of these factors, the decoration of NCNC, and presumably other CNM, does not seem to be affected by changes in these parameters. This may provide an avenue for facilitated GNP formation through the use of carbon scaffolds as patterning substrates. Throughout the investigations of GNP synthesis parameters and their effect on GNP corking of NCNC, optimum conditions resulted in 40% of NCNC having their open end being sealed with a GNP. This material will be referred to Au-NCNC for future reference.

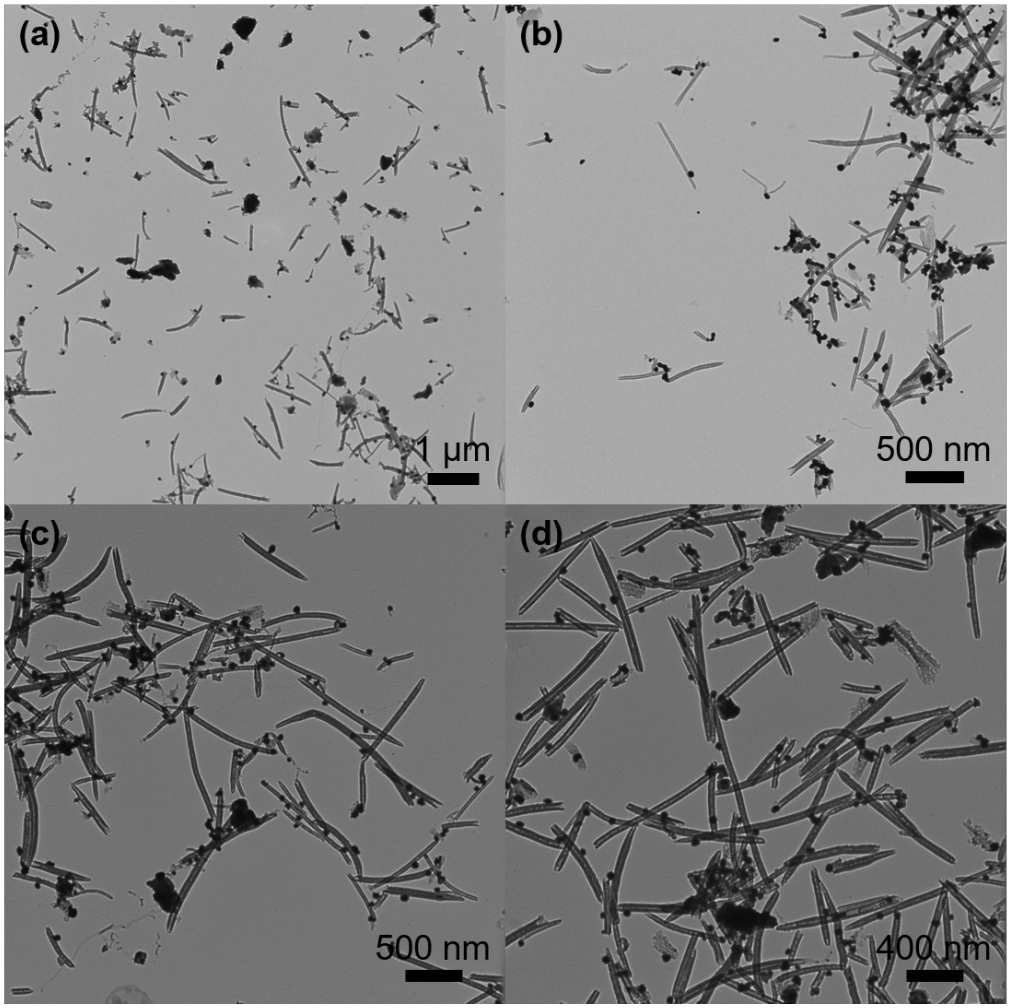

Figure 3-6 Transmission electron microscopy images of GNP decoration reactions with (a) 0.635 mM $HAuCl_4$, (b) 2.54 mM $HAuCl_4$, (c) 0.51 mM trisodium citrate, and (d) 2.04 mM trisodium citrate.

Once bound to the open end of the cups, the GNP appears to adapt to the shape of the opening completely sealing the interior space. To evaluate the seal between the GNP and the NCNC, Au-NCNC were exposed to high temperatures and oxygen atmosphere in an environmental TEM to determine the effect these oxidizing conditions have on the resulting material. Interestingly, when Au-NCNC are exposed to oxidizing conditions, the external graphitic walls seem to degrade while the interior cavity remains primarily unaffected as shown in Figure

3–7. As the inner cavity remains intact, it begs to follow that any loaded cargo within the interior of the Au-NCNC would also be protected from the external environment.

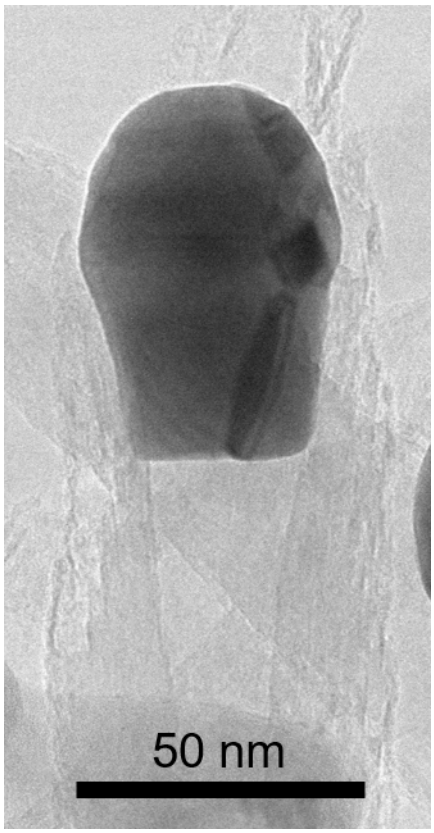

Figure 3-7 High-resolution transmission electron microscopy image of gold corked NCNC (Au-NCNC) exposed to 7×10^{-4} Torr O_2 at 400°C showing the external degradation of Au-NCNC while the inner cavity remains intact. Adapted from reference.[190]

The presence of GNP on the NCNC causes a strong SERS effect, allowing sensitive detection of this hybrid material by Raman spectroscopy in biological samples. Figure 3–8 shows the Raman spectra of NCNC decorated with GNP as compared to unfunctionalized NCNC. Enhancements of about 15- and 18- fold were noticed for the intensities of D (~1350 cm^{-1}) and G (~1582 cm^{-1}) bands, respectively. We speculate that the SERS effect mainly originates from the

charge transfer between GNP and NCNC due to electronic interaction between the two, as a result of direct contact.[191] By physically mixing NCNC with commercial citrate-coated GNP, free GNP are randomly distributed together with NCNC showing no specific interaction and the SERS effect was not observed. This SERS effect represents a mechanism for not only tracking the removal of the GNP cork from the NCNC but may also be used to determine the successful loading of the NCNC through SERS enhancement of the loaded cargo.

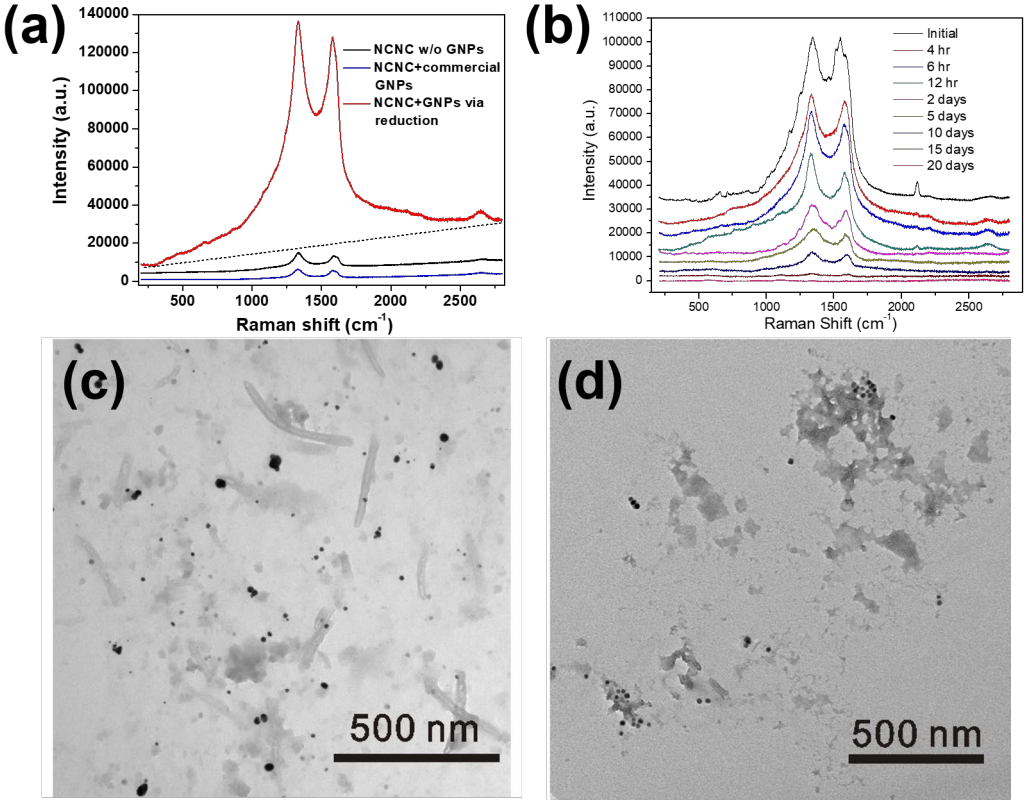

Figure 3-8 Raman spectra of (a) NCNC (black), NCNC mixed with commercial GNP (blue), and NCNC corked with GNP by in situ reduction of $HAuCl_4$ (red), and (b) Au-NCNC in response to ezymatic oxidation of incubation in hMPO/H_2O_2/NaCl. Transmission electron microscopy images of Au-NCNC in response to enzymatic oxidation after (c) 5 days and (d) 20 days. Reprinted (adapted) with permission from reference.[167] Copyright 2014 American Chemical Society.

To determine if the SERS effect between the GNP and NCNC can be used to track the uncorking of the material, Au-NCNC were incubated in a mixture of hMPO/H_2O_2/NaCl which has been used for effective degradation of CNM.[74, 99] Raman spectra were taken of the experiment over the course of 20 days with a downward trend in Raman intensity being observed even within the first 4 hours. Looking at TEM on day 5 illustrates that the NCNC are uncorked while the cup structure remains primarily intact. However, by day 20 the NCNC material is almost completely degraded. Therefore, interaction with the oxidative environment not only results in the degradation of the graphitic shell, but also triggered the opening of the NCNC through the release of the GNP cork. Once detached from the NCNC, the GNP fail to induce the SERS effect on NCNC similar to the mixture of NCNC with free GNP. The Raman spectra of the degradation sample show a drastic decrease of D and G band intensities within the first 2 days of degradation, followed by a slower decrease afterward until complete degradation. This indicates that the GNP corks are primarily removed from the NCNC structure within the first two days which explains the sharp decrease in the Raman intensity over that time period. After detachment of the GNP, the remaining graphitic NCNC are degraded which explains the slower decrease in Raman intensity after Day 2.

As the open end of the NCNC have been shown to be effectively corked with GNP, and exposure to oxidative conditions can remove the GNP corks Au-NCNC represent an attractive material for the loading and release of designated cargo. In an effort to prove this, we first loaded the Au-NCNC with Rh123. Rhodamine derivates have been frequently used as Raman probes for high-sensitivity SERS analysis.[192] Rh123 was first mixed at a concentration of 0.15 μM with NCNC in water, followed by incubation with $HAuCl_4$ and reduction by trisodium citrate. The solution is then repeatedly washed with ethanol and water to remove any free Rh123, TEM images indicate that the addition of Rh123 to the corking solution at this concentration does not influence

the formation of GNP corks on the NCNC. We expect the poor solubility of Rh123 in water to drive its loading into the interior of the NCNC through. As a control, Rh123 was added at the concentration of 0.15 µM to the pre-made Au-NCNC and washed in the same way. The Raman spectra of these materials were compared to the Raman spectra of pure Rh123 to prove loading of the designated cargo as shown in Figure 3–9.

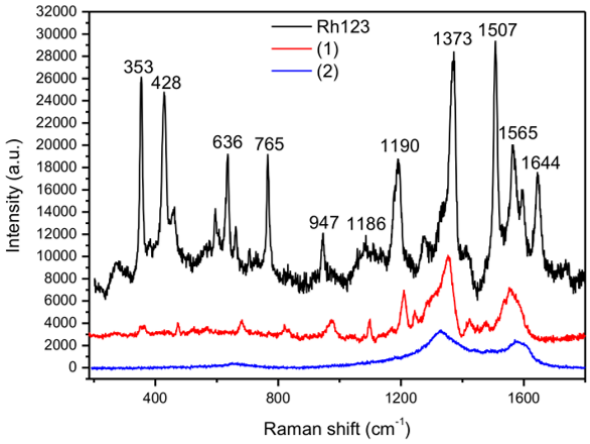

Figure 3-9 Raman spectra of free Rh123 drop-cast on a glass slide at the concentration of 0.15 µM (black), (1) the precipitate of NCNC functionalized with GNP in the presence of 0.15 µM Rh123, after repetitive wash, and (2) the precipitate of 0.15 µM Rh123 mixed with as-synthesized Au-NCNC conjugates, after repetitive wash. Reprinted (adapted) with permission from reference.[167] Copyright 2014 American Chemical Society.

The pure Rh123 sample on a glass slide gave multiple peaks between 300 and 1700 cm^{-1} in good agreement with the literature.[193] The Au-NCNC sample prepared in the presence of Rh123 shows similar peaks as the pure Rh123, while the Au-NCNC sample mixed with Rh123 post-synthesis does not show any characteristic Rh123 Raman peaks. It is inferred that the repeated wash procedure is able to remove any untrapped free Rh123 molecules outside the cups, while the remaining Raman signals in the Rh123 loaded Au-NCNC after wash may be incurred from the trapped Rh123 adsorbed on the inner surface of the GNP corks. These results suggest that Rh123

can indeed be trapped inside the NCNC after the corking of GNP but is not able to bind tightly on the outer GNP or NCNC surfaces. The slight shift of the characteristic peaks of Rh123 in the corked NCNC samples from the pure chemicals can be due to band stiffening as a result of charge transfer between the GNP and the analytes.[194] Because different vibrational modes may be enhanced differently, the relative intensities of the peaks also vary from the spectra of the pure chemical.

In order to prove the release of loaded cargo from Au-NCNC, Rh123 loaded Au-NCNC were exposed to enzymatic oxidation over 5 days with the resulting fluorescence of the solution measured. Rh123 has strong fluorescence around 520 nm when excited at 500 nm. Rh123 loaded Au-NCNC were incubated in MPO, NaCl, and H_2O_2 for 5 days with fluorescence measurements taken every day; the observance of a fluorescent signal would indicate the release of Rh123 from the inner cavity of the Au-NCNC illustrating uncorking. As shown in Figure 3–10, fluorescence intensity is low on Day 0 but spikes rapidly after 24 hours. This spike in fluorescence indicates the removal of the GNP cork in response to enzymatic oxidation and subsequent burst release of the loaded cargo. This intensity however fades after 48 and 72 hours which is hypothesized to be due to enzymatic degradation of the Rh123 molecule. As shown in Figure 3–10b, when 0.01 mg/mL Rh123 is exposed to the same enzymatic degradation conditions as Rh123 loaded Au-NCNC the UV-Vis absorbance of the molecule decreases over time. Therefore, the Au-NCNC container protects its loaded cargo from degradation as free molecules are rapidly consumed. Interestingly, a second fluorescence peak is observed after 96 hours which may relate to a second release profile of Au-NCNC. The initial spike in fluorescence could be due to the release of the loosely bound Rh123 particles, while the second fluorescence peak represents the release of tightly bound Rh123 which can only occur once the graphitic lattice of the NCNC begins to be degraded. This indicates

a burst release in addition to a long-term release profiles which may result in unique therapeutic applications.[195]

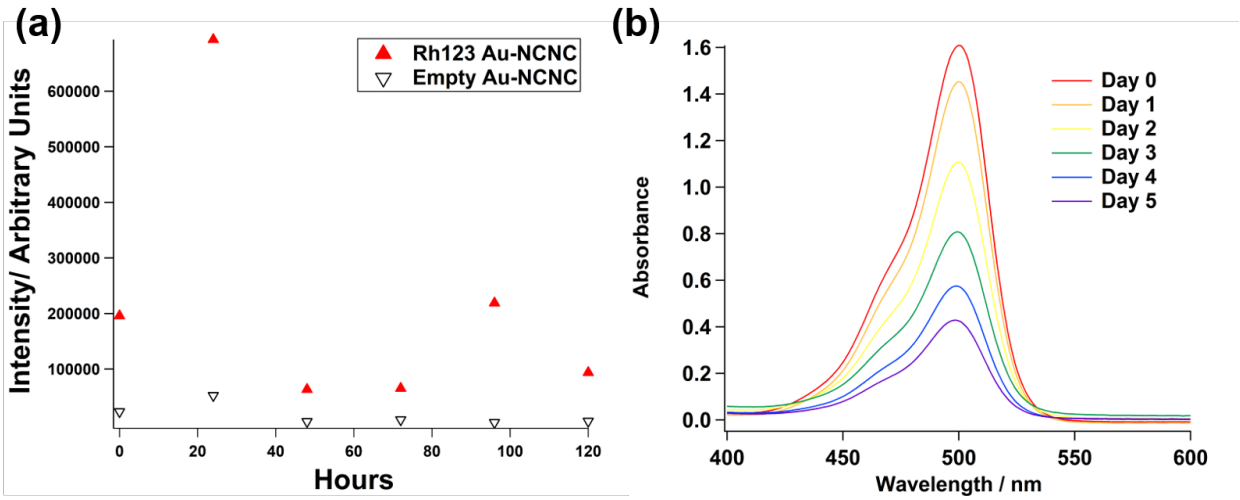

Figure 3-10 (a) Fluorescence intensity of Rh123 loaded Au-NCNC in response to enzymatic oxidation. (b) UV-Vis spectra of the enzymatic degradation of Rh123 with an initial concentration of 0.01 mg/mL.

3.4 Conclusions

NCNC are able to be isolated from the stacked fiber through a combination of acid oxidation and high-intensity probe-tip sonication. Through a trisodium citrate reduction, the separated NCNC can be effectively corked with GNP on their open rims due to the preferential distribution of amine functionalities on the open end of the NCNC. Unlike free GNP synthesis which is heavily dependent on pH, precursor concentrations, and ionic strength, GNP decoration of NCNC is relatively unphased by alterations in solution factors. The resulting Au-NCNC can be effectively opened through enzymatic oxidation, followed by complete degradation of the graphitic NCNC container. Finally, Au-NCNC can be loaded with cargo as confirmed through

SERS enhancement of the Raman signals by the GNP cork and effectively released through enzymatic oxidation. The results here illustrate the capability of Au-NCNC for effective drug delivery which will be further explored in Chapter 4.

3.5 Acknowledgement

This work at the University of Pittsburgh was supported by an NSF CAREER Award No. 0954345, NIH R01ES019304, RO1CA154369, U19 AI068021, HL114453, and NIOSH OH008282. We thank the Nanoscale Fabrication and Characterization Facility and the Department of Biological Sciences at the University of Pittsburgh for provision of access to the TEM and Raman instruments.

4.0 Loading Au-NCNC with cargo and enzymatic delivery

4.1 Introduction

In Chapter 3 we evaluated the propensity for separated NCNC to be decorated and effectively corked with GNP as a novel class of drug delivery vehicles. It was illustrated that Au-NCNC can be loaded with cargo as determined by SERS enhancement of the cargo's Raman peaks and effectively released through exposure to enzymatic oxidation. This was tested with Rh123 which has characteristic Raman peaks as well as fluorescent properties to track its release. We now turn our attention to a more practical application which is the use of a common chemotherapeutic agent, paclitaxel, which has been used extensively in cancer therapy. Research has shown that ultra-low doses of paclitaxel to a subset of cancer cells known as MDSC can result in their differentiation into DC and subsequent restoration of immune response. MDSC are characterized by an upregulation of the enzymatic machinery which has been shown to degrade and uncork Au-NCNC and therefore represent an attractive delivery mechanism. Paclitaxel loaded Au-NCNC were first thoroughly characterized to confirm loading and release. Next, Au-NCNC were tested *in vitro* to confirm their ability to be degraded and release paclitaxel for restoration of immune function. Finally, Au-NCNC were tested *in vivo* in tumor bearing mice with effect on cell differentiation and tumor growth characterized.

The *in vitro* results of this project were published in the following article

Nano-Gold Corking and Enzymatic Uncorking of Carbon Nanotube Cups. *Journal of the American Chemical Society* **2015**, *137*(2), 675–684, Copyright © 2015, American Chemical Society. The full citation is listed as reference[167] in the bibliography section.

List of Authors: Yong Zhao, Seth C. Burkert, Yifan Tang, Dan C. Sorescu, Alexandr A. Kapralov, Galina V. Shurin, Michael R. Shurin, Valerian E. Kagan, Alexander Star

Author Contributions: All authors contributed to the design of experiments and writing of the paper. YZ and SCB carried out corking and loading experiments. YZ, YT, and SCB performed material characterization. DCS led the theoretical study. AK and VEK performed cellular studies. GVS and MRS performed *in vitro* experiments.

The *in vivo* results of this project were published in the following article

Targeting myeloid regulators by paclitaxel-loaded enzymatically degradable nanocups. *Nanoscale* **2018**, *10*(37), 17990–18000, Copyright © 2018 The Royal Society of Chemistry. The full citation is listed as reference[196] in the bibliography section.

List of Authors: Seth C. Burkert, Galina V. Shurin, David L. White, Xiaoyun He, Alexandr A. Kapralov, Valerian E. Kagan, Michael R. Shurin, Alexander Star

Author Contribution: All authors contributed to the design of experiments and writing of the paper. SCB carried out the corking and loading experiments and Au-NCNC characterization. DLW performed high-resolution TEM. XH performed MS quantification of paclitaxel. AAK and VEK quantified MPO activity and peroxynitrite activity. GVS and MRS performed *in vivo* experiments.

Nanocarriers are emerging as a valuable tool set in delivering therapeutics in experimental and clinical oncology. Several types of nanocarriers based primarily on liposomes and polymer-protein conjugates have already been approved for clinical use.[197] Recent innovations in nanoscience and nanotechnology are driving novel nanocarriers to clinical translation. CNT are ideal vehicles for this purpose because of the potential for chemical functionalization, proven ability to penetrate mammalian cells and transport biological macromolecules including peptides, proteins, and nucleic acids, and tunable lengths (up to several microns) that can be tailored for cell

or organelle penetration.[22, 198, 199] However, specialized nanomaterials for precision targeting of the immunosuppressive tumor environment have been difficult to achieve due to the heterogeneous nature of tumors.[200, 201]

Targeting MDSC with certain chemotherapeutic agents, *e.g.*, gemcitabine, cisplatin, and 5-fluorouracil, to induce apoptotic death is a generally accepted therapeutic approach.[202-205] Two potential strategies are differentiation of circulating and lymphoid tissue MDSC prior to accumulation in the tumor microenvironment or direct differentiation of the tumor associated MDSC.[206] The method of targeting circulating and lymphoid tissue MDSC has been overlooked in most traditional therapies. Delivery of high-concentrations of chemotherapeutic agents has typically been correlated with toxicity, hypersensitivity reactions, and neuropathy.[207, 208] We have previously demonstrated that low doses of paclitaxel can down-regulate accumulation and function of MDSC in melanoma and up-regulate their differentiation into immune stimulatory DC.[209, 210] However, clinical applicability of cytotoxic drugs for depleting immune regulators is limited by cumulative toxicity, non-specific effects, immunosuppression and possible pro-metastatic activity.[84-86] Thus, novel approaches for controlled delivery and release of chemotherapeutic agents is highly desirable.

We have previously shown the NCNC can be separated into individual and short stacked segments, loaded with cargo, corked with GNP and subsequently uncorked by potent oxidants enzymatically generated in biochemical models or in inflammatory cells. To illustrate the potential of Au-NCNC as drug delivery systems, they were loaded with paclitaxel and incubated with MDSC. The delivery of paclitaxel caused inhibition of immunosuppressive phenotype of MDSC and their differentiation into DC, thus reversing their immunosuppressive activity, providing proof of concept for Au-NCNC as a novel drug delivery system. Au-NCNC have a length scale greater

than 200 nm and are not expected to penetrate the tumor microenvironment as they are too large to be up-taken through the enhanced permeability and retention (EPR) effect.[128] However, due to the overexpression of oxidative biodegradation reagents in MDSC, we expect Au-NCNC to selectively degrade in circulating and lymphoid tissue MDSC resulting in local delivery of paclitaxel and subsequent MDSC differentiation. Here, we report *in vivo* systemic nanodelivery of Au-NCNC containing paclitaxel inhibited melanoma growth in mice with 25–30% of treated mice being tumor free after 2–3 weeks. ICP-MS tracking of gold atoms indicates that the Au-NCNC do not localize in the tumor mass but instead are found in the spleen and liver resulting in a decrease of MDSC as confirmed by flow cytometry. The results of this investigation provide the proof of concept that systemic targeting of MDSC results in anti-tumor effects without specific targeting to the tumor microenvironment.

4.2 Experimental section

4.2.1 Synthesis of Au-NCNC

NCNC were synthesized through CVD synthesis and oxidized through sonication in mineral acids and separated by probe-tip sonication as optimized in Chapter 2.[100, 167, 168] Briefly, 10 mg of NCNC were suspended in 40 mL of a 3:1 (v/v) solution of H_2SO_4:HNO_3 and agitated in a bath sonicator for 8 hours at room temperature. The resulting oxidized NCNC were filtered through a 200 nm PTFE membrane and resuspended in nanopore water (18.2 MΩ·cm). The oxidized NCNC in water were then sonicated for 4 hours with a probe-tip ultrasonicator (Qsonica Q500) equipped with a ½ inch probe. The resulting separated NCNC were used for loading and

corking reactions. NCNC were corked through a trisodium citrate reduction of chloroauric acid as optimized in Chapter 3.[167, 168] NCNC were suspended in 2 mL of 1× phosphate buffer at a concentration of 0.01 mg/mL and stirred on a hot plate at 75°C. A solution of paclitaxel was made in ethanol at a concentration of 2 mg/mL. To load the paclitaxel into the NCNC before gold corking with gold nanoparticles, 50 µL of the paclitaxel solution was added to the NCNC and allowed to stir for 20 minutes. When corking in the absence of paclitaxel 50 µL of ethanol was added to the empty NCNC for consistency between samples. Next, 100 µL of $HAuCl_4$ aqueous solution (1 mg/mL) was added to the NCNC solution and allowed to stir for 20 minutes. After incubation, 60 µL of 1 wt% trisodium citrate solution was added dropwise and the reaction was stirred for 2 hours. Au-NCNC were collected by centrifugation at 1300g for 30 minutes. The resulting supernatant and subsequent washes of the corking solution were analyzed by LC-MS to determine the amount of paclitaxel remaining in solution.

4.2.2 Material characterization

TEM images were taken on a FEI Morgagni microscope with an accelerating voltage of 80 kV. High resolution TEM images were taken on a JEOL 2100F microscope with 200 kV accelerating voltage. Samples were drop-cast on lacey carbon TEM grids. Raman spectra were collected from an XplorA Raman AFM-TERS system with a 638 nm (24 mW) laser at 10% laser intensity and 10 second exposure time. XPS characterization was performed on a Thermo ESCALAB 250 Xi XPS using monochromated Al Kα X-rays as the source. DLS and zeta potential measurements were performed on a Malvern Zetasizer

4.2.3 MPO degradation of Au-NCNC and paclitaxel quantification

Paclitaxel loaded Au-NCNC were suspended in 446 µL of PBS and 50 µL of water, additions of 2 µL of 2.5 g/L MPO every 6 hours and 2 µL of 25 mM H_2O_2 every hour with 12 additions a day. The samples were incubated at 37°C for 48 hours. The resulting solutions were centrifuged at 1300g for 30 minutes with the supernatant (top 400 µL) being taken and the paclitaxel collected by dichloromethane (DCM) extraction. After the DCM extraction, the solvent was evaporated, and the resulting residue was resuspended in 500 µL of methanol for injection into the LC-MS column. For quantification analysis, 20 µL of 0.5 mg/mL docetaxel was added as an internal standard.

Liquid chromatography was performed using a Dionex-Ultimate 3000 (Thermo Fisher Scientific). The column employed was a Luna-C18(2), 100 × 2.0 mm length and 3 µm particle size from Phenomenex. The mobile phases used were 0.1% formic acid in water (A) and 0.1% formic acid in acetonitrile (B). An isocratic program with 50% A and 50% B was used. The flow rate was held constant at 200 µL/min with injection volume of 5 µL.

The LC effluent was pumped into a Q-Exactive benchtop Orbitrap-based mass spectrometer (Thermo Fisher Scientific) with electrospray ionization (ESI) held at a positive polarity. Nitrogen sheath gas and auxiliary gas flow rate were set up at 35 and 10 (arbitrary units), respectively. The capillary temperature was set at 250°C, spray voltage was 3.5 kV and S-lens voltage set to 60 V. The instrument was operated in targeted single ion monitoring (t-SIM) by selecting the targeted compound (*m/z* 854, $[M+H]^+$ for paclitaxel) and the internal standard (*m/z* 808, $[M+H]^+$ for docetaxel) at 70,000 resolving power and the AGC target was 1×10^6.

4.2.4 Measurements of MPO activity and peroxynitrite production by MDSC

Detection of MPO activity and peroxynitrite generation was performed using aminophenyl fluorescein (APF) and hydroxylphenol fluorescein (HPF), respectively. MDSC obtained from normal and B16 melanoma bearing mice were suspended in RPMI 1640 media without phenol red, seeded in a 24-well plate (150×10^3 cells per well in a volume of 400 μL), and incubated in the presence of 5 μM APF or 5 μM HPF for 30 minutes. Activation of cells was performed by addition of 40 nM of PMA. Cell suspensions were analyzed by flow cytometry (FACSanto, BD Biosciences, San Jose, CA).

4.2.5 Animals

6-8 week old male C57BL/6 mice were obtained from Taconic. All animals were housed under the standard controlled conditions, and food and water were available *at libitum*. All animal experiments were approved by the Institutional Animal Care and Use Committee and performed in accordance with the Animal Welfare Act and the federal Public Health Service Policy on the Humane Care and Use of Laboratory Animals.

4.2.6 Isolation, treatment, and evaluation of MDSC

For pulmonary MDSC isolation and analysis, mouse lungs were dispersed using a 2% collagenase A and 0.75% DNase I (Roche Diagnostics GmbH, Mannheim, Germany) in RPMI 1640 medium supplemented with 10% FBS at 20°C for 1 hour in Miltenyi Biotec gentleMACS Dissociator. Bone marrow cells were isolated, filtered through a 70 μm cell strainer, and red blood

cells were lysed with lysing buffer (155 mM NH_4Cl in 10 mM Tris-HCl buffer pH 7.5, 25°C) for 3 minutes. After RBC lysis, cells were washed and used for MDSC sorting. CD11b+ Gr-1+ MDSC were isolated from the digested lungs and bone marrow cell suspensions by magnetic cell sorting using a mouse MDSC Isolation Kit (MACS, Miltenyi Biotec, Auburn, CA) according to the manufacturer's instructions. Control MDSC were isolated from tumor-free mice. After isolation, all MDSC were cultured with empty and paclitaxel-loaded Au-NCNC for 48 hours.

For testing the effect of Au-NCNC on MDSC function, bone marrow-derived MDSC from tumor-free and B16-bearing melanoma mice were treated with Au-NCNC as above and mixed with T cells at different ratios (1/10–1/100) for 24 hours. Syngeneic T lymphocytes were isolated from the spleen of tumor-free mice by nylon wool enrichment method and preactivated with Concanovalin A (5 hours, 2.5 μg/mL, Sigma, St. Louis, MO). T cell proliferation was measured by uptake of 3H-thymidine (1 μCi/well, 5 Ci/mmol; DuPont-NEN, Boston, MA) pulsed for 16–18 hours. Cells were harvested on GF/C glass fiber filters (Whatman Intl. Ltd., Maidstone, UK) using MACH III microwell harvester (Tomtec, Hamden, CT). 3H-thymidine incorporation was determined on MicroBeta TRILUX liquid scintillation counter (WALLAC, Finland) and expressed as count per minute (cpm).

Production of TGF-β by the bone marrow MDSC isolated from tumor-free and B16-bearing mice was determined by assessing the levels of TGF-β1 in cell-free supernatants by ELISA (R&D Systems, Minneapolis. MN).

Differentiation of MDSC into DC was evaluated in lung MDSC cultures treated with NCNC for 48 hours by staining cells with anti-CD11b, anti-Ly6G, anti-Ly6C, anti-Gr-1, and anti-CD11c antibodies (Biolegend Inc., San Diego, CA) directly conjugated to FITS, PE, PE/Cy7, or APC/Cy7, and analyzed by flow cytometry (BD FacsCalibur) and FlowJo Software.

4.2.7 Cell cultures

Murine B16 melanoma cell line (American Type Culture Collection) was maintained in a complete RPMI 1640 medium (GIBCO BRL) supplemented with non-essential amino acids, 10% heat-inactivated fetal bovine serum (FBS), 2 mM L-glutamine, 100 IU/mL penicillin, and 100 μg/mL streptomycin. All tumor cell line cultures were mycoplasma free.

4.2.8 Animal tumor models and experimental designs

B16 cells (5×10^4 in 100 μL of saline) were inoculated s.c. in a flank of syngeneic C57BL/6 mice on Day 0. Six days later, tumor-bearing mice were injected i.v. with (i) saline (300 μL, control), (ii) control empty Au-NCNC, (iii) paclitaxel loaded Au-NCNC (300 μL per mouse), and (iv) free paclitaxel (80 μg per mouse). The administered free paclitaxel dosage was determined by taking our maximum delivered dosage from paclitaxel loaded Au-NCNC plus an additional 20%. Paclitaxel was purchased from Mayne Pharma. The tumor size was detected twice per week and expressed as the tumor area (mm^2). All studies included 5–7 mice per group and were independently repeated 2 or 3 times.

For MDSC analysis, tumor tissues were dispersed using 2% collagenase A and 0.75% DNAse I (Roche Diagnostics, Manheim, Germany) in RPMI 1640 with 10% FBS at 20°C for 1 hour using gentleMACS Dissociator (Milteyi Biotec) according to the manufacturer protocols. Spleens were harvested into 5 mL of complete RPMI 1640 medium in a sterile culture dish, grounded, and cell suspensions were filtered through a 70 μm cell strainer. Red blood cells in the lung and spleen were lysed with lysing buffer (155 mM NH_4Cl in 10 mM Tris-HCl buffer pH 7.5, 25°C) for 3 minutes. After RBC lysis, cells were washed 2 times with FACS buffer (PBS

containing 0.1% BSA and 0.05% sodium azide (Sigma, St Louis, MO)). Cell suspensions were labelled with anti-Ly6G, anti-Ly6C, anti-GR-1, and anti-CD45 antibodies (Biolegend Inc., San Diego, CA) directly conjugated to FITC, PE or Alexa700. Stained cell suspensions were analyzed by flow cytometry (FACSalibur, BD Biosciences, San Jose, CA). Data on MDSC levels in the tumor, lung, and spleen are presented as the percentage of cells gated on CD45+ cells.

4.2.9 Detection of gold atoms *in vivo*

Tissue samples were digested based upon a previously published procedure.[211] First, tissue samples were snap frozen in liquid nitrogen and freeze-dried overnight in a Labconco Freezone 6 lyophilizer to remove all water. Each tissue sample was then digested to white ash through the addition of 500 µL of 30% hydrogen peroxide at room temperature. The digested white ash was then further dissolved by the addition of 500 µL of HNO_3. The samples were allowed to sit for 2 days to allow for complete digestion. The samples were then diluted by the addition of 500 µL of nanopore water. In order to dissolve the residual gold from the tissue samples several drops of an *aqua regia* solution, 3:1 hydrochloric acid (Sigma-Aldrich, >99.999% trace metal basis): nitric acid (Sigma-Aldrich, >99.99% trace metal basis), was added to each digested sample and allowed to sit overnight. The resulting solution was filtered through a 200 nm polyvinylidene fluoride (PVDF) syringe filter to remove any undigested tissue.

Inductively-coupled plasma mass spectrometry (ICP-MS) analysis was performed using an argon flow with a NexION spectrometer (PerkinElmer, Inc.). An *aqua regia* solution was prepared and diluted with water for a 5% (by volume) *aqua regia* matrix. Unknown Au concentrations were determined by comparison to a 5-point standard curve with a range of 1-30 ppb (1, 5, 10, 20, and 30 ppb prepared by volume) from a gold standard for ICP (Fluka, TraceCERT 1.001 ± 2 mg/L Au

in HCl) diluted in the 5% *aqua regia* matrix. All standards were measured 5 times and averaged, while the unknown samples were measured in triplicate and averaged. A 5 minute flush time with a 5% *aqua regia* matrix was used between all runs, and a blank was analyzed before each unknown sample to confirm removal of all residual metals from the instrument.

4.2.10 Statistical analysis

For a standard comparison of two groups, the Student *t*-test was used after evaluation of normality. If data distribution was not normal, a Mann Whitney rank sum test was performed. For the comparison of multiple groups, analysis of variance was applied. SigmaStat Software was used for the data analysis (SyStat Software, Inc.). For all statistical analyses, $p < 0.05$ was considered significant. All experiments were repeated at least two times. Data are presented as the mean ± SEM. Average length and width of Au-NCNC were determined by TEM from 140 measurements and reported as the mean ± standard deviation. DLS size distribution was determined from an average of 3 measurements and reported as the mean ± standard deviation. Zeta potential was determined from an average of 9 measurements and reported as the mean ± standard deviation. LC-MS quantification of paclitaxel loading was performed from 6 individual trials with the average being reported ± standard deviation.

4.3 Results and discussion

The principles of synthesis for Au-NCNC are illustrated in Figure 4–1. Briefly, NCNC were synthesized through a liquid injection CVD method and subsequently separated through

oxidation with mineral acids followed by probe-tip ultrasonication. The resulting separated NCNC were effectively corked with GNP through a trisodium citrate reduction with $HauCl_4$. As was shown in Chapter 3, the gold nanoparticles preferentially attach to the open end of the separated NCNC due to strong attraction to the dangling amine groups produced through intense probe-tip ultrasonication.[167]

For *in vivo* application of Au-NCNC, alterations to the corking procedure were made to produce sterile Au-NCNC. In order to mimic the biological environment Au-NCNC will be opened under; corking reactions were performed in 2 mL of 1×phosphate buffer (PBS). Corking the NCNC in PBS, as opposed to the normal corking procedure in nanopore water, should also mitigate changes in local biological ion concentrations. Additionally, 50 μL of ethanol was added to the corking reactions to sterilize the Au-NCNC from biological contaminants and to enhance the solubility of paclitaxel in the aqueous corking environment. We believe that the loading of NCNC with paclitaxel is due to its poor aqueous solubility resulting in attraction to the hydrophobic interior of the cup *via* a nanoprecipitation reaction facilitated by the evaporation of ethanol from the aqueous corking environment. Nanoprecipitation has previously been reported as an effective technique for loading cisplatin into analogous single-walled carbon nanohorns.[212]

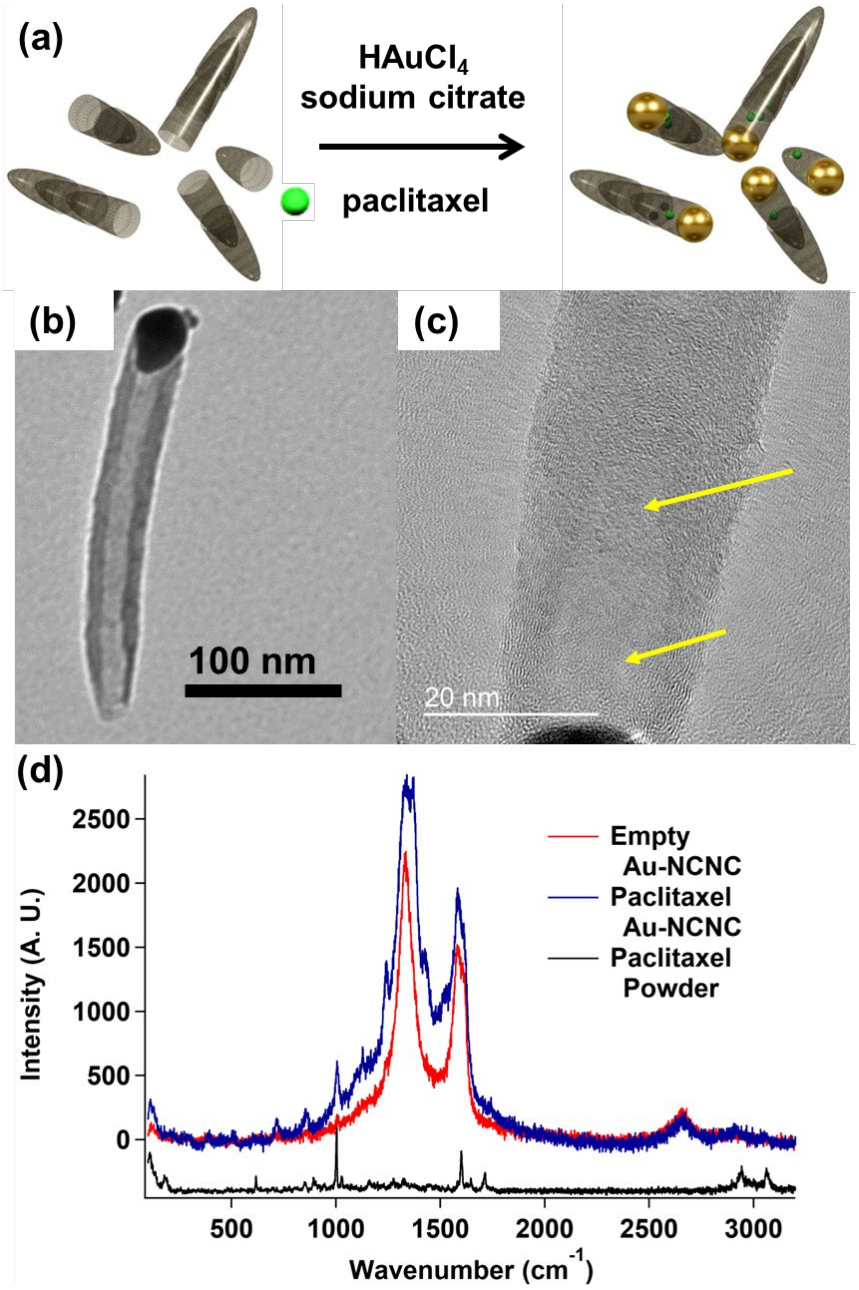

Figure 4-1 (a) Principles of synthesis for the loading and corking of Au-NCNC. (b) A representative transmission electron microscopy (TEM) image of Au-NCNC. (c) High resolution TEM image illustrating the presence of paclitaxel inside the Au-NCNC, the presence of paclitaxel is highlighted with yellow arrows. (d) Raman spectra of empty Au-NCNC, paclitaxel loaded Au-NCNC, and paclitaxel powder. Reproduced from reference[196] with permission from The Royal Society of Chemistry.

A representative TEM image of the final Au-NCNC is shown in Figure 4–1b. As can be seen, the GNP forms a seal around the open end of the NCNC. Loading of paclitaxel into the hollow inner cavity of NCNC is illustrated by high resolution TEM (Figure 4–1c). Dark areas in the central cavity are observed lacking discernible crystallinity indicating they are not due to the structure of the NCNC. Finally, paclitaxel loading was confirmed by Raman spectroscopy. GNP enhance the Raman signatures of NCNC and the loaded paclitaxel through surface enhancement effects as demonstrated in the Raman spectra of the NCNC under low laser intensity (Figure 4–1d). Changes in the chemical and physical properties of Au-NCNC were monitored due to modifications in the corking procedure for *in vivo* delivery of paclitaxel. This information is included as supporting information in Chapter 6. The resulting paclitaxel loaded Au-NCNC have an average length of 550 nm ± 260 nm and average width of 55 nm ± 17 nm as measured by TEM. Length distribution was confirmed with DLS measurements with an average size of 513 nm ± 21 nm. Furthermore, the zeta potential of the paclitaxel loaded Au-NCNC was found to be –39.9 mV ± 1.9 mV in nanopure water at a pH of 6 indicating colloidally stable particles as shown in Figure 4–2.

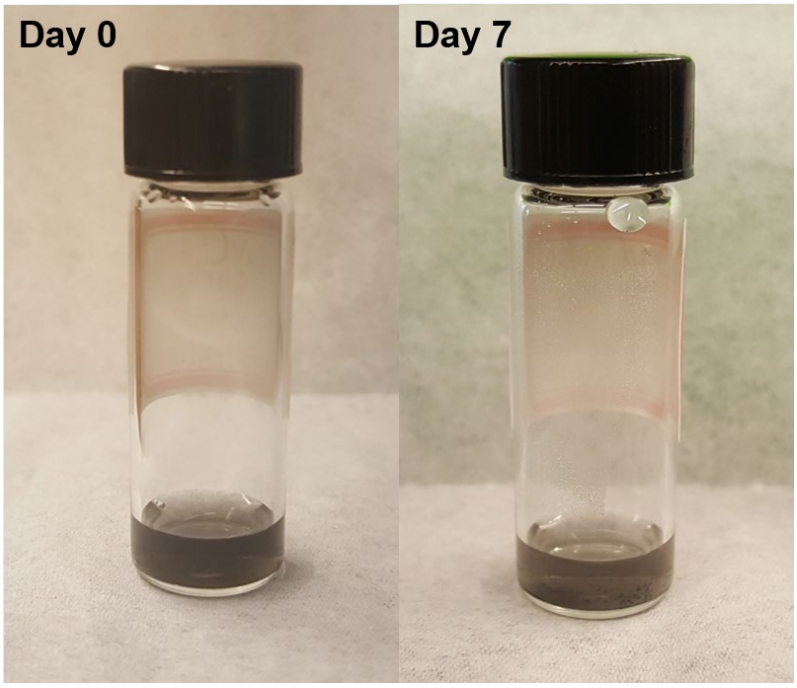

Figure 4-2 Photographs of paclitaxel loaded Au-NCNC on Day 0 and Day 7 illustrating colloidal stability of the particles. Reproduced from reference[196] with permission from the Royal Society of Chemistry.

LC-MS was utilized to track paclitaxel for two goals: (1) establish that paclitaxel is loaded within the interior of Au-NCNC and is released upon incubation with MPO/H_2O_2/Cl^- and (2) determine the amount of the loaded paclitaxel. Successful observation of paclitaxel by LC-MS enabled quantification through comparison with an internal standard, docetaxel, and creating a calibration curve of the area ratios between the two molecules.[213] A calibration curve for quantifying paclitaxel in the µg/mL range was constructed and is available in Chapter 6 supporting information. The supernatant of the corking solution after centrifugation and the resulting washes were analyzed by LC-MS to determine the amount of paclitaxel remaining in solution after the corking reaction. The initial corking solution had 100 µg of paclitaxel and the remaining supernatant and washing solution had 64 µg ± 23 µg. Therefore, the amount of loaded paclitaxel

to the interior of Au-NCNC is 36 µg ± 23 µg resulting in a roughly 36% loading efficiency which correlates with our previously reported corking efficiency based on TEM.[167]

Paclitaxel loaded Au-NCNC were incubated with MPO and H_2O_2 in PBS buffer for 0, 24, and 48 hours. Upon completion of the MPO uncorking of the paclitaxel loaded Au-NCNC, the solution was centrifuged and the supernatant collected for paclitaxel extraction. DCM extraction was performed to collect any released paclitaxel resulting from uncorking. As a control, an empty Au-NCNC sample was also incubated with MPO and H_2O_2 for 48 hours with the same extraction performed. The amount of paclitaxel in these samples was quantified through LC-MS and the constructed calibration curve as seen in Table 4–1. At 0 hours, the area ratio of the paclitaxel is low enough that it can be assumed no paclitaxel is present. After 24 and 48 hours of incubation with MPO and H_2O_2, paclitaxel begins to be released from the cups as the released mass of paclitaxel in the solution is 0.302 µg and 0.910 µg respectively. The empty control sample does not show any paclitaxel indicating that no by-products of the MPO oxidation of Au-NCNC interfere with the paclitaxel quantification. These results demonstrate that paclitaxel is released slowly over time as only 3% of the loaded paclitaxel has been released after 48 hours of incubation with MPO. The interaction of paclitaxel with the interior of the NCNC is strong enough to require complete degradation of the NCNC for total release of paclitaxel despite uncorking of gold occurring after 24 hours. We hypothesize that this strong interaction promotes a slow delivery of the therapeutic agent.

Table 4-1 Released paclitaxel upon uncorking of Au-NCNC

Sample	Area Ratio	Taxol release (µg)
0 hour	0.010	–
24 hours	0.088	0.302
48 hours	0.265	0.910
48 hours control	0.009	–

The release of paclitaxel is also correlated to the uncorking of the Au-NCNC as observed by TEM and Raman spectroscopy shown in Figure 4–3. Au-NCNC were incubated with MDSC for 48 hours before being collected. The GNP corks are removed from the NCNC where the inset TEM image shows a GNP which is only partly associated to the opening of the NCNC. Au-NCNC were incubated with MPO, H_2O_2, and NaCl for 0, 24, and 48 hours before being collected and Raman spectra measured. As MPO incubation proceeds the GNP are removed from the NCNC, as evidenced by TEM images, thus lowering the Raman enhancement due to the association of the plasmonic particles with the graphitic structure. For comparison a Raman spectrum of separated NCNC without any attached GNP is also presented.

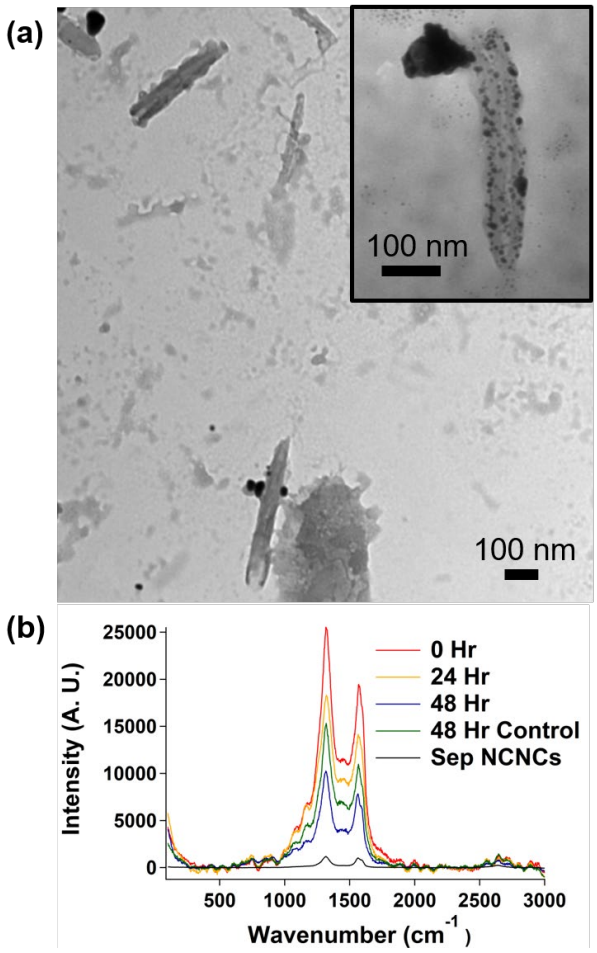

Figure 4-3 (a) Transmission electron microscopy images illustrating the uncorking and degradation of Au-NCNC upon incubation with MDSC. (b) Raman spectroscopy illustrating the uncorking of Au-NCNC upon incubation with MPO, H_2O_2, and NaCl in comparison to pristine NCNC. Reproduced from reference[196] with permission from the Royal Society of Chemistry.

We expect MDSC from tumor-bearing mice to be highly effective in opening and degrading Au-NCNC due to high levels of expression of MPO, NADPH oxidase, and iNOS. In fact, tumor-activated MDSC from tumor-bearing animals exert a higher level of MPO and $ONOO^-$ generating activity than non-activated MDSC from control, tumor-free mice as illustrated in Figure 4–4. In these experiments, we used aminophenyl-fluorescein (APF) as a substrate for MPO and hydroxyl-phenyl fluorescein (HPF) for assessments of peroxynitrite-driven oxidants.[214, 215] In both

cases, highly fluorescent products were formed after oxidation reactions driven by MPO or $ONOO^-$, respectively. We observe a ~2 fold higher oxidative potency detectable in the presence of MDSC from tumor-bearing animals compared to control non-activated cells ($p < 0.05$). The addition of Au-NCNC caused a marked decrease in HPF/APF fluorescence emission intensity ($p < 0.05$), indicating that a significant portion of the reactive intermediates was interacting with Au-NCNC rather than with the fluorescent probes. Therefore, MDSC from tumor-bearing mice produce larger amounts of oxidizing agents providing an avenue for degradation of the paclitaxel loaded Au-NCNC. The pro-oxidative environment allows the Au-NCNC to be selectively degraded within MDSC minimizing the need for targeting ligands.

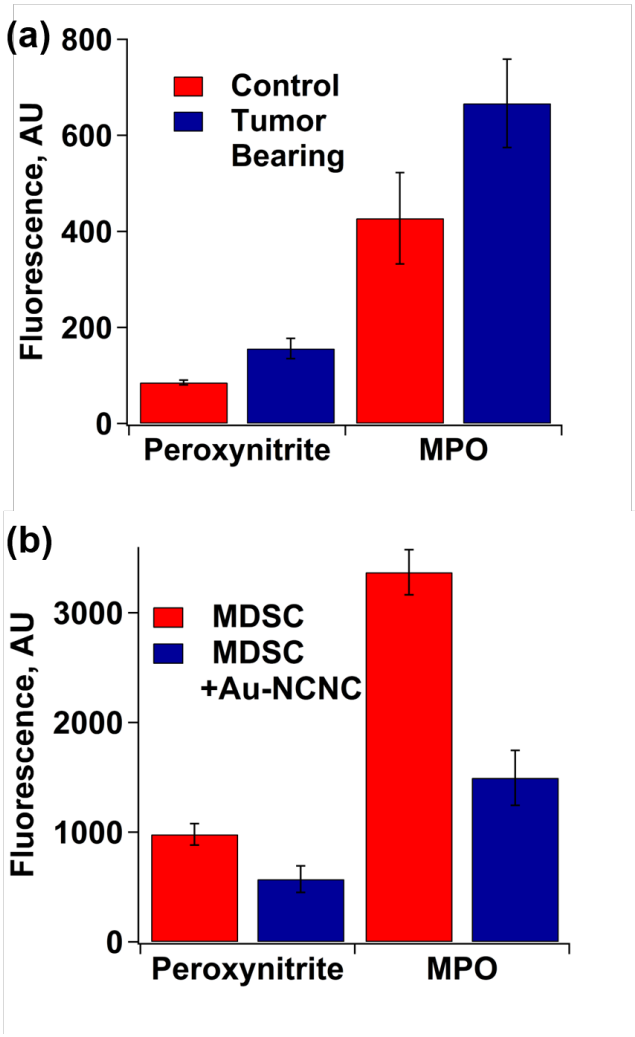

Figure 4-4 (a) MPO activity and peroxynitrite ($ONOO^-$) production in MDSC isolated from tumor-free (control, red) and tumor-bearing (blue) mice. (b) Activated MDSC can target Au-NCNC as reflected by decreased activity of MPO and expression of $ONOO^-$ after addition of NCNC (blue) as compared to control MDSC (red). Au-NCNC are oxidized by PMA-activated MDSC resulting in the decrease in the MPO and $ONOO^-$ responses. Reproduced from reference[196] with permission from The Royal Society of Chemistry.

We first proved that NCNC-delivered paclitaxel is not cytotoxic for cells by assessing MDSC apoptosis after coincubation with Au-NCNC as shown in Chapter 6 supporting information. No significant differences in the percentage of apoptotic (Annexin V+/PI-) cells were detected between control and tumor-associated MDSC treated with empty or paclitaxel-loaded Au-

NCNC ($p > 0.5$). Next, we revealed that Au-NCNC loaded with paclitaxel, but not empty Au-NCNC, blocked the ability of tumor-associated MDSC to suppress proliferation of preactivated T lymphocytes, as shown in Figure 4–5, which suggests that paclitaxel was effectively delivered to MDSC by Au-NCNC and affected their immunosuppressive activity, as expected. Furthermore, knowing that TGF-β produced by tumor-associated MDSC plays a role in inhibiting T cells, we showed that paclitaxel loaded Au-NCNC, but not empty Au-NCNC, significantly down-regulated expression of TGF-β in tumor-associated MDSC. As expected, no effects of empty Au-NCNC on control MDSC were observed. Finally, we tested whether paclitaxel loaded Au-NCNC can stimulate differentiation of tumor-associated MDSC into DC, because this property of MDSC has been reported to be lost in cancer. As shown in Figure 4-6, treatment of MDSC isolated from tumor-bearing mice with paclitaxel loaded Au-NCNC, but not empty Au-NCNC, increased appearance of CD11c+ DC up to 3-fold, suggesting that paclitaxel delivered by Au-NCNC up-regulates MDSC differentiation to DC. Altogether, these results demonstrate that paclitaxel can be loaded into Au-NCNC and effectively delivered to targeted cells, mainly MDSC.

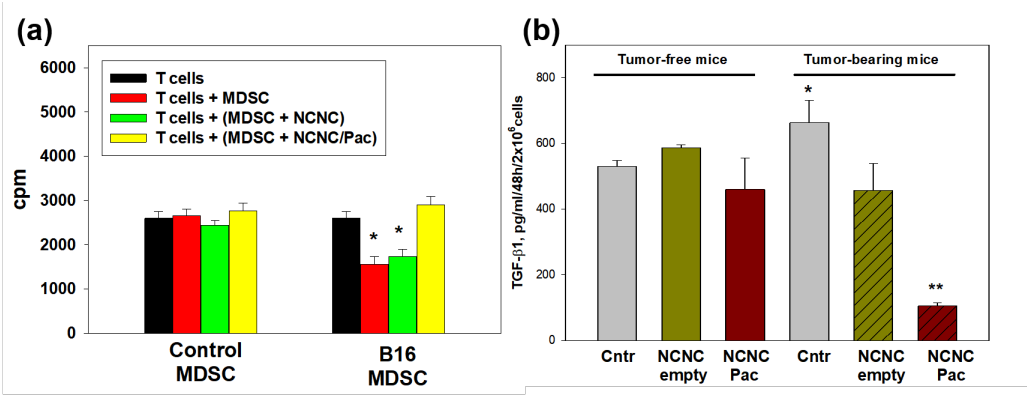

Figure 4-5 (a) Control and tumor-associated MDSC were incubated with empty and paclitaxel-loaded Au-NCNC for 48 hours, washed, counted, and coincubated with ConA preactivated and syngeneic splenic T lymphocytes. T cell proliferation was assessed by ^{3}H-thymidine incorporation and expressed as counts per minute (cpm) (*, $p < 0.05$ ANOVA), (b) Bone marrow MDSC were sorted from tumor-free mice and mice bearing B16 melanoma for 3 weeks, incubated with medium (control), empty Au-NCNC, and paclitaxel loaded Au-NCNC. TGF-β was measured by ELISA in cell-free supernatents (*, $p < 0.05$ vs. Cntr in tumor-free mice, **, $p < 0.05$ vs. all groups). Reproduced (adapted) with permission from reference.[167] Copyright 2014 American Chemical Society.

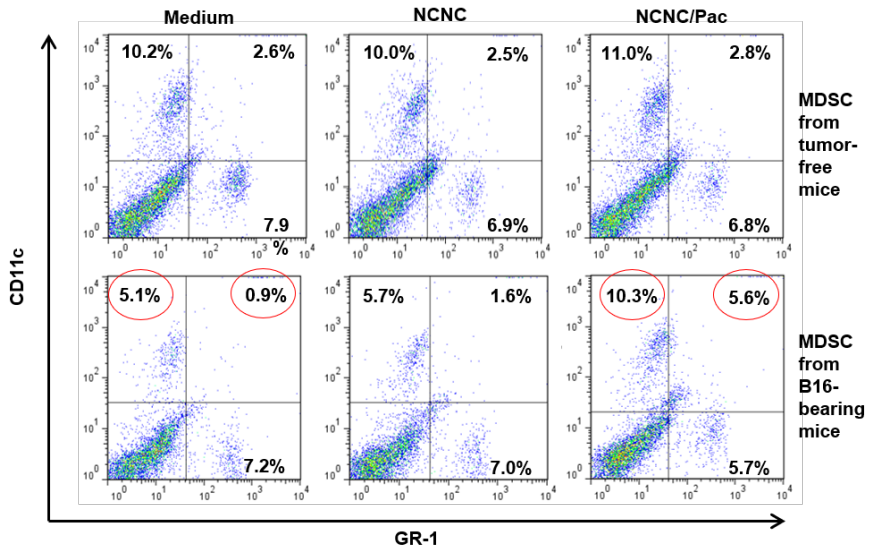

Figure 4-6 Paclitaxel loaded Au-NCNC up-regulates differentiation of tumor-associated MDSC into DC. Lung MDSC from tumor-free and B16-melanoma metastasis-bearing mice were cell sorted, incubated with empty and paclitaxel loaded Au-NCNC for 48 hours and appearance of CD11c+ DC was assessed by flow cytometry. Reproduced (adapted) with permission from reference.[167] Copyright 2014 American Chemical Society.

To determine whether paclitaxel-loaded Au-NCNC display unique drug delivery characteristics *in vivo*, we assessed tumor (melanoma) growth in syngeneic animals treated with saline, empty Au-NCNC, Au-NCNC loaded with paclitaxel, and free paclitaxel as described above. Prior reports have shown that systemic delivery of 1–5 mg/kg doses of paclitaxel in different tumor models can restore immune function *in vivo*.[210] However, the effect was observed only after multiple injections or in combination with other therapies. As the loaded amount of paclitaxel was found to be on average 36 µg, the total administered dosage of paclitaxel was 1.8 mg/kg. We administered one injection of the paclitaxel loaded Au-NCNC per mouse and measured the therapeutic effect over 3 weeks. Time-course of tumor growth in all groups of melanoma-bearing mice is shown in Figure 4–7. Control mice without Au-NCNC injection have a linear/exponential increase in tumor size over the course of more than two weeks, as expected.

Injection of empty Au-NCNC results in a slight decrease in the rate of tumor growth, which can be attributed to non-specific inflammation associated with systemic nanomaterial administration. Immune cells are characterized by the expression of oxidative enzymes and the expression of these enzymes increases in response to pro-inflammatory conditions.[216, 217] More specifically, the introduction of nanomaterials to biological systems has been shown to trigger such a pro-inflammatory response. Incubation of macrophages with MWNT was found to induce activity of COX-2 and iNOS which are responsible for the metabolism of arachidonic acid into prostaglandins and production of NO respectively which are both central to inflammatory response.[218] Shortening CNT has typically been seen as a way to decrease these effects; however the incorporation of structural and chemical defects after specific shortening techniques have been correlated with enhanced pro-inflammatory and pro-oxidative responses.[219] Therefore, the marginal decrease in tumor growth in response to empty Au-NCNC is most likely due to the activation of these pro-inflammatory machineries. Treatment with paclitaxel-loaded Au-NCNC results in significant inhibition of tumor growth in melanoma-bearing mice ($p < 0.05$, n = 3). The effect observed is more pronounced as compared to empty Au-NCNC indicating that the anti-tumor effect is not due to non-specific inflammation and must be due to the delivery of paclitaxel. Furthermore, ~25–30% of mice injected with paclitaxel-loaded Au-NCNC were found to be tumor-free on day 15. A single administration of free paclitaxel in tumor bearing mice did not significantly alter tumor growth. This confirms our early studies showing noncytotoxic doses of this chemotherapeutic agent (less than 20–30 mg/kg as a single injection) do not display a significant antitumor potential in the B16 melanoma model.[220-222] Thus, Au-NCNC based delivery of paclitaxel, unlike free paclitaxel results in significant inhibition of tumor growth *in vivo*. Injection of free paclitaxel affects a slight decrease in tumor growth between days 5 and 9. Decreased tumor growth was short-lived as

growth rates returned to similar values as the saline injection for the remainder of the *in vivo* trial. In comparison, delivery of paclitaxel by Au-NCNC resulted in prolonged effects over the entire time course of the *in vivo* experiment. This further illustrates a strong interaction of the paclitaxel with the interior cavity of the NCNC resulting in gradual release of the loaded cargo as opposed to a burst delivery of chemotherapeutic agent.

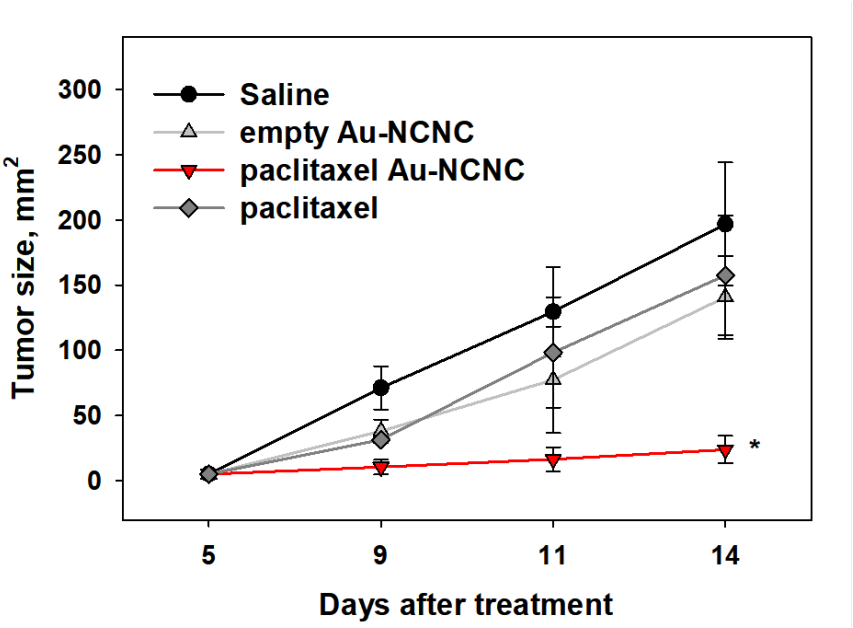

Figure 4-7 B16 melanoma cells were inoculated s.c. in syngeneic mice on day 0 and on day 6 animals were treated with saline (control), empty Au-NCNC, paclitaxel loaded Au-NCNC, and free paclitaxel. Tumor growth was measured as described in the experimental section. The results are shown as the mean ± SEM. *, $p < 0.01$ (ANOVA, n = 3 experiments). Reproduced from reference[196] with permission from The Royal Society of Chemistry.

While bio-distribution of paclitaxel has been previously studied through LC-MS, these experiments were performed at time points less than 24 hours.[223, 224] Therefore, the GNP corks, which act to effectively seal the NCNC openings, also provide a unique label for tracking the

distribution of Au-NCNC upon *in vivo* delivery. Gold atom concentrations were tracked through digestion of mouse tissue followed by quantification by ICP-MS. To determine homing and distribution of gold atoms in mice *in vivo*, heart, lung, liver, spleen, and tumor tissue were collected from treated animals at different time points. The tissue samples were then digested based upon previously published procedure.[211] Gold concentrations in each tissue sample were evaluated at days 6, 8 and 13 after injection of paclitaxel loaded and empty Au-NCNC. Comparisons between the biodistribution of empty Au-NCNC and paclitaxel loaded NCNC are not desirable due to the ability of paclitaxel to alter maturation and thus phagocytic activity and homing of myeloid phagocytes like macrophages, DC, MDSC, and neutrophils. In fact, paclitaxel is a known inhibitor of neutrophil function and longevity.[225] Research has shown that paclitaxel could stimulate maturation of DC, alter their endocytic activity and change DC motility.[226-228] Others have shown that nanodelivered paclitaxel changed the phagocytic properties of liver macrophages.[229] Therefore, we focus on the biodistribution of gold in response to i.v. injection of paclitaxel loaded Au-NCNC as shown in Figure 4–8. The complete ICP-MS data including gold bio-distribution of empty Au-NCNC are summarized in Chapter 6 supporting information.

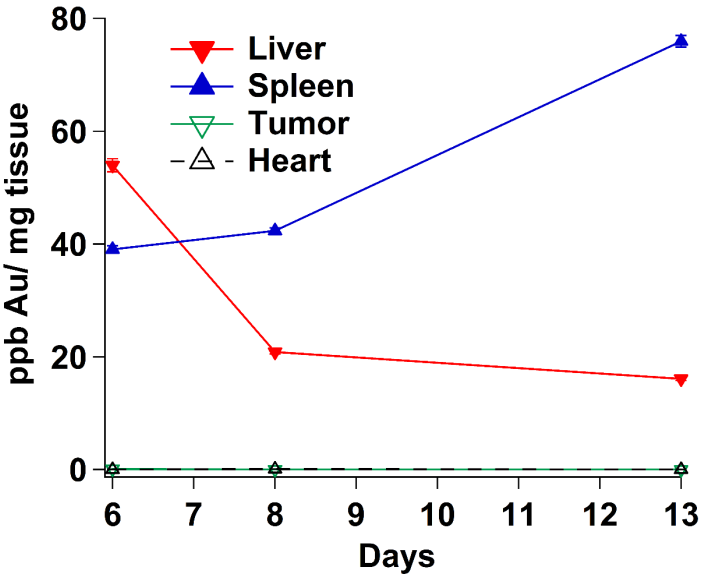

Figure 4-8 ICP-MS was used to detect gold atoms in different tissues 6, 8, and 13 days after i.v. injection of paclitaxel loaded Au-NCNC. The results were normalized per milligram of tissue. Each sample was run in triplicate with the average being reported and error bars representing the standard deviation of the triplicate measurements. Reproduced from reference[196] with permission from The Royal Society of Chemistry.

The initial bio-distribution of paclitaxel loaded Au-NCNC as determined by ICP-MS shows the most accumulation of gold within the liver, followed by the spleen and negligible accumulation within the heart and tumor. While long-term comparisons between empty and paclitaxel loaded Au-NCNC are undesirable, due to differences in phagocytic activity in response to delivered paclitaxel, initial biodistribution of gold in response to i.v. injection of empty Au-NCNC was found to be similar to paclitaxel loaded Au-NCNC. The bio-distribution of gold after i.v. injection of paclitaxel loaded Au-NCNC indicates a decrease in the amount of gold located within the liver while a simultaneous increase in the amount of gold located within the spleen over time. The temporal change in distribution can be attributed to the difference in bio-distribution between GNP and CNT. Previous reports have shown that introduction of CNT *in vivo* results in an initial accumulation within the liver.[230] Similar studies on the bio-distribution of GNP found

that the particles mainly accumulate in the spleen upon *in vivo* exposure.[211] We believe that the initial spike of gold atoms in the liver is due to GNP still being associated with NCNC and therefore following the normal bio-distribution of the CNT. After several days, the GNP have been detached from the nanotube surface by oxidation and proceed on their normal bio-distribution thus accumulating in the spleen. The amount of gold found within the heart is plotted as a control as GNP are not expected to reside within heart tissue for extended periods of time. ICP-MS analysis of gold bio-distribution also indicates that the gold does not reside within the tumor for extended periods of time. This illustrates that due to the length scale of Au-NCNC, they are not up-taken by the tumor microenvironment and therefore delivery of paclitaxel directly to the tumor is not expected. Instead, Au-NCNC are up-taken by circulating and lymphoid tissue MDSC where they are uncorked and paclitaxel is locally delivered. This represents a novel chemotherapeutic technique altering circulating and lymphoid tissue MDSC instead of targeting the tumor microenvironment.

Monitoring the levels of MDSC subsets in both lymphoid and non-lymphoid tissues across the time course of the experiment, by flow cytometry, was used to evaluate whether the antitumor activity of paclitaxel loaded Au-NCNC *in vivo* is associated with down-regulation of MDSC and potential correlation with gold distribution. Figure 4–9 (upper panels) shows that administration of paclitaxel loaded Au-NCNC was accompanied by a rapid and prolonged decrease of the percentage of intratumoral PMN-MDSC up to 4–5 fold ($p < 0.05$, n=2). Interestingly, no significant alterations of intratumoral M-MDSC were seen after Au-NCNC administration, which may be due to the differential sensitivity of intratumoral MDSC subsets to paclitaxel. Reports have shown that PMN-MDSC but not M-MDSC in the tumor milieu may differentiate into regDC and that paclitaxel might affect this pathway of myeloid regulatory cell interdifferentiation.[92]

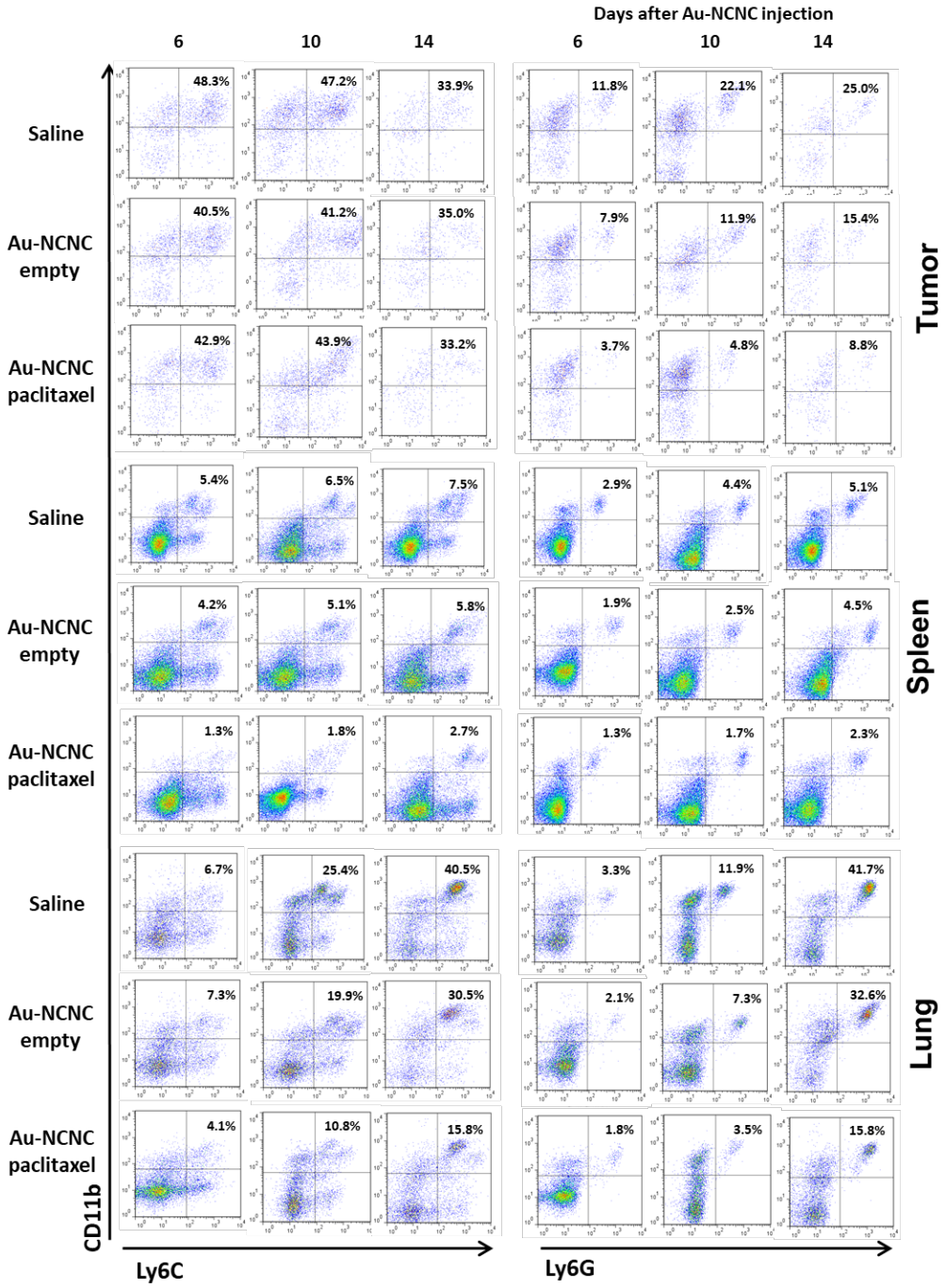

Figure 4-9 B16 melanoma-bearing mice were i.v. injected with saline, empty Au-NCNC and paclitaxel loaded Au-NCNC and tissues were harvested at different time points as shown. Representative flow cytometry results are shown for CD45 gated cell populations. The levels of monocytic CD11bLy6C^{high}Ly6G$^{low/neg}$ M-MDSC and polymorphonuclear CD11bLy6G^{high}Ly6C$^{low/neg}$ PMN-MDSC are shown. Two independent experiments revealed similar results. Reproduced from reference[196] with permission from The Royal Society of Chemistry.

We conducted a similar evaluation of both MDSC subsets in dynamics after intravenous injection of empty and paclitaxel loaded Au-NCNC in the spleen and lungs, the organs known for high tropism and homing of MDSC. Tumor-bearing mice receiving either saline or free paclitaxel served as controls. It is important to notice that the level of MDSC was determined within CD45+ cells, *i.e.* leukocytes: also known as leukocyte common antigen, CD45 is expressed on almost all hematopoietic cells except for mature erythrocytes.[231] This fact is documented by low levels of MDSC in the spleen, which are enriched with leukocytes. The results of these studies confirm that the treatment of melanoma-bearing mice with paclitaxel loaded Au-NCNC is accompanied by a decrease in MDSC in different lymphoid and non-lymphoid tissues, in conjunction with a decrease in the tumor mass. However, injection of free paclitaxel does not have the same effect as MDSC levels were found to be similar to those of mice injected with saline which can be seen in Chapter 6 supporting information. These data agree with our results suggesting that corked NCNC might be opened in different tissues where myeloid regulatory cells, in particular MDSC, are expected to accumulate during tumor growth and progression. Furthermore, both monocytic and polymorphonuclear MDSC were affected by NCNC delivered paclitaxel confirming the fact that in tumor-bearing hosts MDSC infiltrating the tumor bed are functionally different from MDSC homing in other tissues, including spleen, lymph nodes, bone marrow and non-lymphoid organs. Finally, no vital signs of toxicity or autoimmune processes in mice receiving i.v. Au-NCNC were observed up to 40–50 days after nanomaterial administration. Together, these results strongly support the feasibility of using Au-NCNC loaded with anti-cancer agents in diseases where marked accumulation and/or activation of myeloid regulatory cells is anticipated.

The results of this investigation illustrate several major advantages over analogous drug delivery systems. First, Au-NCNC do not require specific functionalization for targeting the tumor

microenvironment simplifying the production process. Second, the enzymatic opening mechanism is specific for the unique MDSC oxidizing environment resulting in minimal non-specific delivery. Finally, Au-NCNC does not need to be combined with additional therapies to halt tumor progression unlike analogous materials,[232] and does not require the use of paclitaxel derivatives and instead utilizes the unmodified molecule.[233]

4.4 Conclusions

The results presented demonstrate the usefulness of Au-NCNC for the delivery of paclitaxel in the context of cancer immunotherapy. Altering the GNP corking mechanism for *in vivo* applications had minimal effect on the physical and chemical properties of Au-NCNC. Upon intravenous injection Au-NCNC were found to distribute throughout the body and not specifically in the tumor microenvironment. Despite non-exclusive targeting delivery, paclitaxel was released from Au-NCNC and presumably affected the local populations of MDSC. The results provide proof of concept for not only the use of Au-NCNC as a unique immunotherapy but that targeting circulating and lymphoid tissue MDSC can result in a pronounced antitumor effect without specifically targeting the tumor microenvironment. Based on our earlier *in vitro* data showing that paclitaxel released from Au-NCNC in the presence of tumor-activated MDSC did not induce apoptosis of MDSC but augmented MDSC differentiation into DC,[167] a similar mechanism may also operate *in vivo*. Knowing the wide spectrum of immunomodulating properties of paclitaxel,[234] additional antitumor pathways induced by enzymatically degraded paclitaxel loaded corked NCNC can be suggested. Their evaluation, as well as systemic characterization of antitumor

potential of Au-NCNC loaded with different chemotherapeutic, targeted and immunotherapeutic compounds in different pre-clinical tumor models is timely and well justified.

4.5 Acknowledgement

This work at the University of Pittsburgh was supported by an NSF CAREER Award No. 0954345, NIH R01ES019304, NIH 2R01CA165065-06A1, NIH 5U19AI068021-14 and NIH R01Ca154369. Raman characterization was completed through the assistance of a ONR (N000141410765) grant. Special thanks to the Nanoscale Fabrication and Characterization Facility and the Department of Biological Sciences at the University of Pittsburgh for provision of access to the TEM and Raman instruments. Special thanks to Ashley Smith, Kathryn Johnston, and Daniel J. Bain for use and operation of the ICP-MS. Special thanks to Dr. Bhaskar Godugu for assistance with LC-MS method development.

5.0 Additional projects

5.1 Non-noble metal decoration of NCNC

As presented in Chapter 3, NCNC possess the ability to reduce noble metal salts at varying temperatures in order to produce NCNC decorated with nanoparticles. In Chapter 2, we explored how variation in the metal precursor can affect the electrocatalytic performance of NCNC towards the ORR with nickel based NCNC showing unique 4 electron reduction. External functionalization of NCNC with nickel, and other non-noble metals, may result in unique hybrid materials with electrocatalytic performance towards highly desirable reactions such as the ORR and carbon dioxide reduction. While we have shown that nickel-based materials may be of interest for the ORR, there is evidence that cobalt doped nanomaterials may possess enhanced electrocatalytic activity for carbon dioxide reduction.[235] Therefore, we aimed to reduce $NiCl_2$ and $CoCl_2$ salts on NCNC for potential applications in electrocatalytic reactions.

NCNC were incubated in either 0.385 mM $NiCl_2$ or $CoCl_2$ solutions for 2 hours at 75°C with no additional reducing agent added. The resulting material was collected and washed by centrifugation and subsequently imaged by TEM. Representative TEM images are shown in Figure 5–1 and the formation of sheets on the external surface of NCNC can be observed. As surface area has been known to improve electrocatalytic activity these materials may prove to be interesting catalysts for their respective reactions. To confirm the presence of the metal on the NCNC, XPS characterization was performed where the respective metals were both observed with each showing the formation of metal oxide and metal hydroxide species. These materials were both tested for their respective electrocatalytic reactions as shown in Figure 5–2. Ni decorated NCNC

did show potential for ORR electrocatalytic activity which is similar to the activity shown before for the NCNC[Ni] material. Likewise, Co decorated NCNC showed potential for carbon dioxide reduction as evidenced by the increase in overall current compared to a nitrogen purged solvent. Further characterization of these materials was not performed however, product analysis and optimization of the decoration procedure could result in interesting electrocatalysts.

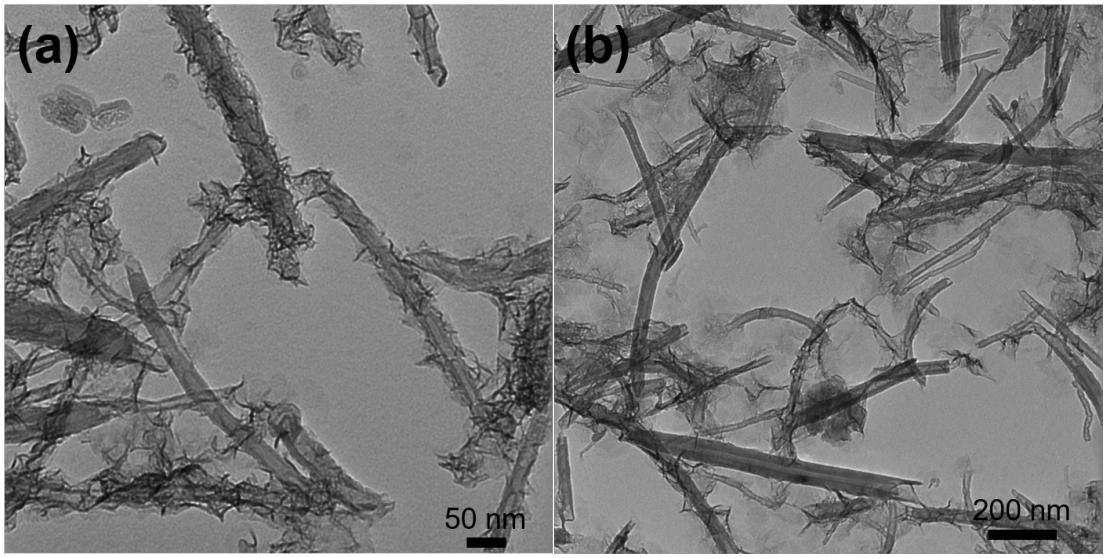

Figure 5-1 Transmission electron microscopy images of separated NCNC incubated with (a) $NiCl_2$ and (b) $CoCl_2$.

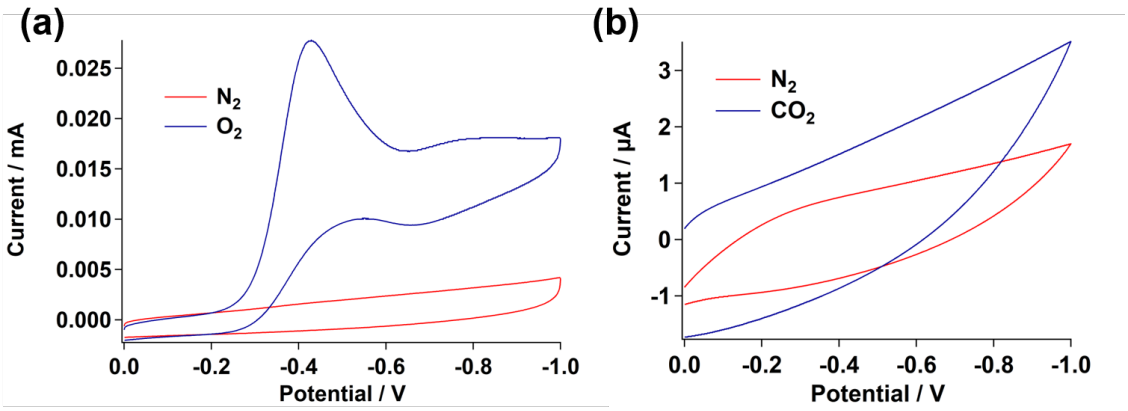

Figure 5-2 Cyclic voltammetry of (a) Ni decorated NCNC in 0.1 M KOH in the presence and absence of O_2, and (b) Co decorated NCNC in DMF in the presence and absence of CO_2.

6.0 Supporting information

This Chapter contains supporting information related to the optimization of NCNC synthesis, separation, GNP decoration, and the loading and delivery of cargo.

Changes in the chemical and physical properties of Au-NCNC were monitored due to modifications in the corking procedure for *in vivo* delivery of paclitaxel. We investigated the physical structure of Au-NCNC prepared in (i) nanopure water, (ii) buffer, (iii) buffer and ethanol, and finally (iv) buffer, ethanol, and paclitaxel corking conditions. TEM revealed no significant differences in the physical structure of Au-NCNC due to the altered corking conditions, as shown in Figure 6-1. However, when ethanol is added to the corking solution, both alone or in combination with paclitaxel, free GNP formation increased as compared to nanopure water and buffer corking conditions. Despite the increase in free GNP formation, a similar percentage (30–40%) of NCNC were found to be completely corked.

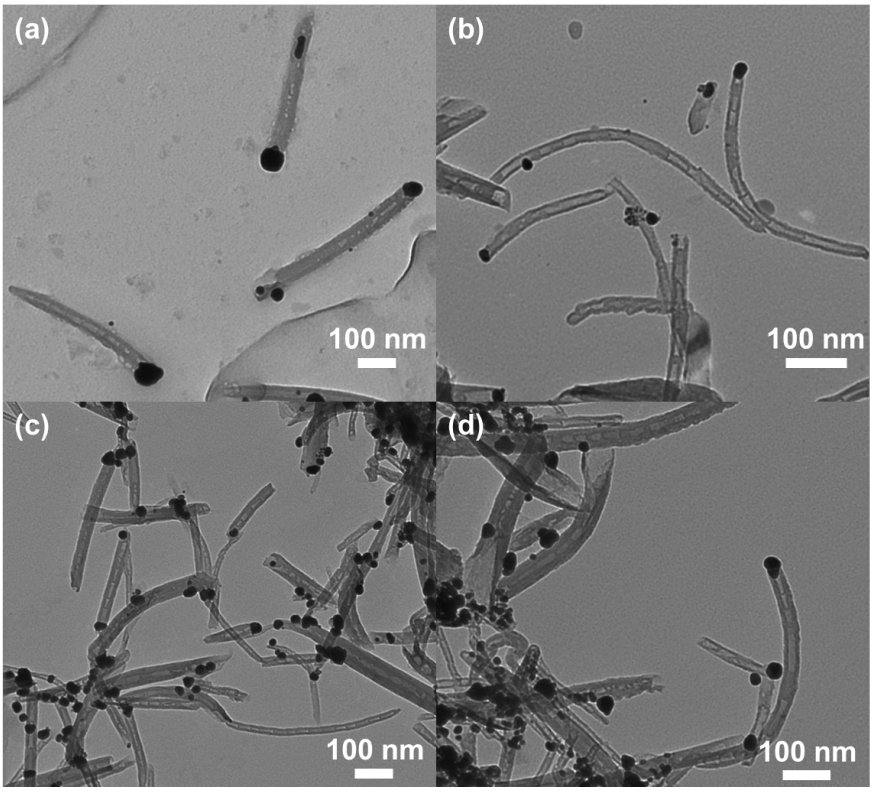

Figure 6-1 Representative transmission electron microscopy images of Au-NCNC synthesized in (a) nanopure water, (b) 1× phosphate buffer, (c) 1× phosphate buffer and ethanol, and (d) 1× phosphate buffer and paclitaxel suspended in ethanol. Reproduced from reference[196] with permission from The Royal Society of Chemistry.

The chemical structure of the Au-NCNC did not vary significantly under the several modified corking conditions. Raman spectra are shown in Figure 6-2 illustrate similar enhancement in the defect peak (D peak, ~1320 cm^{-1}) and graphitic peak (G peak, ~1560 cm^{-1}) of the NCNC, which is due to the presence of the GNP in each of the Au-NCNC samples. In addition, nearly identical D/G ratios were detected. Similar Raman intensities confirm that coordination of the NCNC with GNP is roughly equivalent. The comparable D/G ratios indicate that changes in the corking conditions do not result in additional defects being incurred by the NCNC structure. Furthermore, survey XPS characteristics do not show any substantial changes in elemental composition of NCNC as illustrated in Figure 6-3 and Table 6-1.

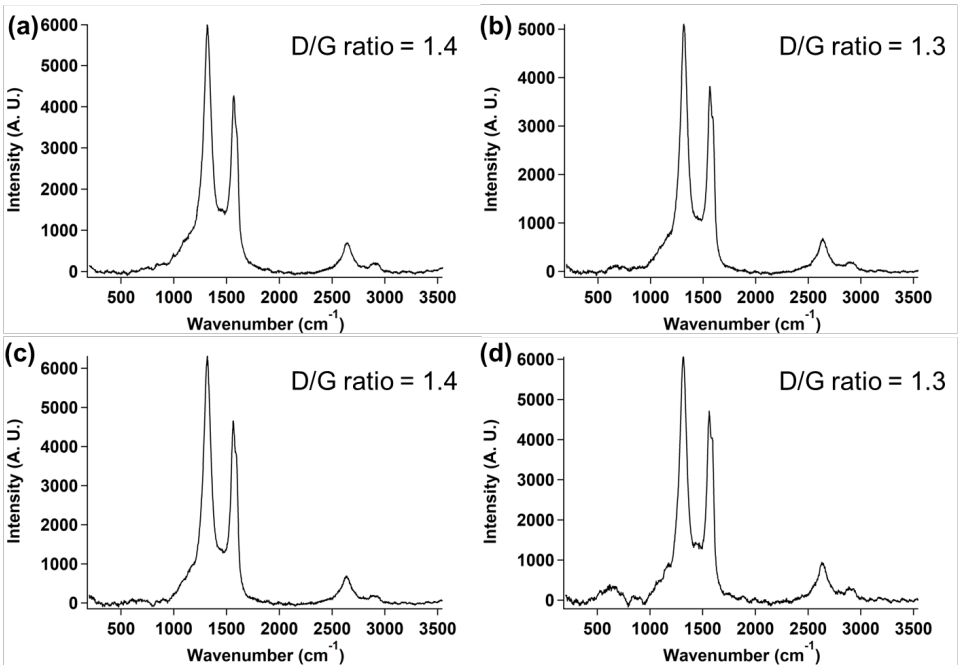

Figure 6-2 Raman characterization with inset D/G ratios for Au-NCNC synthesized in (a) nanopure water, (b) 1× phosphate buffer, (c) 1× phosphate buffer and ethanol, and (d) 1× phosphate buffer and paclitaxel suspended in ethanol. Reproduced from reference[196] with permission from The Royal Society of Chemistry.

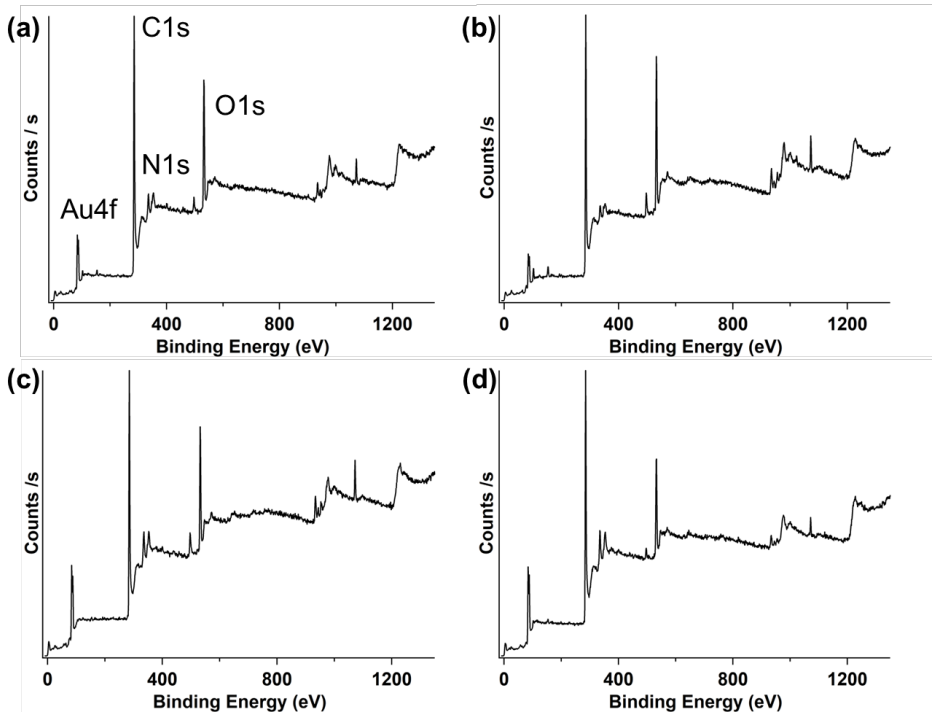

Figure 6-3 Survey X-ray photoelectron spectroscopy characterization of Au-NCNC synthesized in (a) nanopure water, (b) 1× phosphate buffer, (c) 1× phosphate buffer and ethanol, and (d) 1× phosphate buffer and paclitaxel suspended in ethanol. Reproduced from reference[196] with permission from The Royal Society of Chemistry.

Table 6-1 Atomic percent of each Au-NCNC sample as determined by survey XPS

Element	Normal	Buffer	Ethanol	Taxol
C1s	79.07%	77.54%	79.15%	82.42%
O1s	18.03%	20.41%	17.09%	14.94%
N1s	1.84%	1.36%	2.26%	1.05%
Au4f	1.06%	0.69%	1.50%	1.60%

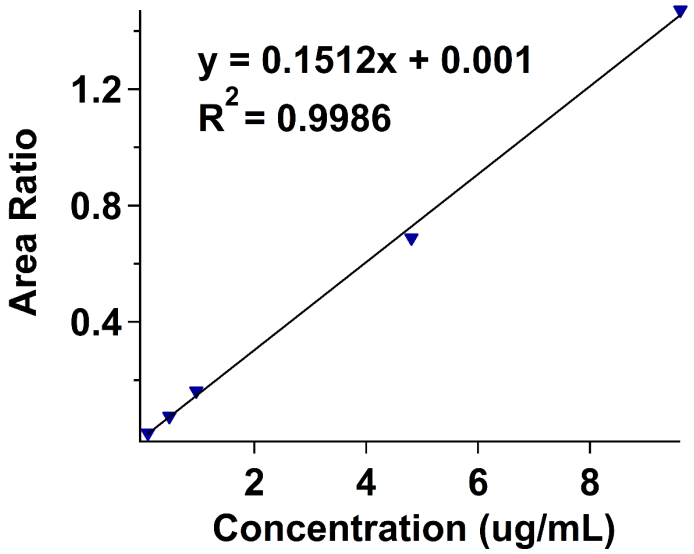

Figure 6-4 Calibration plot for the quantification of pacltiaxel. Reproduced from reference[196] with permission from The Royal Society of Chemistry.

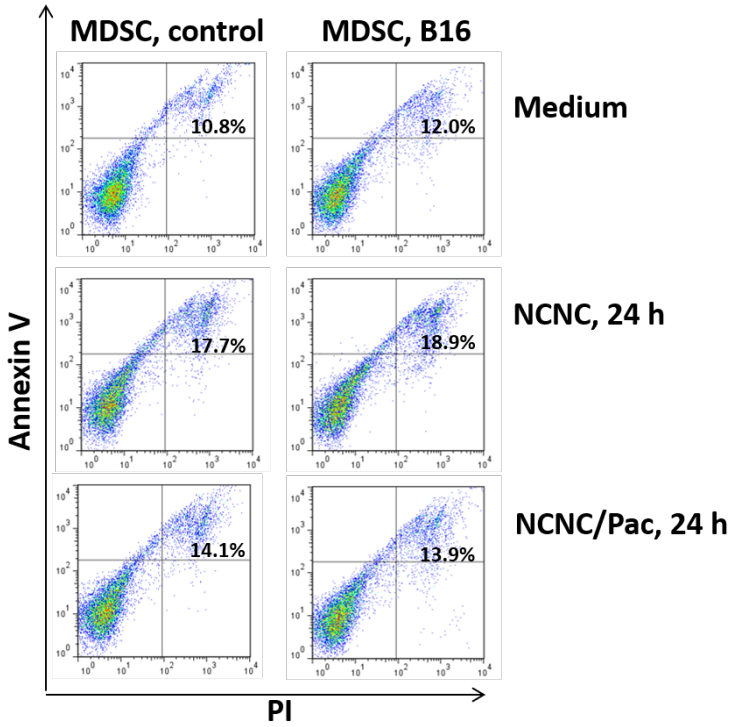

Figure 6-5 Au-NCNC delivered paclitaxel is not cytotoxic for control and tumor-associated MDSC. Intact and tumor-activated MDSC were treated with empty and paclitaxel loaded Au-NCNC for 24 hours, washed and their apoptosis was determined after Annexin V and PI staining by flow cytometry. Reprinted (adapted) with permission from reference.[167] Copyright 2014 American Chemical Society.

Table 6-2 Bio-distribution of gold atoms as detected by ICP-MS

	ppb Au/mg tissue		
Day 6	**B16 melanoma (control)**	**Empty Au-NCNC**	**Paclitaxel Au-NCNC**
Heart	0.005 ± 0.000	0.096 ± 0.003	0.062 ± 0.002
Liver	0.035 ± 0.000	18.260 ± 1.314	53.962 ± 1.150
Lung	0.014 ± 0.000	12.145 ± 0.141	6.384 ± 0.101
Spleen	0.033 ± 0.001	16.828 ± 0.887	39.069 ± 0.645
Tumor	0.009 ± 0.001	0.316 ± 0.013	0.138 ± 0.006
Day 8	**B16 melanoma (control)**	**Empty Au-NCNC**	**Paclitaxel Au-NCNC**
Heart	0.007 ± 0.000	0.108 ± 0.001	0.145 ± 0.010
Liver	0.006 ± 0.000	81.204 ± 1.622	20.891 ± 0.363
Lung	0.010 ± 0.001	32.557 ± 0.620	0.892 ± 0.010
Spleen	0.013 ± 0.001	208.916 ± 2.561	42.387 ± 0.505
Tumor	0.006 ± 0.000	0.194 ± 0.009	0.066 ± 0.002
Day 13	**B16 melanoma (control)**	**Empty Au-NCNC**	**Paclitaxel Au-NCNC**
Heart	0.016 ± 0.008	0.055 ± 0.003	0.073 ± 0.003
Liver	0.007 ± 0.000	26.904 ± 0.134	16.118 ± 0.304
Lung	0.026 ± 0.000	63.950 ± 1.102	13.910 ± 0.329
Spleen	0.025 ± 0.001	123.912 ± 3.042	75.931 ± 1.034
Tumor	0.006 ± 0.001	0.068 ± 0.001	0.067 ± 0.003

Each sample was run in triplicate with the average of the triplicate measurements being reported ± the standard deviation of the measurements. The gold ppb concentration of each data point was normalized to the mass of the tissue sample.

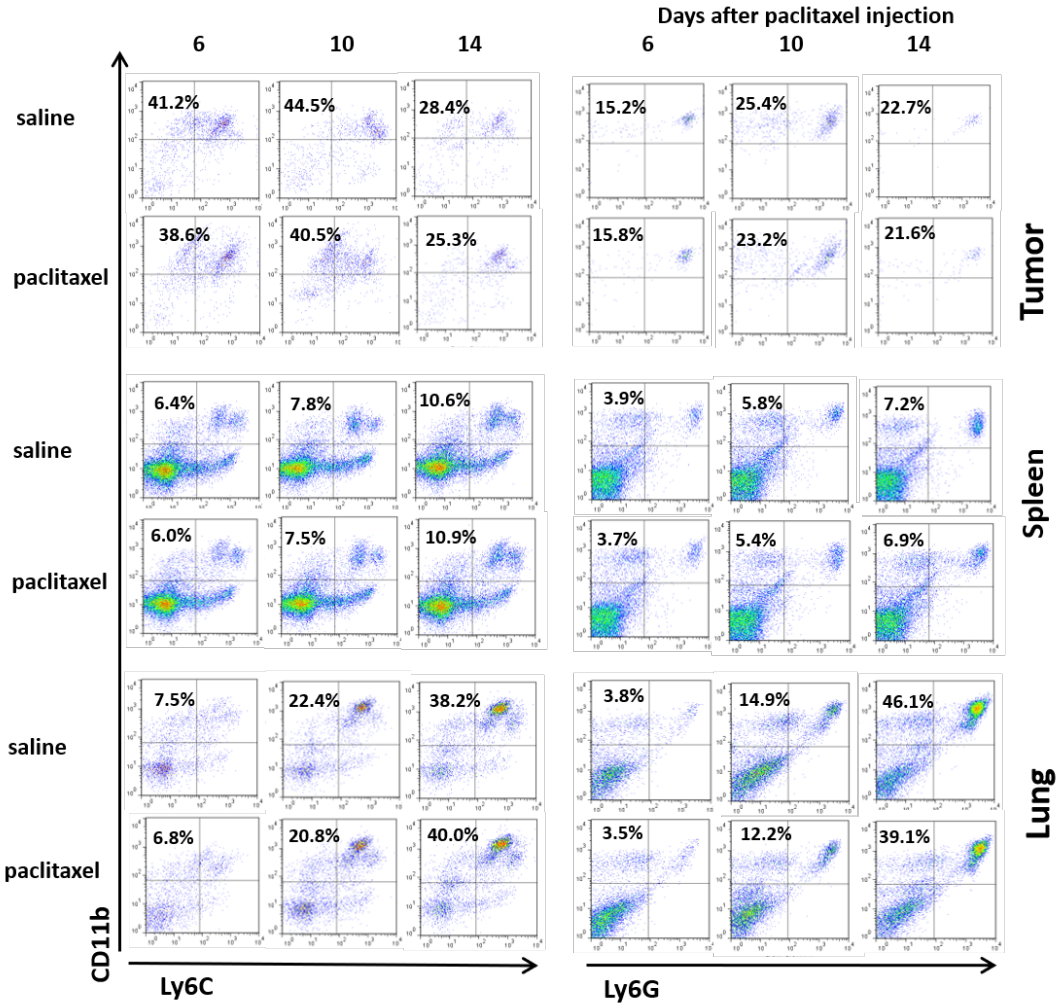

Figure 6-6 B16 melanoma-bearing mice were tail vein injected with saline and free paclitaxel, and tissues were harvested at different time points as shown. Representative flow cytometry results are shown for CD45 gated cell populations. The levels of monocytic CD11bLybC^{high}Ly6G$^{low/neg}$ M-MDSC and polymorphonuclear CD11bLy6G^{high}Ly6C$^{low/neg}$ PMN-MDSC are shown. Two independent experiments revealed similar results. Reproduced from reference[196] with permission from The Royal Society of Chemistry.

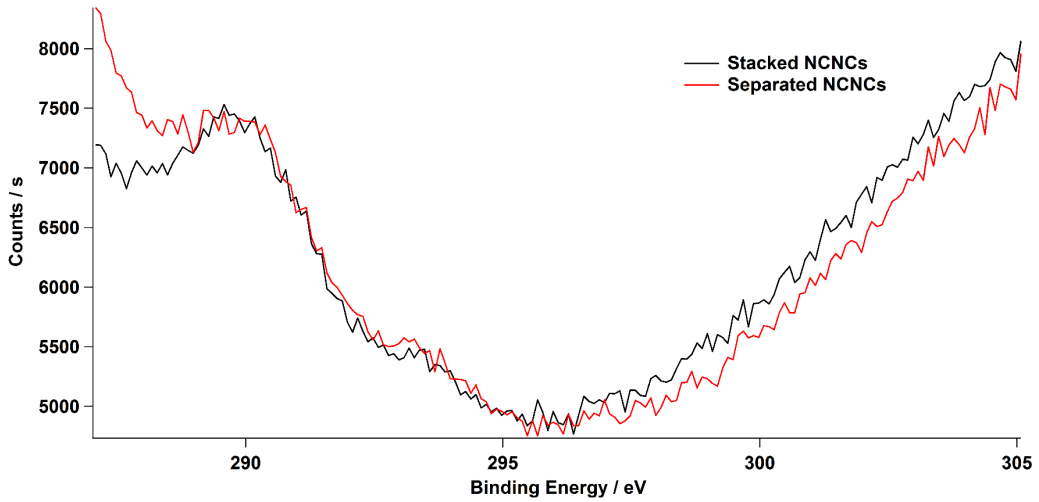

Figure 6-7 K2p high resolution X-ray photoelectron spectroscopy spectra for stacked NCNC (black) and separated NCNC (red) to show the absence of potassium from both samples. Reprinted (adapted) from reference.[101]

Appendix A

1. Bian, L.; Sorescu, D. C.; Chen, L.; White, D. L.; Burkert, S. C.; Khalifa, Y.; Zhang, Z.; Sejdic, E. Star, A. Machine Learning Identifications of the Sensing Descriptors Relevant in Molecular Interactions with Metal Nanoparticle-Decorated Nanotube Field-Effect Transistors *ACS Appl. Mater. Interfaces* **2019**, *11*(1), 1219–1227.
2. Ellis, J. E.; Zeng, Z.; Hwang, S. I.; Li, S.; Luo, T.; Burkert, S. C.; White, D. L.; Rosi, N. L.; Gassensmith, J. J.; Star, A. Growth of ZIF−8 on molecularly ordered 2−methylimidazole/single−walled carbon nanotubes to form highly porous, electrically conductive composites *Chem. Sci.* **2019**, *10*(3), 737–742.
3. Burkert, S. C.; Shurin, G. V.; White, D. L.; He, X.; Kapralov, A. A.; Kagan, V. E.; Shurin, M. R.; Star, A. Targeting myeloid regulators by paclitaxel-loaded enzymatically degradable nanocups *Nanoscale* **2018**, *10*(37), 17990−18000.
4. Peng, G.; Wu, S.; Peng, Q.; Burkert S. C.; Du, R.; Yu, C.; Star, A. Synthesis of TiO2 Nanospindles Supported Pt Nanodots for Oxygen Reduction Reactions *Advances in New and Renewable Energy* **2018**, *6*, 163–168.
5. Michael, Z. P.; Shao, W.-T.; Sorescu, D. C.; Euler, R.; Burkert, S. C.; Star, A. Probing Biomolecular Interactions with Gold Nanoparticle-Decorated Single-Walled Carbon Nanotubes *J. Phys. Chem. C* **2017**, *121*(38), 20813–20820.
6. Ellis, J. E.; Sorescu, D. C.; Burkert, S. C.; White, D. L.; Star, A. Uncondensed Graphitic Carbon Nitride on Reduced Graphene Oxide for Oxygen Sensing via a Photoredox Mechanism *ACS Appl. Mater. Interfaces* **2017**, *9*(32), 27142–27151.

7. Vlasova I. I.; Kapralov, A. A.; Michael, Z. P.; Burkert, S. C.; Shurin, M. R.; Star, A.; Shvedova, A. A.; Kagan, V. F. Enzymatic Oxidative Biodegradation of Nanoparticles: Mechanisms, Significance and Applications *Toxicol. Appl. Pharm*. **2016**, *299*, 58–69.

8. Bhattacharya, K.; Mukherjee, S. P.; Gallud, A.; Burkert, S. C.; Bistarelli, S.; Bellucci, S.; Bottini, M.; Star, A.; Fadeel, B.; Biological Interactions of Carbon-Based Nanomaterials: From Coronation to Degradation *Nanomed. – Nanotechnol*. **2016**, *12*(2), 333–351.

9. Burkert, S. C.; Star, A. Corking Nitrogen-Doped Carbon Nanotube Cups with Gold Nanoparticles for Biodegradable Drug Delivery Applications *Curr. Protoc. Chem. Biol.* **2015**, *7*(4), 249–262.

10. Dong, H.; Zhao, Y.; Tang, Y.; Burkert, S. C.; Star, A. Oxidative Unzipping of Stacked Nitrogen-Doped Carbon Nanotube Cups *ACS Appl. Mater. Interfaces* **2015**, *7*(20), 10734–10741

11. Zhao, Y.; Burkert, S. C.; Tang, Y.; Sorescu, D. C.; Kapralov, A. A.; Shurin, G. V.; Shurin, M. R.; Kagan, V. E.; Star, A. Nano-Gold Corking and Enzymatic Uncorking of Carbon Nanotube Cups *J. Am. Chem. Soc*. **2015**, *137*(2), 675–684

12. Tang, Y.; Zhao, Y.; Burkert, S. C.; Ding, M.; Ellis, J. E.; Star, A. Efficient Separation of Nitrogen-Doped Carbon Nanotube Cups *Carbon* **2014**, *80*, 583–590.

13. Tang, Y.; Burkert, S. C.; Zhao, Y.; Saidi, W. A.; Star, A. The Effect of Metal Catalyst on the Electrocatalytic Activity of Nitrogen-Doped Carbon Nanotubes *J. Phys. Chem. C* **2013**, *117*(48), 25213–25221

Bibliography

1. *Springer Handbook of Nanotechnology*, Springer, Germany, 4th edn., 2017.
2. M. Brust and C. J. Kiely, *Colloids Surf. A: Physicochem. Eng. Asp.*, 2002, **202**, 175-186.
3. M.-C. Daniel and D. Astruc, *Chem. Rev.*, 2004, **104**, 293-346.
4. G. Cao, *Nanostructures and Nanomaterials Synthesis, Properties, and Applications*, Imperial College Press, London, 2004.
5. M. A. Gatoo, S. Naseem, M. Y. Arfat, A. M. Dar, K. Qasim and S. Zubair, *Biomed Res. Int.*, 2014, 498420.
6. V. E. Kagan, N. V. Konduru, W. Feng, B. L. Allen, J. Conroy, Y. Volkov, I. I. Vlasova, N. A. Belikova, N. Yanamala, A. Kapralov, Y. Y. Tyurina, J. Shi, E. R. Kisin, A. R. Murray, J. Franks, D. Stolz, P. Gou, J. Klein-Seetharaman, B. Fadeel, A. Star and A. A. Shvedova, *Nat. Nanotechnol.*, 2010, **5**, 354-359.
7. A. A. Shvedova, E. R. Kisin, D. Porter, P. Schulte, V. E. Kagan, B. Fadeel and V. Castranova, *Pharmacol. Ther.*, 2009, **121**, 192-204.
8. K. Bhattacharya, S. P. Mukherjee, A. Gallud, S. C. Burkert, S. Bistarelli, S. Bellucci, M. Bottini, A. Star and B. Fadeel, *Nanomedicine: NBM*, 2016, **12**, 333-351.
9. B. Fadeel, *J. Intern. Med.*, 2013, **274**, 578-580.
10. R. Langer and R. Weissleder, *JAMA*, 2015, **313**, 135-136.
11. S. Nasir, M. Z. Hussein, Z. Zainal and N. A. Yusof, *Materials*, 2018, **11**, 295.
12. V. N. Mochalin, O. Shenderova, D. Ho and Y. Gogotsi, *Nat. Nanotechnol.*, 2012, **7**, 11-23.
13. R. Arjmandi, A. Hassan, N. Othman and Z. Mohamad, *Carbon-Based Polymer Nanocomposites for Environmental and Energy Applications*, John Fedor, 2018.
14. H. W. Kroto, J. R. Heath, S. C. O'Brien, R. F. Curl and R. E. Smalley, *Nature*, 1985, **318**, 162-163.
15. S. Iijima, *Nature*, 1991, **354**, 56-58.
16. M. Monthioux and V. L. Kuznetsov, *Carbon*, 2006, **44**, 1621-1623.
17. S. M. Bachilo, M. S. Strano, C. Kittrell, R. H. Hauge, R. E. Smalley and R. B. Weisman, *Science*, 2002, **298**, 2361-2366.

18. K. S. Novoselov, A. K. Geim, S. V. Morozov, D. Jiang, Y. Zhang, S. V. Dubonos, G. I. V and A. A. Firsov, *Science*, 2004, **306**, 666-669.

19. K. S. Novoselov, V. I. Fal'ko, L. Colombo, P. R. Gellert, M. G. Schwab and K. Kim, *Nature*, 2012, **490**, 192-200.

20. A. C. Ferrari, F. Bonaccorso, V. Fal'ko, K. S. Novoselov, S. Roche, P. Boggild, S. Borini, F. H. L. Koppens, V. Palermo, N. Pugno, J. A. Garrido, R. Sordan, A. Bianco, L. Ballerini, M. Prato, E. Lidorikis, J. Kivioja, C. Marinelli, T. Ryhanen, A. Morpurgo, J. N. Coleman, V. Nicolosi, L. Colombo, A. Fert, M. Garcia-Hernandez, A. Bachtold, G. F. Schneider, F. Guinea, C. Dekker, M. Barbone, Z. Sun, C. Galiotis, A. N. Grigorenko, G. Konstantatos, A. Kis, M. Katsnelson, L. Vandersypen, A. Loiseau, V. Morandi, D. Neumaier, E. Treossi, V. Pellegrini, M. Polini, A. Trediucci, G. M. Williams, B. H. Hong, J.-H. Ahn, J. M. Kim, H. Zirath, B. J. v. Wees, H. v. d. Zant, L. Occhipinti, A. D. Matteo, I. A. Kinloch, T. Seyller, E. Quesnel, Z. Feng, K. Teo, N. Rupesinghe, P. Hakonen, S. R. T. Neil, Q. T. T. Lofwander and J. Kinaret, *Nanoscale*, 2015, **7**, 4598-4810.

21. N. F. Atta, A. Galal and E. H. El-Ads, *Biosensors - Micro and Nanoscale Applications*, 2015.

22. K. Kostarelos, L. Lacerda, G. Pastorin, W. Wu, S. Wieckowski, J. Luangsivilay, S. Godefroy, D. Pantarotto, J.-P. Briand, S. Muller, M. Prato and A. Bianco, *Nat. Nanotechnol.*, 2007, **2**, 108-113.

23. D. Chen, C. A. Dougherty, K. Zhu and H. Hong, *J. Control. Release*, 2015, **210**, 230-245.

24. W. Fan, L. Zhang and T. Liu, *Graphene-Carbon Nanotube Hybrids for Energy and Environmental Applciations*, Springer, Singapore, 2016.

25. A. A. Bhirde, V. Patel, J. Gavard, G. Zhang, A. A. Sousa, A. Masedunskas, R. D. Leapman, R. Weiger, J. S. Gutkind and J. F. Rushling, *ACS Nano*, 2009, **3**, 307-316.

26. R. Singh, D. Pantarotto, L. Lacerda, G. Pastorin, C. Klumpp, M. Prato, A. Bianco and K. Kostarelos, *Proc. Natl. Acad. Sci. U.S.A.*, 2006, **103**, 3357-3362.

27. K. T. Al-Jamal, A. Nunes, L. Methven, H. Ali-Boucetta, S. Li, F. Toma, M. A. Herrero, W. T. Al-Jamal, H. M. M. t. Eikelder, J. Foster, S. Mather, M. Prato, A. Bianco and K. Kostarelos, *Angew. Chem. Int. Ed. Engl.*, 2012, **51**, 6389-6393.

28. A. Thess, R. Lee, P. Nikolaev, H. Dai, J. Robert, C. Xu, Y. H. Lee, S. G. Kim, A. G. Rinzler, D. T. Colbert, G. E. Scuseria, D. Tomanek, J. E. Fischer and R. E. Smalley, *Science*, 1996, **273**, 483-487.

29. P. C. Eklund, B. K. Pradhan, U. J. Kim, Q. Xiong, J. E. Fischer, A. D. Friedman, B. C. Holloway, K. Jordan and M. W. Smith, *Nano Lett.*, 2002, **2**, 561-566.

30. T. Guo, P. Nikolaev, A. Thess, D. T. Colbert and R. E. Smalley, *Chem. Phys. Lett.*, 1995, **243**, 49-54.

31. C. M. Lieber and C.-C. Chen, *Solid State Physics*, 1994, **48**, 109-148.

32. V. N. Bezmelnitsin, A. V. Eletskii, N. G. Schepetov, A. G. Avent and R. Taylor, *J. Chem. Soc., Perkin Trans. 2*, 1997, **0**, 683-686.

33. Y. M. Manawi, Ihsanullah, A. Samara, T. Al-Ansari and M. A. Atieh, *Materials (Basel)*, 2018, **11**, 822.

34. M. U. Zahid, E. Pervaiz, A. Hussain, M. I. Shahzad and M. B. K. Niazi, *Mater. Res. Express*, 2018, **5**, 052002.

35. P. H. Matter, E. Wang, M. Arias, E. J. Biddinger and U. S. Ozkan, *J. Phys. Chem. B*, 2006, **110**, 18374-18384.

36. S. v. Dommele, A. Romero-Izquirdo, R. Brydson, K. P. d. Jong and J. H. Bitter, *Carbon*, 2008, **46**, 138-148.

37. C. H. See and A. T. Harris, *Ind. Eng. Chem. Res.*, 2007, **46**, 997-1012.

38. H. Kathyayini, N. Nagaraju, A. Fonseca and J. B. Nagy, *J. Mol. Catal. A*, 2004, **223**, 129-136.

39. R. T. K. Baker, P. S. Harris, R. B. Thomas and R. J. White, *J. Catal.*, 1973, **30**, 86-95.

40. R. T. K. Baker, *Carbon*, 1989, **27**, 315-323.

41. Y. Ma, L. Sun, W. Huang, L. Zhang, J. Zhao, Q. Fan and W. Huang, *J. Phys. Chem. C*, 2011, **115**, 24592-24597.

42. Y. Tang, B. L. Allen, D. R. Kauffman and A. Star, *J. Am. Chem. Soc.*, 2009, **131**, 13200-13201.

43. K. Gong, F. Du, Z. Xia, M. Durstock and L. Dai, *Science*, 2009, **323**, 760-764.

44. Y. Li, W. Zhou, H. Wang, L. Xie, Y. Liang, F. Wei, J.-C. Idrobo, S. J. Pennycook and H. Dai, *Nat. Nanotechnol.*, 2012, **7**, 394-400.

45. T. Schilling, A. Okunola, J. Masa, W. Schuhmann and M. Bron, *Electrochim. Acta*, 2010, **55**, 7597-7602.

46. X. Wang, X. Li, L. Zhang, Y. Yoon, P. K. Weber, H. Wang, J. Guo and H. Dai, *Science*, 2009, **324**, 768-771.

47. B. L. Allen, P. D. Kichambare and A. Star, *ACS Nano*, 2008, **2**, 1914-1920.

48. M. L. Zhao, D. J. Li, L. Yuan, Y. C. Yue, H. Liu and X. Sun, *Carbon*, 2011, **49**, 3125-3133.

49. X. Ma and E. G. Wang, *Appl. Phys. Lett.*, 2000, **77**, 4136-4138.

50. Y. Zhao, B. L. Allen and A. Star, *J. Phys. Chem. A*, 2011, **115**, 9536-9544.

51. Y. Zhao, Y. Tang, Y. Chen and A. Star, *ACS Nano*, 2012, **6**, 6912-6921.

52. J. C. Carrero-Sanchez, A. L. Elias, R. Mancilla, G. Arrellin, H. Terrones, J. P. Laclette and M. Terrones, *Nano Lett.*, 2006, **6**, 1609-1616.

53. E. C. Dreaden, A. M. Alkilany, X. Huang, C. J. Murphy and M. A. El-Sayed, *Chem. Soc. Rev.*, 2012, **41**, 2740-2779.

54. L. A. Dykman and N. G. Khlebtsov, *Acta Naturae*, 2011, **3**, 34-55.

55. M. Grzelczak, J. Perez-Juste, P. Mulvaney and L. M. Liz-Marzan, *Chem. Soc. Rev.*, 2008, **37**, 1783-1791.

56. R. Jin, C. Zeng, M. Zhou and Y. Chen, *Chem. Rev.*, 2016, **116**, 10346-10413.

57. C. R. Martin, *Adv. Mater.*, 1991, **3**, 457-459.

58. J. E. Millstone, S. J. Hurst, G. S. Metraux, J. I. Cutler and C. A. Mirkin, *Small*, 2009, **5**, 646-664.

59. J. Turkevich, P. C. Stevenson and J. Hillier, *Discuss. Faraday Soc.*, 1951, **11**, 55-75.

60. F. Kettermann, A. Birnbaum, S. Witte, M. Wuithschick, N. Pinna, R. Kraehnert, K. Rademann and J. Polte, *Chem. Mater.*, 2016, **28**, 4072-4081.

61. M. Wuithschick, A. Birnbaum, S. Witte, M. Sztucki, U. Vainio, N. Pinna, K. Rademann, F. Emmerling, R. Kraehnert and J. Polte, *ACS Nano*, 2015, **9**, 7052-7071.

62. S. R. Ahmed, J. Kim, T. Suzuki, J. Lee and E. Y. Park, *Biosensors and Bioelectronics*, 2016, **85**, 503-508.

63. M. Ding, D. C. Sorescu, G. P. Kotchey and A. Star, *J. Am. Chem. Soc.*, 2012, **134**, 3472-3479.

64. B.-S. Kong, J. Geng and H.-T. Jung, *Chem. Commun.*, 2009, **0**, 2174-2176.

65. W. Xin, J. Severino, I. M. D. Rosa, D. Yu, J. Mckay, P. Ye, X. Yin, J.-M. Yang, L. Carlson and S. Kodambaka, *Nano Lett.*, 2018, **18**, 1875-1881.

66. J. Wang, X. Dong, R. Xu, S. Li, P. Chen and M. B. Chan-Park, *Nanoscale*, 2012, **4**, 3055-3059.

67. J. E. Millstone, W. Wei, M. R. Jones, H. Yoo and C. A. Mirkin, *Nano Lett.*, 2008, **8**, 2526-2529.

68. C. Zong, M. Xu, L.-J. Xu, T. Wei, X. Ma, X.-S. Zheng, R. Hu and B. Ren, *Chem. Rev.*, 2018, **118**, 4946-4980.

69. S. Nie and S. R. Emory, *Science*, 1997, **275**, 1102-1106.

70. E. J. Blackie, E. C. L. Ru and P. G. Etchegoin, *J. Am. Chem. Soc.*, 2009, **131**, 14466-14472.

71. F. M. P. Tonelli, V. A. M. Goulart, K. N. Gomes, M. S. Ladeira, A. K. Santos, E. Lorencon, L. O. Ladeira and R. R. Resende, *Nanomedicine*, 2015, **10**, 2423-2450.

72. A. Kunzmann, B. Andersson, T. Thurnherr, H. Krug, A. Scheynius and B. Fadeel, *Biochim. Biophys. Acta*, 2011, **1810**, 361-373.

73. N. Kamaly, Z. Xiao, P. M. Valencia, A. F. Radovic-Moreno and O. C. Farokhzad, *Chem. Soc. Rev.*, 2012, **41**, 2971-3010.

74. G. P. Kotchey, Y. Zhao, V. E. Kagan and A. Star, *Adv. Drug Deliv. Rev.*, 2013, **65**, 1921-1932.

75. K. Bhattacharya, F. T. Andon, R. El-Sayed and B. Fadeel, *Adv. Drug Deliv. Rev.*, 2013, **65**, 2087-2097.

76. K. Bhattacharya, R. El-Sayed, F. T. Andon, S. P. Mukherjee, J. Gregory, H. Li, Y. Zhao, W. Seo, A. Fornara, B. Brandner, M. S. Toprak, K. Leifer, A. Star and B. Fadeel, *Carbon*, 2015, **91**, 506-517.

77. B. L. Allen, G. P. Kotchey, Y. Chen, N. V. K. Yanamala, J. Klein-Seetharaman, V. E. Kagan and A. Star, *J. Am. Chem. Soc.*, 2009, **131**, 17194-17205.

78. V. E. Kagan, A. A. Kapralov, C. M. S. Croix, S. C. Watkins, E. R. Kisin, G. P. Kotchey, K. Balasubramanian, I. I. Vlasova, J. Yu, K. Kim, W. Seo, R. K. Mallampalli, A. Star and A. A. Shvedova, *ACS Nano*, 2014, **8**, 5610-5621.

79. K. Saika and T. Sobue, *Gan To Kagaku Ryoho*, 2013, **40**, 2475-2480.

80. D. Marvel and D. I. Gabrilovich, *J. Clin. Invest.*, 2015, **125**, 3356-3364.

81. J. S. Ko, R. M. Bukowski and J. H. Fincke, *Curr. Oncol. Rep.*, 2009, **11**, 87-93.

82. E. Shtivelman, M. A. Davies, P. Hwu, J. Yang, M. Lotem, M. Oren, K. T. Flahery and D. E. Fisher, *Oncotarget*, 2014, **5**, 1701-1752.

83. J. Vincent, G. Mignot, F. Chalmin, S. Ladoire, M. Bruchard, A. Chevriaux, F. Martin, L. Apetoh, C. Rebe and F. Ghiringhelli, *Cancer Res.*, 2010, **70**, 3052-3061.

84. M. R. Shurin, *Nat. Med.*, 2013, **19**, 20-22.

85. M. R. Shurin, H. Naiditch, D. W. Gutkin, V. Umansky and G. V. Shurin, *Curr. Med. Chem.*, 2012, **19**, 1792-1803.

86. S. Gingis-Velitski, D. Loven, L. Benayoun, M. Munster, R. Bril, T. Voloshin, D. Alishekevitz, F. Bertolini and Y. Shaked, *Cancer Res.*, 2011, **71**, 6986-6996.

87. W. Bouquet, W. Ceelen, E. Adriaens, A. Almeida, T. Quinten, F. D. Vos, P. Pattyn, M. Peeters, J. P. Remon and C. Vervaet, *Annals of Surgical Oncology*, 2010, **17**, 2510-2517.

88. D. I. Gabrilovich, *Cancer Immunol. Res.*, 2017, **5**, 3-8.

89. V. Bronte, S. Brandau, S.-H. Chen, M. P. Colombo, A. B. Frey, T. F. Greten, S. Mandruzzato, V. Umansky, R. H. Vonderheide and D. I. Gabrilovich, *Nat. Commun.*, 2016, **7**, 12150.

90. J. E. Talmadge and D. I. Gabrilovich, *Nat. Rev. Cancer*, 2013, **13**, 739-752.

91. S. Ostrand-Rosenberg, *BMC Proc.*, 2013, **7**, K20.

92. H. Zhong, D. W. Gutkin, B. Han, Y. Ma, A. A. Keskinov, M. R. Shurin and G. V. Shurin, *Int. J. Cancer*, 2014, **134**, 2633-2645.

93. J. Wang, L. Yang, L. Yu, Y.-Y. Wang, R. Chen, J. Qian, Z.-P. Hong and X.-S. Su, *Oncotarget*, 2017, **8**, 17050-17058.

94. B. Huang, P.-Y. Pan, Q. Li, A. I. Sato, D. E. Levy, J. Bromberg, C. M. Divino and S.-H. Chen, *Cancer Res.*, 2006, **66**, 1123-1131.

95. P. Sinha, V. K. Clements, S. K. Bunt, S. M. Albelda and S. Ostrand-Rosenberg, *J. Immunol.*, 2007, **179**, 977-983.

96. J. Sceneay, M. T. Chow, A. Chen, H. M. Halse, C. S. F. Wong, D. M. Andrews, E. K. Sloan, B. S. Parker, D. D. Bowtell, M. J. Smyth and A. Moller, *Cancer Res.*, 2012, **72**, 3906-3911.

97. E. Suzuki, V. Kapoor, A. S. Jassar, L. R. Kaiser and S. M. Albelda, *Clin. Cancer Res.*, 2005, **11**, 6713-6721.

98. S. Ugel, F. D. Sanctis, S. Mandruzzato and V. Bronte, *J. Clin. Invest.*, 2015, **125**, 3365-3376.

99. I. I. Vlasova, A. A. Kapralov, Z. P. Michael, S. C. Burkert, M. R. Shurin, A. Star, A. A. Shvedova and V. E. Kagan, *Toxicol. Appl. Pharmacol.*, 2016, **299**, 58-69.

100. Y. Tang, S. C. Burkert, Y. Zhao, W. A. Saidi and A. Star, *J. Phys. Chem. C*, 2013, **117**, 25213-25221.

101. Y. Tang, Y. Zhao, S. C. Burkert, M. Ding, J. E. Ellis and A. Star, *Carbon*, 2014, **80**, 583-590.

102. H. Dong, Y. Zhao, Y. Tang, S. C. Burkert and A. Star, *ACS Appl. Mater. Interfaces*, 2015, **7**, 10734-10741.

103. L. Yang, J. Shui, L. Du, Y. Shao, J. Liu, L. Dai and Z. Hu, *Adv. Mater.*, 2019.

104. C. Hu and L. Dai, *Adv. Mater.*, 2018, **31**, 1804672.

105. S. Zhao, D.-W. Wang, R. Amal and L. Dai, *Adv. Mater.*, 2018.

106. L. Qu, Y. Liu, J.-B. Baek and L. Dai, *ACS Nano*, 2010, **4**, 1321-1326.

107. Y. Liang, Y. Li, H. Wang and H. Dai, *J. Am. Chem. Soc.*, 2013, **135**, 2013-2036.

108. T. Chen, Z. Cai, Z. Yang, L. Li, X. Sun, T. Huang, A. Yu, H. G. Kia and H. Peng, *Adv. Mater.*, 2011, **23**, 4620-4625.

109. S. Maldonado and K. J. Stevenson, *J. Phys. Chem. B*, 2005, **109**, 4707-4716.

110. J. Kruusma, N. Mould, K. Jurkschat, A. Crossley and C. E. Banks, *Electrochem. Commun.*, 2007, **9**, 2330-2333.

111. A. H. Groschel and A. H. E. Muller, *Nanoscale*, 2015, **7**, 11841-11876.

112. R. Ye, J. Dong, L. Wang, R. Mendoza-Cruz, Y. Li, P.-F. An, M. J. Yacaman, B. I. Yakobson, D. Chen and J. M. Tour, *Carbon*, 2018, **132**, 623-631.

113. L. Wang and M. Pumera, *Chem. Commun.*, 2014, **50**, 12662-12664.

114. H. R. Byon, J. Suntivich and Y. Shao-Horn, *Chem. Mater.*, 2011, **23**, 3421-3428.

115. Q. Liu and J. Zhang, *Langmuir*, 2013, **29**, 3821-3828.

116. A. Hirano, M. Wada, T. Tanaka and H. Kataura, *ACS Nano*, 2019.

117. C. Song and J. Zhang, in *PEM Fuel Cell Electrocatalysts and Catalyst Layers*, ed. J. Zhang, Springer, London, 2008.

118. X. Xu, S. Jiang, Z. Hu and S. Liu, *ACS Nano*, 2010, **4**, 4292-4298.

119. S. Kattel, P. Atanassov and B. Kiefer, *Phys. Chem. Chem. Phys.*, 2013, **15**, 148-153.

120. B. L. Allen, C. M. Shade, A. M. Wingling, S. Petoud and A. Star, *Adv. Mater.*, 2009, **21**, 4692-4695.

121. Y. Wang and X. Bai, *Mater. Lett.*, 2009, **63**, 206-208.

122. D. Shimamoto, K. Fujisawa, H. Muramatsu, T. Hayashi, Y. A. Kim, T. Yanagisawa, M. Endo and M. S. Dresselhau, *Carbon*, 2010, **48**, 3643-3647.

123. Y. Zhao, Y. Tang and A. Star, *J. Vis. Exp.*, 2013, **75**, e50383.

124. T. Enoki, M. Suzuki and M. Endo, *Graphite intercalation compounds and applications*, Oxford University, New York, 2003.

125. T. Li, Y.-H. Liu, B. Chitara and J. E. Goldberger, *J. Am. Chem. Soc.*, 2014, **136**, 2986-2989.

126. J. E. Jones, M. C. Cheshire, D. J. Casadonte and C. C. Phifer, *Org. Lett.*, 2004, **6**, 1915-1917.

127. A. Ciesielski and P. Samori, *Chem. Soc. Rev.*, 2014, **43**, 381-398.

128. H. Maeda, *Adv. Enzyme Regul.*, 2001, **41**, 189-207.

129. T. Inoshita, K. Nakao and H. Kamimura, *J. Phys. Soc. Jpn.*, 1977, **43**, 1237-1243.

130. D. V. Kosynkin, A. L. Higginbottham, A. Sinitskii, J. R. Lomeda, A. Simiev, B. K. Price and J. M. Tour, *Nature*, 2009, **458**, 872-876.

131. R. Cruz-Silva, A. Morelos-Gomez, S. Vega-Diaz, F. Tristan-Lopez, A. L. Elias, N. Perea-Lopez, H. Muramatsu, T. Hayashi, K. Fujisawa, Y. A. Kim, M. Endo and M. Terrones, *ACS Nano*, 2013, **7**, 2192-2204.

132. Y. Li, Y. Hu, Y. Zhao, G. Shi, L. Deng, Y. Hou and L. Qu, *Adv. Mater.*, 2010, **23**, 776-780.

133. D. Pan, J. Zhang, Z. Li and M. Wu, *Adv. Mater.*, 2010, **22**, 734-738.

134. Y. Li, Y. Zhao, H. Cheng, Y. Hu, G. Shi, L. Dai and L. Qu, *J. Am. Chem. Soc.*, 2012, **134**, 15-18.

135. J. F. Li, Y. F. Huang, Y. Ding, Z. L. Yang, S. B. Li, X. S. Zhou, F. R. Fan, W. Zhang, Z. Y. Zhou, D. Y. Wu, B. Ren, Z. L. Wang and Z. Q. Tian, *Nature*, 2010, **464**, 392-395.

136. K. L. Wustholz, A.-I. Henry, J. M. McMahon, R. G. Freeman, N. Valley, M. E. Piotti, M. J. Natan, G. C. Schatz and R. P. V. Duyne, *J. Am. Chem. Soc.*, 2010, **132**, 10903-10910.

137. J.-H. Lee, J.-M. Nam, K.-S. Jeon, D.-K. Lim, H. Kim, S. Kwon, H. Lee and Y. D. Suh, *ACS Nano*, 2012, **6**, 9574-9584.

138. X. Zhou, X. Huang, X. Qi, S. Wu, C. Xue, F. Y. C. Boey, Q. Yan, P. Chen and H. Zhang, *J. Phys. Chem. C*, 2009, **113**, 10842-10846.

139. F. Schedin, E. Lidorikis, A. Lombardo, V. G. Kravets, A. K. Geim, A. N. Grigorenko, K. S. Novoselov and A. C. Ferrari, *ACS Nano*, 2010, **4**, 5617-5626.

140. R. Lv, Q. Li, A. R. Botello-Mendez, T. Hayashi, B. Wang, A. Berkdemir, Q. Hao, A. L. Elias, R. Cruz-Silva, H. R. Gutierrez, Y. A. Kim, H. Muramatsu, J. Zhu, M. Endo, H. Terrones, J.-C. Charlier, M. Pan and M. Terrones, *Sci. Rep.*, 2012, **2**, 586.

141. V. Blum, R. Gehrke, F. Hanke, P. Havu, V. Havu, X. Ren, K. Reuter and M. Scheffler, *Comput. Phys. Commun.*, 2009, **180**, 2175-2196.

142. J. P. Perdew, K. Burke and M. Ernzerhof, *Phys. Rev. Lett.*, 1996, **77**, 3865-3868.

143. A. Tkatchenko and M. Scheffler, *Phys. Rev. Lett.*, 2009, **102**, 073005.

144. V. Havu, V. Blum, P. Havu and M. Scheffler, *J. Comput. Phys.*, 2009, **228**, 8367-8379.

145. M. Lin, J. P. Y. Tan, C. Boothroyd, K. P. Loh, E. S. Tok and Y.-L. Foo, *Nano Lett.*, 2007, **7**, 2234-2238.

146. D. Shin, B. Jeong, B. S. Mun, H. Jeon, H.-J. Shin, J. Baik and J. Lee, *J. Phys. Chem. C*, 2013, **117**, 11619-11624.

147. G. Wu, K. L. More, C. M. Johnston and P. Zelenay, *Science*, 2011, **332**, 443-447.

148. M. Lefevre, E. Proietti, F. Jaouen and J.-P. Dodelet, *Science*, 2009, **324**, 71-74.

149. M. S. Thorum, J. M. Hankett and A. A. Gewirth, *The Journal of Physical Chemistry Letters*, 2011, **2**, 295-298.

150. B. Wang, *J. Power Sources*, 2005, **152**, 1-15.

151. H. Tang, H. Yin, J. Wang, N. Yang, D. Wang and Z. Tang, *Angew. Chem. Int. Ed. Engl.*, 2013, **52**, 5585-5589.

152. J. Masa, A. Zhao, W. Xia, M. Muhler and W. Schuhmann, *Electrochim. Acta*, 2014, **128**, 271-278.

153. A. Titov, P. Zapol, P. Kral, D.-J. Liu, H. Iddir, K. Baishya and L. A. Curtiss, *J. Phys. Chem. C*, 2009, **113**, 21629-21634.

154. V. Tripkovic, M. Vanin, M. Karamad, M. E. Bjorketun, K. W. Jacobsen, K. S. Thygesen and J. Rossmeisl, *J. Phys. Chem. C*, 2013, **117**, 9187-9195.

155. H. Feng, J. Ma and Z. Hu, *J. Mater. Chem.*, 2010, **20**, 1702-1708.

156. D. Kochubey, V. Kaichev, A. Saraev, S. Tomyn, A. Belov and Y. Voloshin, *J. Phys. Chem. C*, 2013, **117**, 2753-2759.

157. U. I. Koslowski, I. Abs-Wurmbach, S. Fiechter and P. Bogdanoff, *J. Phys. Chem. C*, 2008, **112**, 15356-15366.

158. L. Ding, Q. Xin, X. Zhou, J. Qiao, H. Li and H. Wang, *J. Appl. Electrochem.*, 2012, **43**, 43-51.

159. J. K. Norskov, J. Rossmeisl, A. Logadottir and L. Lindqvist, *J. Phys. Chem. B*, 2004, **108**, 17886-17892.

160. F. Cella-Vallejo, J. I. Martinez and J. Rossmeisl, *Phys. Chem. Chem. Phys.*, 2011, **13**, 15639-15643.

161. M. S. Dresselhaus and G. Dresselhaus, *Adv. Phys.*, 2002, **51**, 1-186.

162. L. M. Viculis, J. J. Mack and R. B. Kaner, *Science*, 2003, **299**, 1361.

163. K. S. Suslick and D. J. Flannigan, *Annu. Rev. Phys. Chem.*, 2008, **59**, 659-683.

164. A. L. Higginbotham, D. V. Kosynkin, A. Sinitskii, Z. Sun and J. M. Tour, *ACS Nano*, 2010, **4**, 2059-2069.

165. T. Sharifi, G. Hu, X. Jia and T. Wagberg, *ACS Nano*, 2012, **6**, 8904-8912.

166. H. Chu, J. Wang, L. Ding, D. Yuan, Y. Zhang, J. Liu and Y. Li, *J. Am. Chem. Soc.*, 2009, **131**, 14310-14316.

167. Y. Zhao, S. C. Burkert, Y. Tang, D. C. Sorescu, A. A. Kapralov, G. V. Shurin, M. R. Shurin, V. E. Kagan and A. Star, *J. Am. Chem. Soc.*, 2015, **137**, 675-684.

168. S. C. Burkert and A. Star, *Curr. Protoc. Chem. Biol.*, 2015, **7**, 249-262.

169. M. S. Muthu, D. T. Leong, L. Mei and S.-S. Feng, *Theranostics*, 2014, **4**, 660-677.

170. M. S. Muthu, A. Abdulla and B. L. Pandey, *Nanomedicine*, 2013, **8**, 863-866.

171. K. Yamashita, Y. Yoshioka, K. Higashisaka, Y. Morishita, T. Yoshida, M. Fujimura, H. Kayamuro, H. Nabeshi, T. Yamashita, K. Nagano, Y. Abe, H. Kamada, Y. Kawai, T. Mayumi, T. Yoshikawa, N. Itoh, S.-i. Tsunoda and Y. Tsutsumi, *Inflammation*, 2010, **33**, 276-280.

172. S.-T. Yang, J. Luo, Q. Zhou and H. Wang, *Theranostics*, 2012, **2**, 271-282.

173. I. Florea, O. Ersen, R. Arenal, D. Ihiawakrim, C. Messaoudi, K. Chizari, I. Janowska and C. Pham-Huu, *J. Am. Chem. Soc.*, 2012, **134**, 9672-9680.

174. J. Kimling, M. Maier, B. Okenve, V. Kotaidis, H. Ballot and A. Plech, *J. Phys. Chem. B*, 2006, **110**, 15700-15707.

175. J. Chen, S. Chen, X. Zhao, L. V. Kuznetsova, S. S. Wong and I. Ojima, *J. Am. Chem. Soc.*, 2008, **130**, 16778-16785.

176. M. Prato, K. Kostarelos and A. Bianco, *Acc. Chem. Res.*, 2008, **41**, 60-68.

177. W. Wu, S. Wieckowski, G. Pastorin, M. Benincasa, C. Klumpp, J.-P. Briand and R. Gennaro, *Angew. Chem. Int. Ed. Engl.*, 2005, **44**, 6358-6362.

178. Z. Liu, X. Sun, N. Nakayama-Ratchford and H. Dai, *ACS Nano*, 2007, **1**, 50-56.

179. Y. Ren and G. Pastorin, *Adv. Mater.*, 2008, **20**, 2031-2036.

180. B. M. Kim, S. Qian and H. H. Bau, *Nano Lett.*, 2005, **5**, 873-878.

181. A. Guven, I. A. Rusakova, M. T. Lewis and L. J. Wilson, *Biomaterials*, 2012, **33**, 1455-1461.

182. K. Yanagi, Y. Miyata and H. Kataura, *Adv. Mater.*, 2006, **18**, 437-441.

183. G. Kresse and J. Furthmuller, *J. Comput. Mater. Sci.*, 1996, **6**, 15-50.

184. G. Kresse and J. Furthmuller, *J. Phys. Rev. B*, 1996, **54**, 11169.

185. P. E. Blochl, *J. Phys. Rev. B*, 1994, **50**, 17953.

186. T. Bucko, S. Lebegue, J. Hafner and J. G. Angyan, *J. Phys. Rev. B*, 2013, **87**, 064110.

187. G. Henkelman, *J. Chem. Phys.*, 2000, **113**, 9901.

188. X. Ma, E. G. Wang, R. D. Tilley, D. A. Jefferson and W. Zhou, *Appl. Phys. Lett.*, 2000, **77**, 4136.

189. A. Schon, B. R. Clarkson, M. Jaime and E. Freire, *Proteins*, 2017, **85**, 2009-2016.

190. S. D. House, C. M. Andolina, S. C. Burkert, A. Star and J. C. Yang, *Microsc. Microanal.*, 2018.

191. X. Fu, F. Bei, X. Wang, S. O'Brien and J. R. Lombardi, *Nanoscale*, 2010, **2**, 1461-1466.

192. C. S. Rout, A. Kumar, G. Xiong, J. Irudayaraj and T. S. Fisher, *Appl. Phys. Lett.*, 2010, **97**, 133108.

193. J. Chowdhury, P. Pal, M. Ghosh and T. N. Misra, *J. Colloid Interface Sci.*, 2001, **235**, 317-324.

194. J.-P. Sylvestre, S. Poulin, A. V. Kabashin, E. Sacher, M. Meunier and J. H. T. Luong, *J. Phys. Chem. B*, 2004, **108**, 16864-16869.

195. Y. H. Yun, B. K. Lee and K. Park, *J. Control. Release*, 2015, **219**, 2-7.

196. S. C. Burkert, G. V. Shurin, D. L. White, X. He, A. A. Kapralov, V. E. Kagan, M. R. Shurin and A. Star, *Nanoscale*, 2018, **10**, 17990-18000.

197. D. Peer, J. M. Karp, S. Hong, O. C. Farokhzad, R. Margalit and R. Langer, *Nat. Nanotechnol.*, 2007, **2**, 751-760.

198. S. W. Kim, T. Kim, Y. S. Kim, H. S. Choi, H. J. Lim, S. J. Yang and C. R. Park, *Carbon*, 2012, **50**, 3-33.

199. V. Sanna, N. Pala and M. Sechi, *Int. J. Nanomedicine*, 2014, **9**, 467-483.

200. M. G. Sikkandhar, A. M. Nedumaran, R. Ravichandar, S. Singh, I. Santhakumar, Z. C. Goh, S. Mishra, G. Archunan, B. Gulyas and P. Parmanabhan, *Int. J. Mol. Sci.*, 2017, **18**, E1036.

201. L. Tian and Y. H. Bae, *Colloids Surf., B*, 2012, **99**, 116-126.

202. R. Wesolowski, J. Markowitz and I. William E. Carson, *J. Immunother. Cancer*, 2013, **1**, 10.

203. K. H. Parker, D. W. Beury and S. Ostrand-Rosenberg, *Adv. Cancer Res.*, 2015, **128**, 95-139.

204. D. D. Mitri, A. Toso and A. Alimonti, *Clin. Cancer Res.*, 2015, **21**, 1-5.

205. K. N. Kodumudi, K. Woan, D. L. Gilvary, E. Sahakian, S. Wei and J. Y. Djeu, *Clin. Cancer Res.*, 2010, **16**, 4583-4594.

206. V. Kumar, S. Patel, E. Tcyganov and D. I. Gabrilovich, *Trends in Immunology*, 2016, **37**, 208-220.

207. V. J. Poirier, A. E. Hershey, K. E. Burgess, B. Phillips, M. M. Turek, L. J. Forrest, L. Beaver and D. M. Vail, *J. Vet. Intern. Med.*, 2008, **18**, 219-222.

208. T. Iwamoto, *Biol. Pharm. Bull.*, 2013, **36**, 715-718.

209. T. Michels, G. V. Shurin, H. Naiditch, A. Sevko, V. Umansky and M. R. Shurin, *J. Immunotoxicol.*, 2012, **9**, 292-300.

210. A. Sevko, T. Michels, M. Vrohlings, L. Umansky, P. Beckhove, M. Kato, G. V. Shurin, M. R. Shurin and V. Umansky, *J. Immunol.*, 2013, **190**, 2464-2471.

211. C. Lasagna-Reeves, D. Gonzalez-Romero, M. A. Barria, I. Olmedo, A. Clos, V. M. S. Ramanujam, A. Urayama, L. Vergara, M. J. Kogan and C. Soto, *Biochem. Biophys. Res. Commun.*, 2010, **393**, 649-655.

212. K. Ajima, M. Yudasaka, T. Murakami, A. Maigne, K. Shiba and S. Iijima, *Mol. Pharm.*, 2005, **2**, 475-480.

213. Caroline de Gracia Lux, S. Joshi-Barr, T. Nguyen, E. Mahmoud, E. Schopf, N. Fomina and A. Almutairi, *J. Am. Chem. Soc.*, 2012, **134**, 15758-15764.

214. P. Wardman, *Free Radic. Biol. Med.*, 2007, **43**, 995-1022.

215. J. Flemmig, P. Schwarz, I. Backer, A. Leichsenring, F. Lange and J. Arnhold, *J. Immunol. Methods*, 2014, **415**, 46-56.

216. B. Brune, N. Dehne, N. Grossmann, M. Jung, D. Namagaladze, T. Schmid, A. v. Knethen and A. Weigert, *Antioxid. Redox Signal*, 2013, **19**, 595-637.

217. H. Mangge, K. Becker, D. Fuchs and J. M. Gostner, *World J. Cardiol.*, 2014, **6**, 462-477.

218. J. K. Lee, B. C. Sayers, K.-S. Chun, H.-C. Lao, J. K. Shipley-Phillips, J. C. Bonner and R. Langenbach, *Part. Fibre Toxicol.*, 2012, **9**, 14.

219. C. Bussy, M. Pinault, J. Cambedouzou, M. J. Landry, P. Jegou, M. Mayne-L'hermite, P. Launois, J. Boczkowski and S. Lanone, *Part. Fibre Toxicol.*, 2012, **9**, 46.

220. H. Zhong, B. Han, I. L. Tourkova, A. Lokshin, A. Rosenbloom, M. R. Shurin and G. V. Shurin, *Clin. Cancer Res.*, 2007, **13**, 5455-5462.

221. H. Naiditch, M. R. Shurin and G. V. Shurin, *Immunol. Res.*, 2011, **50**, 276-285.

222. J. P. Landreneau, M. R. Shurin, M. V. Agassandian, A. A. Keskinov, Y. Ma and G. V. Shurin, *Cancer Microenviron.*, 2015, **8**, 57-64.

223. R. Li, J. S. Eun and M.-K. Lee, *Arch. Pharmacal Res.*, 2011, **34**, 331-337.

224. D. Mandal, T. K. Shaw, G. Dey, M. M. Pal, B. Mukherjee, A. K. Bandyopadhyay and M. Mandal, *Int. J. Biol. Macromol.*, 2018, **112**, 818-830.

225. R. L. Roberts, J. Nath, M. M. Friedman and J. I. Gallin, *J. Immunol.*, 1982, **129**, 2134-2141.

226. G. V. Shurin, I. L. Tourkova, R. Kaneno and M. R. Shurin, *J. Immunol.*, 2009, **183**, 137-144.

227. G. V. Shurin, I. L. Tourkova and M. R. Shurin, *J. Immunother.*, 2008, **31**, 491-499.

228. R. Kaneno, G. V. Shurin, I. L. Tourkova and M. R. Shurin, *J. Transl. Med.*, 2009, **7**, 58.

229. T. Tanei, F. Leonard, X. Liu, J. F. Alexander, Y. Saito, M. Ferrari, B. Godin and K. Yokoi, *Cancer Res.*, 2016, **76**, 429-439.

230. Z. Liu, W. Cai, L. He, N. Nakayama, K. Chen, X. Sun, X. Chen and H. Dai, *Nat. Nanotechnol.*, 2007, **2**, 47-52.

231. A. Nakano, T. Harads, S. Morikawa and Y. Kato, *Acta Pathol. Jpn*, 1990, **40**, 107-115.

232. Y. Lv, C. Xu, X. Zhao, C. Lin, X. Yang, X. Xin, L. Zhang, C. Qin, X. Han, L. Yang, W. He and L. Yin, *ACS Nano*, 2018, **12**, 1519-1536.

233. W. Tang, J. Yang, Y. Yuan, Z. Zhao, Z. Lian and G. Liang, *Nanoscale*, 2017, **9**, 6529-6536.

234. A. Javeed, M. Ashraf, A. Riaz, A. Ghafoor, S. Afzal and M. M. Mukhtar, *Eur. J. Pharm. Sci.*, 2009, **38**, 283-290.

235. P. Huang, J. Huang, S. A. Pantovich, A. D. Carl, T. G. Fenton, C. A. Caputo, R. L. Grimm, A. I. Frenkel and G. Li, *J. Am. Chem. Soc.*, 2018, **140**, 16042-16047.